The Attachment of Colloidal Particles to Environmentally Relevant Surfaces: Effect of Ionic Strength, Particle Shape, and Physicochemical Properties

By

Coy P. McNew

Dissertation

Submitted to the Faculty of the

Graduate School of Vanderbilt University

in partial fulfillment of the requirements

for the degree of

DOCTOR OF PHILOSOPHY

in

Environmental Engineering

December, 2015

Nashville, Tennessee

Approved:

Professor Eugene J. LeBoeuf, Chair

Professor George Hornberger

Professor M. Douglas LeVan

Associate Professor Alan Bowers

Associate Professor Yusong Li

To my mom and dad, unconditionally supportive

ACKNOWLEDGMENTS

This work was financially supported by the National Science Foundation Award Nos. 1133528 and 1133280, the Vanderbilt University Discovery Grant Program, and the Vanderbilt University Department of Civil and Environmental Engineering.

This work would not have been possible without the support of my advisor, Gene LeBoeuf. From the day I received your call informing me of my acceptance into the doctoral program in Civil and Environmental Engineering, I knew I was in for something special and I definitely have not been disappointed. The freedom you've afforded me in my research pursuits and consistent confidence you've shown in my decisions have surely made me a better researcher, teacher, academic, and all around person.

To all of my family, who have unwaveringly supported me since day one. To my mom and dad, who have beamed with pride at each and every accomplishment I've ever achieved, regardless of how small or large. You have no idea how much you mean to me and how much you've shaped me into the person I am today. From the bottom of my heart, thank you for all that you've done for me and continue to do on a daily basis. To my late grandmother who always reminded me to look out for number one. If there's a better piece of daily advice out there, I've yet to hear it.

To Kate, who has shared in the daily (and sometimes hourly) ups and downs of being a graduate student. No one has ever taught me more about what it means to be emotionally mature and exactly how to make it through tough times. You have a big heart and some big brains too.

TABLE OF CONTENTS

Page

LIST OF TABLES

LIST OF FIGURES

Chapter 1

Introduction

1.1 Background and Motivation

The worldwide market for nanotechnology products is expected to reach a total of $64.2 billion over the next five years [1]. With such a high level of production and dissemination, the eventual release of engineered nanomaterials (ENMs) into the environment is inevitable, either from industrial sources or through disposal in municipal waste. In particular, carbonaceous nanomaterials (CNMs), such as fullerene (C_{60}) and multiwalled carbon nanotubes (MWNTs), have widespread applications in many areas (e.g. biomedical technology, electronics, and optics) [2–5] and are also produced in large quantities (e.g., 300 tons/year) [6]. Several studies have investigated and revealed the potential human health effects, aquatic toxicity, and antimicrobial properties of ENMs [3, 7–10]. Due to the ongoing environmental release coupled with a strong potential for toxicity, concern for the fate and transport of these materials in the environment is growing.

The fate and transport of ENMs are influenced by their unusual physicochemical properties, attributable to many factors including their small size (surface area and size distribution), composition (purity, crystallinity, electronic properties), surface structure (functional groups, inorganic or organic coatings), solubility, shape, and aggregation. Once in the environment, ENMs will participate in complex interactions with natural soils and sediments, and thus, organic matter attached on the soil and sediment surfaces. This soil and sediment organic matter (SOM) may be dissolved in the aqueous phase or immobilized (attached) on the surface soil or sediment grains. Attached SOM layers are the product of on-site physical and biological decomposition and are an essential component of natural soil and sediments. Attached SOM has been found to strongly sorb hydrophobic organic chemicals (HOCs) and thus influence their fate and transport [11]. If similar interactions between

SOM and ENMs exist, these interactions will influence potential pathways of exposure and eventual impact on ecosystems and human health. This work will focus on the interaction between ENMs and attached SOM layers, with the central hypothesis being that this interaction is governed by (A) the physicochemical characteristics (e.g. macromolecular properties) of SOM, (B) the ionic strength of solution, and (C) the fundamental nanostructure (e.g. shape) of ENMs. By using a suite of analytical instruments, the physicochemical properties of SOM, the shape of ENMs, and the ionic strength of solution are systematically varied while monitoring the effects on ENM aggregation, deposition, and attachment, as well as alterations in SOM structure. Not only will knowledge of SOM and ENM interactions improve the understanding of the fate and transport of ENMs in the natural environment, but it will also aid in the engineered environment, through improved understanding of factors influencing ENM aggregation and deposition behavior for applications in water and wastewater treatment.

1.2 Literature Review

1.2.1 Macromolecular properties of SOM

There are several categories of SOM with varying physical and chemical characteristics and composition based on age and degree of biological decomposition. SOM ranges from newly deposited biopolymers (e.g. polysaccharides and lignin), to moderately aged humic substances, to well-aged kerogen and black carbon. Some biopolymers show low affinities for HOCs, such as polysaccharides and lignin, but others, such as lipids, appear to be strong sorbents for HOCs [12]. Lipids, however, usually occur at very low concentrations in natural soils. Even though biopolymers are not normally considered a significant source of HOC sorption in soils [11], a study by Wang and Xing [13] observed an enhanced sorption of HOCs by biopolymer-derived chars.

Humic substances, including humins, humic acids, and fulvic acids, typically repre-

sent the dominant organic components in soils and sediments [14]. Chemically, humic substances are a mixture of both substituted aromatic and aliphatic compounds, forming a complex physical structure held together by inter- and intra-molecular interactions [15]. Humic acids represent complex mixtures of macromolecules with varying degrees of crosslinkages; however, research suggests that bulk properties of humic substances may be similar to those of organic macromolecules. For example, several humic substances have been shown to undergo thermal transitions similar to those observed for other organic macromolecules. These humic substances have been shown to transition from a more rigid, glass-like state to a more soft, rubbery-like state at temperatures ranging from 35 °C to 65 °C [16–22]. Some more well-aged, rigid SOMs, such as coals and kerogens, have also been observed to undergo similar transitions [23, 24], albeit usually at much higher temperatures. At this transition, additional thermal energy available results in an increase in the number and magnitude of molecular motions, effectively breaking molecular inter- and intra-chain crosslinkages, and allowing molecular chains to slide past one another. These increased molecular motions create greater free volume and a discontinuity in the second partial derivatives of free volume [22, 25]. The spreading of this transition over a range of temperatures is likely due to the heterogeneous nature of humic substances, both in terms of molecular weight and structure [22]. All of these studies, however, investigate a bulk and (in most cases) dry state of SOM. Attached SOM layers are typically hydrated, immobilized, thin layers of SOM which bring added variables into consideration, most notably water content and the presence of cations. Because of these added variables, it is not yet clear to what extent conclusions drawn in the aforementioned studies will translate to attached layers of SOM.

Soft humic substances often posses linear sorption behavior for HOCs, suggesting a partitioning-type process [26]. Rigid SOM, such as kerogen and black carbon, are characterized by more condensed, cross-linked, aromatic structures and are generally believed to be primarily responsible for adsorption-dominated processes [27]. Soft SOMs are usu-

ally associated with shorter sorption equilibrium attainment, on the order of several weeks to several months, while more rigid SOMs are usually associated with longer equilibrium times on the order of years [26]. The rate of diffusion of HOCs into the SOM is largely governed by the relaxation of the SOM matrix to accommodate the sorbing HOCs [28]. Since humic substances typically possess fewer and looser cross-linkages, they likely relax much quicker than the more condensed, cross-linked and tightly bound kerogen-dominated materials. This may partly explain the faster sorption equilibration times in humic substances.

An important factor when considering the macromolecular properties of SOM is, of course, the presence of water. The hydration of SOM has been shown to alter the SOM matrix in several key ways, namely through altered physicochemical properties. Water has been shown to interact strongly with hydrophilic SOM, with solubility parameters closest to that of water, including fulvic and humic acids [22, 25]. A stronger interaction results in greater water uptake and more swelling of the macromolecular matrix. In the case of humic acids, the swelling of the macromolecular matrix has been shown to result in increased macromolecular mobility and a reduced thermal transition temperature [22, 25], known as a plasticizing effect. In some studies, however, water has been shown to have an antiplasticizing effect [29–31]. In one study [29], the reduction of water content in a peat sample resulted in the reduction of the glass transition temperature, which suggested the water had an antiplasticizing effect. The authors attributed this antiplasticizing effect to a reduction in side chain mobility due to hydrogen bonds formed between water molecules and side chains. In another study [32], the hydration of a peat soil was investigated using differential scanning calorimetry. During the hydration and swelling of the peat soil matrix over an extended period of time, the increased water content showed a short term plasticizing effect (on the order of days) and a slow, long term antiplasticizing effect (on the order of weeks or months). This unexpected antiplasticizing effect was attributed to the slow formation of water bridges. Water molecule bridges (WaMB) form when small groups

of water molecules connect two functional groups by way of a hydrogen-bond bridge and reduce the mobility of these molecular segments [33].

These physicochemical changes in SOM due to hydration have also been shown to significantly affect the sorption of HOCs [34–37]. One study by Graber and Borisover [37] investigated the sorption equilibrium of phenol, pyridine, and atrazine on Pahokee peat. In the case of two of the three HOCs, sorption was greatly increased as the hydration of Pahokee peat was increased. Another such study [36] monitored the sorption of pyridine by Pahokee peat by investigating both the sorption equilibrium and kinetics in the presence of several solvents. The results indicate that the uptake of pyridine was clearly enhanced by all polar solvents, including hydration by water. The mechanism for increased sorption of HOCs due to increased hydration is likely explained by water-assisted disruption of polar SOM contacts, as described by Graber and Borisover [37]. As hydration increases, water molecules penetrate the SOM matrix and reach polar areas that were previously unavailable to HOC interaction, due to inter- or intra-molecular interactions. By hydrating these areas, the water molecules disrupt the interactions between these contacts and provide a new sorption site, which was previously unavailable. The extent to which this sorption enhancing characteristic of SOM hydration may apply to the attachment behavior of ENMs, however, has not yet been investigated.

Another important factor when considering the macromolecular properties of SOM is the presence of cation-mediated cross-linking and bridging. Cation-SOM interactions have been shown to depend on SOM characteristics (e.g. molecular size, composition, configuration), pH, ionic strength of the solution, cation properties, and the ratio of cation to SOM [38]. Thermal energy has not yet been shown to have an effect on cation-SOM interactions, though our recent work suggests it may also play a role [39]. In order for a cation cross-link or bridge to occur, the cation must be able to form a bi- or polydentate complex with two or more SOM functional groups [40]. This, however, does not mean the cations must be multivalent. In fact, the results of one study suggest that Na^{+} could act as an effective cation

for cross-linking [41]. Despite this finding, the tendency for cations to form cross-links is still expected to increase with increased valence [42]. If the SOM functional groups to be cross-linked are on different molecules, then the resulting cross-link is intermolecular, and if the SOM functional groups belong to the same molecule, the cross-link is intramolecular. Intermolecular cross-links have been shown to have effects on SOM supramolecular structure as well as the rigidity of the SOM macromolecular matrix [43]. In several studies, increases in sorption behavior and differences in sorption/desorption behavior of HOCs to NOM have been explained by the effects of cation cross-linking [43, 44], though this cation cross-linking effect on sorption has not yet been directly shown.

In order for a cation to form a cross-link or cation bridge (CaB) with two or more functional groups, the functional groups must be close enough together to all interact with the same cation. On the other hand, much larger distances between functional groups can be bridged by water molecules. As briefly mentioned earlier, WaMBs can span longer distances than direct CaB, with networks of up to 6–10 water molecules [33]. These WaMBs will increase cross-linking and can lead to a more rigid SOM matrix [45]. Cross-linking by combined WaMB and CaB can span even longer distances [43] and could cross-link functional groups that are too far apart for direct CaB or even WaMB. Since several studies have shown that water molecules do, in fact, contribute to cation cross-linking [33, 41] and in turn affect SOM macromolecular matrix rigidity [46], it is clear that water content is an important factor when considering cross-linking influences on macromolecular properties of SOM. The extent to which WaMB and combined WaMB and CaB affect the attachment behavior of ENMs to SOM has not yet been investigated.

1.2.2 Aggregation of ENMs in the aqueous environment

Once ENMs are released, their aggregation behavior and stability in the aqueous environment are key factors in determining their fate and transport. Large unstable aggregates will settle out quickly, reducing their transport and bioavailability, but smaller, more stable

aggregates may travel much further and pose a higher risk to organisms, ecosystems, or ultimately, human health. For this reason, it is critical to understand how ENM aggregates interact with all components of natural water systems. Natural water is a complex system of components, however, and because of that, very few studies have investigated the stability of ENMs in true natural water. Instead, this area of study has been broken down into three key variables that affect the stability of aqueous ENM suspensions, which include the presence of dissolved organic matter (DOM), the effect of pH, and the effect of ionic strength

DOM, being ubiquitous in the natural environment, will have ample opportunity to interact with ENMs once they are released. DOM is believed to interact with ENMs by adsorbing to the surface and coating the particles, altering their surface physicochemical properties and increasing their stability through steric repulsion [47, 48]. Several studies have illustrated that NOM fractions can interact with aqueous ENMs and increase their stability. A tannic acid was shown to stabilize multiwalled carbon nanotubes (MWNTs) in water [49], a humic acid was shown to increase the stability of an aqueous nC_{60} suspension [50], and a DOM extracted from Sahan River in Ukraine was shown to do the same [51]. In addition to these fractionated NOM studies, a Suwannee River water sample with unaltered NOM background was shown to stabilize a suspension of MWNTs, which remained stable for over a month [52]. This result was attributed to the high amount of DOM in the Suwannee River water, which amounted to 59.1 mg/L total carbon content. As discussed earlier, SOM is a heterogeneous mixture of macromolecules with varying physical and chemical characteristics depending on the history, age, and degree of biodecomposition. Depending on these factors, different types of SOM could affect aqueous ENMs in different ways, which remains to be explored.

In the aquatic environment, pH is a master variable that affects the properties of most components. In terms of aqueous ENMs, pH is the major determining factor of zeta potential. Zero point charge (zpc) is the pH value at which a particle carries a zeta potential of

zero and the uncharged particle is at a minimum stability. At a pH near the zpc, the particles will aggregate and flocculate to form large particles and settle out rapidly. At a pH below the zpc, the particles are positively charged and at a pH above the zpc, the particles are negatively charged. The further the pH deviates from the zpc, the more charged the particles become. Zpc values reported for ENMs of interest to this work include a pH of 4.7–6.4 for MWNTs [53] and a pH of 0–1 for nC_{60} [54]. The actual zpc for any given system may deviate from the reported values however, as one study hypothesizes that the zpc of ENMs might vary with particle size [55]. No discernible correlation between particle size and zpc can be seen in summaries of the reported zpc literature [56] however, and so these reported differences may be due to other factors (e.g., suspension preparation method or method for synthesis of particles), so further study would be needed to confirm this hypothesis.

The pH may also affect the stability of aqueous ENMs in another, more complex manner by affecting the DOM coating on the surface of the particles. As discussed previously, DOM can coat the aqueous ENM particles and enhance their stability through steric repulsion. Contrary to this finding, two studies involving the interaction of iron oxide nanoparticles with Suwannee River humic acid [57] and MWNTs with tannic acid [53], have shown that, at suitable pH values, the presence of DOM can actually decrease the stability of the nanoparticles. In the latter study, tannic acid is introduced into an aqueous suspension of MWNTs, effectively enhancing the stability of the suspension. Once the pH is lowered below 5, however, the particles destabilize and settle out. The authors attributed this effect to the lowering of the pH below the pKa of the tannic acid, which caused it to bridge tannic acid coated molecules with possible hydrogen bonds, aggregating particles and greatly reducing the stability of the suspension. This conclusion may be suspect though, since a pH of 5 falls right in the middle of the previously reported zpc range for MWNTs (pH 4.7 - 6.4) [53], and therefore the particle destabilization may be due to the neutral zeta potential instead of the DOM bridging. Despite this disputable conclusion, it is clear that pH plays a major and complex role in the stability of aqueous ENMs.

The effect of ionic strength on the stability of aqueous colloidal particles is a well studied subject and appears to apply to ENMs quite well. When an ENM particle forms in an aqueous environment, it carries a surface charge which causes an electrical double layer to form around it. Depending on the strength of the charge (magnitude of zeta potential), the electrical double layer surrounding each approaching particle will repel one another and keep the particles stable in suspension. The presence of electrolytes will screen this electrical double layer repulsion to some extent, depending on the concentration of electrolytes and the valence of ions. The electrical double layer repulsion can be screened to an extent where the van der Waals attraction forces dominate and the particles aggregate rapidly and settle out. The classic Derjaguin-Landau-Verwey-Overbeek (DLVO) theory [58, 59] describes the stability of aqueous colloids by combining the effects of the two aforementioned forces, electrical double layer repulsion (V_R) and van der Waals attraction (V_A), to constitute the total interaction energy (V_T).

A representative interaction profile of a relatively stable suspension of spherical particles is presented in Fig. 1.1. As one particle approaches another from a distance, the attractive and repulsive forces combine to form an energy barrier, which must be overcome for the particles to aggregate. As ionic strength is increased or zeta potential decreased, both of which usually result from an increase in electrolytes, the energy barrier is reduced. This can continue until van der Waals attractions dominate and the energy barrier vanishes. At this point, the suspension becomes unstable and the particles aggregate rapidly. In this manner, the magnitude of the energy barrier can describe the stability of the colloidal suspension.

The transformation from a stable colloid to a rapidly aggregating colloid occurs over a very narrow range of electrolyte concentration, which culminates in the critical coagulation concentration (CCC) [60]. According to the Schulze-Hardy rule [60], the valence (z) of the counterions play a major role in the location of the CCC, with the CCC being proportional to z^{-6}. Several studies have confirmed the presence of CCC and proportionality

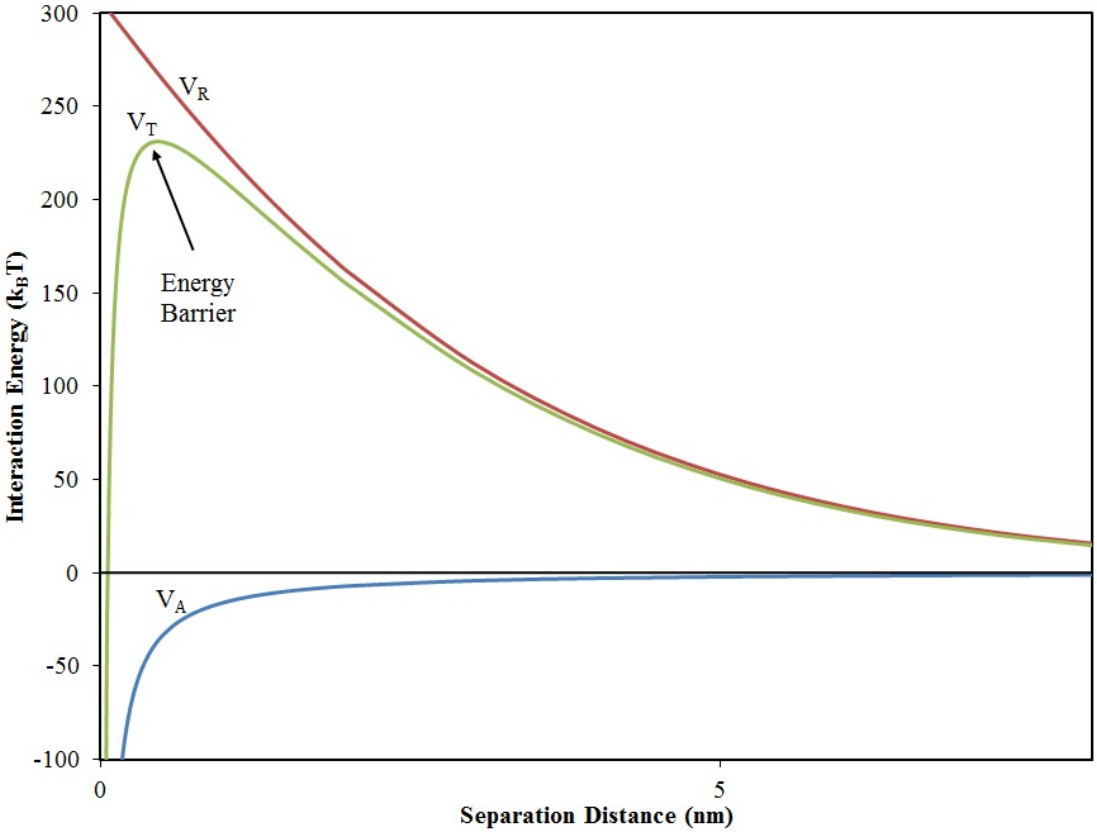

Figure 1.1: Example DLVO interaction energy curve.

to z for both aqueous nC_{60} suspensions [50, 61] and aqueous MWNT suspensions [53, 62], suggesting qualitative agreement with the DLVO theory. Furthermore, the aggregation of an aqueous suspension of nC_{60} has been shown to be in good quantitative agreement with DLVO theory [61]. Based on all the previously discussed information, it is clear that the stability of ENM aqueous suspensions are dependent upon a complex interaction of variables, namely the presence and type of DOM, pH of solution, and the concentration and valence of counterions.

1.2.3 Deposition of ENMs in the subsurface environment

Just as the aggregation behavior of ENMs can determine their fate and transport in the natural environment, so can their deposition behavior. The deposition of ENMs occur when ENM particles collide with and sorb to an immobile surface such as sand or soil grains, which may or may not be coated with different types of SOM. ENM deposition can occur in many types of aquatic environments, including surface or ground water and because of this, the deposition of ENMs is expected to play an important role in determining the fate and transport of ENMs in the natural environment.

The immobile surface, onto which the ENM particles deposit, can be considered an infinitely large particle (relative to the ENM particles), and therefore deposition can be studied as a form of heteroaggregation [60]. Because of this, the DLVO theory is sometimes employed to describe the deposition of ENMs. As stated previously, the DLVO theory describes the interaction between particles as the sum of the electrical double layer repulsive forces and the van der Waals attractive forces. As also stated previously, the electrical double layer repulsive forces are strongly affected by the valence and concentration of electrolyte within the system [60]. Therefore, qualitatively, DLVO theory would predict the deposition of ENMs to increase with both increasing concentration and valence of electrolytes. Several studies have focused on investigating deposition of ENMs onto silica surfaces by varying the electrolyte concentration [61, 63–66] and these studies are explored

further below.

In order to compare deposition rates at varying conditions, independent of ENM aggregation effects [61], the attachment efficiency (α) can be calculated by dividing the initial deposition rate by the corresponding initial deposition rate under favorable (oppositely charged) conditions. By comparing α between varying solution conditions, instead of the deposition rates, the attachment behavior can be compared independent of ENM aggregation effects. Studies investigating aqueous suspensions of both nC_{60} [61, 64, 66] and MWNTs [63, 65] report an increase in α with increasing electrolyte concentration until a critical concentration when α levels off at a maximum of 1. As electrolyte concentration increased, the electrical double layer repulsive forces between the particle and the negatively charged silica surface were screened and the van der Waals attraction forces were unaffected. This continued until the electrical double layer screening was so effective that the van der Waals attractions dominated and the deposition was equal to the deposition onto an oppositely charged surface. These findings are in qualitative agreement with DLVO theory. Additionally, two of the aforementioned studies [61, 66] reported a much larger charge screening effect when a divalent cation (Ca2+) was introduced. This finding is in further qualitative agreement with DLVO theory. These studies demonstrate that the ionic strength can have a tremendous effect on the deposition of ENMs onto mineral surfaces in electrolyte solutions and that this effect can be described by DLVO theory. Unfortunately, the subsurface environment contains additional variables for consideration, namely the presence of SOM as both DOM and attached SOM layers.

As discussed earlier, SOM is ubiquitous in the subsurface environment and can exist in a dissolved form as DOM or attached to large particle or grain surfaces as immobilized SOM layers. When DOM is present in an ENM suspension, it is believed to adsorb to the surface of the particles and increase their stability through steric repulsion. Studies have confirmed this effect for aqueous suspensions of both nC_{60} [50] and MWNTs [52]. In the context of ENM deposition, DOM is expected to have a similar effect. Two studies confirm this

expectation by investigating the effect of DOM (humic substances) on the deposition of an aqueous nC_{60} suspension [66, 67]. In both cases, the deposition of nC_{60} particles onto the silica surface was hindered by the presence of dissolved humic substances. As expected, the authors attributed this finding to the steric hindrance induced by humic molecules adsorbing onto the surface of the nanoparticles. Steric repulsion is a non-DLVO force and therefore, DLVO theory does not correctly predict this effect.

Until very recently, less work has been done to investigate the interactions between ENMs and the other ubiquitous form of SOM, attached SOM layers. One study [66] investigated the deposition of an aqueous suspension of nC_{60} onto silica surfaces precoated with humic acid and alginate. Attached humic acid was shown to reduce the attachment of nC_{60} for both NaCl concentrations investigated, while attached alginate increased the attachment of nC_{60} in the presence of 10 mM NaCl, while decreasing the attachment of nC_{60} in the presence of 30 mM NaCl. The variable behavior of the alginate layer was attributed to its compaction at higher salt concentrations, resulting in a smoother, more rigid layer. A recent study [64] investigated the deposition of an aqueous nC_{60} suspension onto silica surfaces coated with two different humic acids. The Suwannee River Humic Acid (SRHA) coating showed similar attachment of nC_{60} as that of bare silica, while the Elliot Soil Humic Acid appeared to hinder the attachment of nC_{60} over the majority of the NaCl concentration range investigated. A very recent study [63] investigated the interaction between MWNTs and silica surfaces with and without coatings of SRHA. In the presence of attached SRHA, the MWNTs displayed similar attachment behavior as the case for bare silica, since α values for the two cases did not appear statistically different. As described previously, DLVO theory only takes into account the forces of electrical double layer repulsion and van der Waals attraction, therefore these studies illustrate yet another SOM effect that DLVO theory does not correctly predict. Due to the variable nature of conclusions about the effect of SOM layers in the aforementioned papers, it is clear that the physicochemical properties and origin of SOM will likely play a key role in its effect on ENM deposition.

Another important variable to consider for the transport of ENMs or colloidal particles is the particle shape. Many natural colloids are nonspherical in shape, including plate and rod shaped clay [68], various bacterial shapes (e.g., ellipsoid, ovoid, and rod shaped) [69, 70], and some engineered nanomaterials (e.g., carbon nanotubes). Despite the ubiquity of nonspherical colloids, only a limited number of studies have focused on the role of shape with regard to colloidal transport [71–75]. Since most of the aforementioned studies exclusively employ column experiments, the mechanisms behind the particle-surface attachment cannot be isolated. To date, only one study has attempted to isolate the role of shape on particle deposition. Seymour et al. [71] reported a much higher deposition rate of spherical carboxylate-modified polystyrene particles as compared to 2:1 and 4:1 stretched versions of the same particles. These experiments, however, were conducted under favorable conditions (i.e., a positively charged, PLL-coated silica surface), lacking an energy barrier to deposition and limiting the environmental relevance of the findings. No study to date has investigated the role of shape on colloidal particle attachment to environmentally relevant surfaces.

1.2.4 Data-Driven Modeling

Unlike the traditional method of modeling, which involves the fitting of model results to experimental data by tuning model parameters, data-driven modeling allows for the development of empirical models which are trained on large databases of experimental results. This allows for the production of models which do not rely on physically vague model parameters, but rather on the physical and chemical characteristics that define the system. Particle transport models to date have largely relied on such model parameters [76–78] which do not explicitly take into account the physicochemical properties of the particles or the system [79]. Qualitative explanations that link physicochemical characteristics to particle transport and attachment have been developed (e.g., agreement or disagreement with DLVO theory) [39, 61, 64, 66, 80–82] however little quantitative mechanistic insight

has been developed from these studies. Without explicitly linking the physicochemical properties of the particle and system to the transport and attachment, these models remain descriptive tools rather than powerful predictive models.

Machine learning allows us to develop empirical models from complex systems where the underlying relationships between the data are too complex to develop by hand [83]. Machine learning has been successfully applied to a wide range of complex problems, including speech and computer vision, self driving cars, search engines, and medical diagnoses [84–87]. In two recent studies [88, 89] machine learning was applied to predict the toxicity and biological impacts of ENMs, based explicitly on the molecular properties of the nanomaterial. Despite the successes of machine learning in a wide range of applications, it has not been applied to the complex task of modeling environmental transport until very recently. A very recent study by Goldberg et al. [90] employed ensemble machine learning (random forest) regression and classification to predict the retained fraction (RF; the fraction of materials retained during a soil column experiment in comparison to the total mass of materials injected into the column) and shape of retention profile (RP) using a database of more than 200 nanomaterial column transport experiments amassed from published literature. Goldberg et al. [90] reported that their model was able to predict the RF with a mean squared error between 0.025–0.033, and the RP with an expected F1-score (the weighted harmonic mean of precision and recall) between 60–70%. Further, by recursively removing physical and chemical features to optimize model predictive performance, the authors were able to rank the importance of the physicochemical state features (e.g., pH, ionic strength, nanomaterial type, ect) to ENM transport.

An important difference between a data-driven modeling approach like machine learning and the traditional modeling approach is that the data-driven model is trained on a large database of experiments conducted at varying experimental conditions as a whole, rather than developed through separate investigations of isolated factors. This allows the data-driven model to consider the complex interactions between physicochemical conditions

which are lost when the conditions are investigated in isolation. The limiting factor, until recently, has been the lack of a sufficient amount of high quality experimental results to support a data-driven approach.

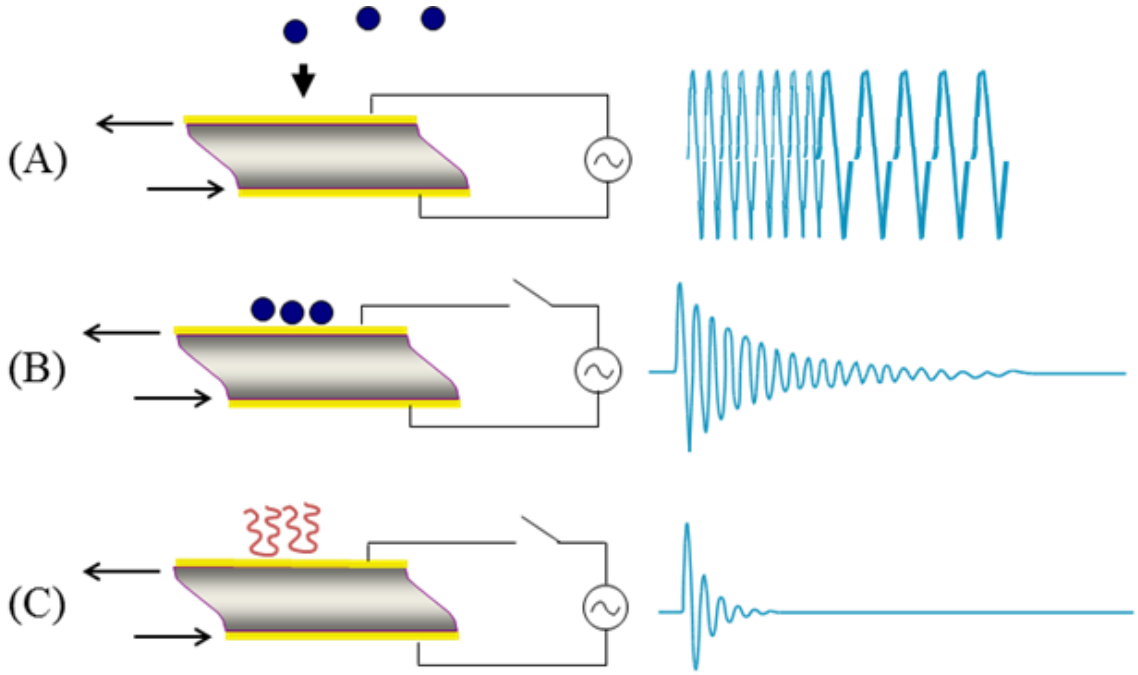

Figure 1.2: An overview of the main concepts involved in utilizing the QCM-D. Mass is coupled to the surface of the sensor, causing a decrease in observed frequency (A). At regular intervals, the power is shut off to the sensor and the rate of oscillatory energy decay is monitored (B & C), with lower dissipation values corresponding to a rigid mass (B) and higher dissipation values corresponding to a soft mass (C). This figure was adapted from a Q-Sense training course on the use of the QCM-D [91].

1.3 Quartz Crystal Microbalance with Dissipation Monitoring

The quartz crystal microbalance with dissipation monitoring (QCM-D) is a device that relies on the piezoelectric properties of quartz to measure nanogram sensitive mass uptake or release through changes in frequency and viscoelastic properties through changes in dissipation, in real time. The QCM-D used in the current work was a Q-Sense E4 system from Biolin Scientific (Stockholm, Sweden). The system consists of four flow modules, each containing a 5 MHz AT-cut, silica coated quartz sensor.

By applying an alternating voltage that matches the quartz sensor's resonance frequency (5 MHz), or multiples of the resonance frequency called overtones, the sensor undergoes an oscillatory deformation. In the case of the AT-cut sensor, this results in vibrations in the thickness-shear mode [92], which means the top and bottom surfaces oscillate in parallel,

but opposite directions (Fig. 1.2). As mass is coupled to the surface of the sensor, the oscillations slow and the frequency decreases (Fig. 1.2A).

At regular intervals throughout experimental analysis, the supplied current is shut off for a short period and the energy decay curve is monitored (Fig. 1.2B). By monitoring the rate at which the output voltage decays over time at a given resonance frequency, the dissipation parameter can be calculated. The dissipation parameter is a dimensionless quantity dependent on the oscillating sensor, any mass coupled to the surface, and the medium in which it is immersed. The dissipation parameter (D) is defined below in Eq. 1.1, where $E_{dissipated}$ is the energy dissipated in one oscillatory cycle and E_{stored} is the energy stored in the oscillating system [92].

$$D = \frac{E_{dissipated}}{2\pi E_{stored}} \tag{1.1}$$

In this manner, the dissipation can be used to infer about the viscoelastic properties of the mass coupled to the sensor. If the coupled mass is very rigid, the vibrational coupling of the mass and sensor will be very good and therefore a longer decay in the oscillatory energy will be observed (Fig. 1.2B). If the coupled mass is soft or viscoelastic, the vibrational coupling will be much poorer and the oscillatory energy will be dissipated much faster due to the poor coupling of the soft material to the stiff sensor (Fig. 1.2C).

The Sauerbrey Relation [93] (Eq. 1.2) has been widely used to describe the relationship between the frequency change of an oscillating sensor and the mass adsorbed onto the surface since its introduction in 1959. In the Sauerbrey Relation, the change in mass (m) is linearly proportional to the change in frequency (f) multiplied by the crystal constant (C) (17.7 ng cm^{-2} Hz^{-1}) divided by the overtone number (n). The Sauerbrey Relation hinges on three key assumptions, however, and they include:

(i) the mass adsorbed onto the sensor is small compared to the mass of the sensor;

(ii) the adsorbed mass is rigid and therefore perfectly coupled to the oscillations of the

sensor; and

(iii) the adsorbed mass is evenly spread over the surface of the sensor.

$$\Delta m = -C\frac{1}{n}\Delta f_n \tag{1.2}$$

The first and third assumptions hold true in most cases where well dispersed, small particles are being deposited onto the sensor in a thin layer. The second assumption however, does not hold true in the case of soft, viscoelastic films. This has been a well known issue since the QCM-D was shown to be applicable in liquids around 1980 [94]. Since a soft film does not follow the motions of the sensor perfectly well, some energy is lost, which is not measured by the frequency alone. By using multiple overtones of frequency and dissipation, there are enough inputs to use viscoelastic models that do not rely on the second assumption. Two such models are the Voigt and the Maxwell viscoelastic models [95]. Both of which are commonly used to estimate quantitative information about a soft mass from a QCM-D experiment, including thickness, viscosity, and density [94]. Due to the limitations of these models, for example, they rely on many parameters to be solved for simultaneously and they assume a homogenous, uniform layer, the deposition rate in this study will be quantified by the initial slope of the frequency shift.

QCM-D monitors the deposition rate of particles onto an oscillating sensor surface, isolating deposition kinetics, and allowing for a direct measure of attachment efficiency (α) without contributions from convection or filtration, unlike traditional soil column experiments. α is an important kinetic transport parameter and is widely used in colloid filtration theory (CFT) to quantify the likelihood of a particle attaching to a surface after a collision. In this manner, α allows the deposition behavior between varying conditions to be compared independent of particle aggregation effects.

Throughout this work, α was calculated from QCM-D data as seen in Eq. 1.3. The initial change of the third overtone of frequency with respect to time ($\frac{df_3}{dt}$) was calculated

from the first 120 seconds of particle deposition. Since the particles explored throughout this work were negatively charged at all experimental conditions examined, any particles that flow near a positively charged surface will attach, meaning the deposition in this case is limited only by diffusive mass transport. Such conditions were created by modifying the silica sensor with a layer of positively charged poly-L-lysine (PLL) and therefore, the diffusion limited deposition rate ($\left(\frac{df_3}{dt}\right)_{diff\ limited}$) was taken to be the particle deposition rate onto the PLL-coated surface at each corresponding experimental condition.

$$\alpha = \frac{df_3/dt}{\left(df_3/dt\right)_{diff\ limited}} \tag{1.3}$$

It should also be noted here that while the frequency shift gives insight into mass changes of the adsorbed layer, this includes any water molecules within the layer, or bound to the layer. The frequency shift associated with mass uptake which results in altered surface topography can be non-negligibly altered by a change in bound water molecules, depending on the surface roughness of the adsorbed layer [96, 97]. The root mean squared roughness (as measured by atomic force microscopy) of all surfaces investigated throughout this work were less than 6 nm, therefore this effect should not alter the frequency shift significantly, according to Rechendorff et al. [96]. Furthermore, all layer topography changes throughout this work resulted from altered solution conditions (ionic strength or temperature) after which ample time was given for the layer to equilibrate before particle deposition was monitored, therefore any frequency shift alterations resulting from water molecule trapping did not affect the observed value of particle deposition rate.

1.4 Research Obejctives

The purpose of this work is to quantitatively investigate the effect of various physicochemical characteristics and solution conditions on the value of particle attachment efficiency, identify which characteristics are most important to predicting attachment efficiency, and finally combine all published attachment efficiency data into an empirical, predictive model. The central hypothesis of this work states that the particle attachment efficiency will depend heavily on:

- The presence and physicochemical characteristics (e.g. macromolecular properties) of any attached SOM layers.
- The ionic strength of solution, through both salt concentration and ion valence.
- The shape of the colloidal, biological, or ENM particle.

Chapter 2 investigates the effect of type and physicochemical properties of attached SOM layers on the particle attachment efficiency of nC_{60}. Using a quartz crystal microbalance with dissipation monitoring (QCM-D), the deposition of nC_{60} onto silica sensors is monitored, with and without coatings of Harpeth humic acid (HHA) and Harpeth fulvic acid (HFA), while varying thermal energy. By comparing attachment efficiency curves as a function of temperature between bare silica, HHA-coated, and HFA-coated sensors with DLVO predictions, the effect of SOM coatings is elucidated. By comparing a thermal characterization of the SOM layers with the attachment efficiency trends, possible mechanisms are identified and discussed.

Chapter 3 focuses on solution chemistry and how it affects particle attachment efficiency. The attachment of nC_{60} onto silica sensors with and without coatings of HHA was monitored while salt concentration and valence was varied. Measurements of surface charge for all depositional surfaces at each experimental condition were compared with the attachment efficiency curves and DLVO predictions of interaction energy. Possible mecha-

nisms for the observed phenomena were introduced and discussed. The findings were also compared to similar published literature.

In Chapter 4, the role of particle shape is explored. Polystyrene (PS) spheres are heated to their glass transition temperature and stretched into an ellipsoidal conformation. By comparing the attachment efficiency of spherical and stretched PS, the role of shape is isolated. The presence of a terrestrial (HHA) and aquatic (Alginate) coating is also investigated and dramatic differences are observed. Through DLVO interaction energy calculations and atomic force microscopy images, possible mechanisms for these observed differences are elucidated.

Chapter 5 introduces a machine learning predictive model for attachment efficiency. All relevant, published attachment efficiency data is gathered and combined into a database and a total of 13 physicochemical characteristics are chosen as predictive features. An ensemble machine learning model (gradient boosting decision trees) is then trained on the database and the most important features for prediction are identified using recursive feature elimination with cross-validation (RFECV). The results from the predictive model and RFECV are presented and the implications of these findings are discussed.

Chapter 6 wraps up the work presented here, by bringing together all the reported information from each preceding chapter and discussing the conclusions and implications of the findings as a whole. Based on these findings, the suggested direction for future, related work is presented.

Chapter 2

The role of soil and sediment organic matter physicochemical properties on nC_{60} attachment

2.1 Introduction

In 2014, the nanotechnology market was valued at around $26 billion and it is expected to grow to $64.2 billion over the next five years [1]. In particular, the buckminsterfullerene (C_{60}) molecule has attracted much attention due to its widespread applications in many areas (e.g. biomedical technology, electronics, and optics) [2–4]. Due to the very low aqueous solubility of C_{60} [98], the nano-sized colloidal particle it forms in water (nC_{60}) is the most environmentally relevant form to study. With such a high level of production and dissemination, the eventual release of nC_{60} into the environment is inevitable, either from industrial sources or through disposal in municipal waste. Several studies have investigated and revealed the potential human health effects, aquatic toxicity, and antimicrobial properties of nC_{60} [3, 9, 10, 99]. The ongoing environmental release coupled with a strong potential for toxicity raise serious concern for the fate and transport of this material in the environment.

The fate and transport of nC_{60} is mainly influenced by aggregation and deposition processes, which are controlled by a complex balance of variables including pH, ionic strength, and presence of organic matter [56]. Once in the environment, nC_{60} will interact with natural soils and sediments, and thus, organic matter attached on the soil and sediment surfaces. Immobilized layers of soil and sediment organic matter (SOM) are the product of on-site physical and biological decomposition and are an essential component of natural soils and sediments. SOM layers have been found to strongly sorb hydrophobic organic chemicals (HOCs) and thus influence their transport [11]. If similar interactions between SOM layers and nC_{60} exist, these interactions will influence potential pathways of exposure and their

eventual impact on ecosystems and human health.

Humic substances, including humins, humic acids, and fulvic acids, typically represent the dominant organic components in soils and sediments [14]. Chemically, humic substances are a mixture of both substituted aromatic and aliphatic compounds, forming a complex physical structure held together by inter- and intra-molecular interactions [15] and therefore represent complex mixtures of macromolecules with varying degrees of crosslinkages. An important factor when considering the macromolecular properties of SOM is, of course, the presence of water. The hydration of SOM has been shown to alter the SOM matrix in several key ways, namely through altered physicochemical properties. Water has been shown to interact strongly with hydrophilic SOM, including fulvic and humic acids, resulting in water uptake and swelling of the macromolecular matrix [22, 25]. The physicochemical changes in SOM due to increased hydration have also been shown to significantly increase the sorption of HOCs [34–37]. The mechanism for increased sorption of HOCs due to increased hydration is likely explained by water-assisted disruption of polar SOM contacts, as described by Graber and Borisover [37]. As hydration increases, water molecules penetrate the SOM matrix and reach polar areas that were previously unavailable to HOC interaction, due to inter- or intra-molecular interactions. By hydrating these areas, the water molecules disrupt the interactions between these contacts and provide a new sorption site, which was previously unavailable. The extent to which this sorption enhancing characteristic of SOM hydration may apply to the deposition behavior of nC_{60}, however, has not yet been investigated.

Dissolved organic matter (DOM), in the form of humic substances, has been shown to adsorb to the surface of nC_{60} aggregates and, through steric repulsion, increase their stability to aggregation [50] and deposition [66]. Until very recently, however, little work has been done to investigate the interaction between nC_{60} and the other form of ubiquitous SOM, immobilized SOM layers. In recent studies, SOM layers have been shown to enhance, hinder, or have no effect on the attachment of nC_{60} depending on the type of

SOM and the ionic strength of solution [64, 66]. Furthermore, depending on the stabilizer, the transport of carbon nanotubes through humic acid coated quartz sand grains has been shown to vary between complete retention and minimal retention [100]. Due to the variable nature of conclusions presented in these studies, it is clear that SOM layers will play a complex role in the deposition of nC_{60}, likely dependent upon the type and physicochemical properties of SOM and the ionic strength of solution.

The purpose of this study is to further investigate the role SOM layers play on the deposition of nC_{60} by varying the type and physicochemical properties of SOM. Using a quartz crystal microbalance with dissipation monitoring (QCM-D), the deposition of nC_{60} onto silica surfaces with and without coatings of humic and fulvic acid was studied, while altering the physicochemical properties of the layer by varying temperature. The attachment efficiencies of nC_{60} onto three different surfaces as a function of temperature are then compared to DLVO theory predictions, and the effect of SOM physicochemical properties on the transport of nC_{60} is discussed. Not only will knowledge of SOM and engineered nanomaterial (ENM) interactions improve the understanding of the fate and transport of ENMs in the natural environment, but it will also aid in the engineered environment, through improved understanding of factors influencing the deposition behavior of similar types of ENMs for applications in water and wastewater treatment.

2.2 Materials and Methods

2.2.1 Materials and solution chemistry

Sublimed nC_{60} powder (99.9%) was purchased from MER Corporation (Tucson, AZ). Dry Harpeth River Humic Acid (HHA) and Fulvic Acid (HFA) were isolated as described in our previous publication [101]. Sodium phosphate monobasic (S5011), sodium phosphate dibasic (S5136), and poly-L-lysine hydrobromide (PLL, P1274) were purchased from Sigma-Aldrich (St. Louis, MO). Reagent grade NaCl (S671) was purchased from Fisher Scientific (Pittsburgh, PA). Silica-coated QCM-D sensors (QSX-303) were purchased from Q-Sense (Biolin Scientific, Stockholm, Sweden). All solutions were prepared using ultra pure water purified by the Milli-Q Water Purification system from Millipore (Billerica, MA).

Sodium phosphate monobasic and sodium phosphate dibasic were mixed on a 50% molar basis to produce a phosphate buffer that would maintain all solutions at a pH of 6.7 $\pm$ 0.1. The background electrolyte concentration for all experiments consisted of 70 mM NaCl and 2 mM of the previously described phosphate buffer.

2.2.2 nC_{60} stock suspension and SOM stock solutions

The nC_{60} stock suspension was prepared using a similar method to that described by Andrievsky et al. [102]. First, approximately 35 mg of C_{60} powder was dissolved in 30 mL toluene, forming a clear, dark purple solution. Then, 5 mL of this mixture was introduced into a beaker containing 50 mL deionized water, forming two distinct phases. This solution was then sonicated (Fisher Sonic Dismembrator 300, Pittsburgh, PA) for more than 3 hours in a fume hood to allow for evaporation of the toluene. The beaker was topped off with deionized water every 20 minutes to account for the evaporated water. The resulting transparent, brown-yellow liquid was filtered through 0.22 μm pore size membrane filter paper (Fisher, GSWP02500), resulting in a clear, bright yellow liquid. This method was

repeated a total of 6 times to produce approximately 330 mL of nC_{60} stock suspension. The resulting nC_{60} stock suspension was determined to have a total carbon content (Shimadzu TOC-V CPH/CPN, Columbia, MD) of 30.48 mg/L and an unadjusted pH of 5.5. The suspension was stored in the dark at 4 °C for the entirety of the study. All experiments took place within 3 months of preparing the nC_{60} stock suspension, during which time the particle size was stable, as confirmed by periodic Dynamic Light Scattering (DLS) monitoring (Malvern Zetasizer Nano ZS, Worcestershire, UK).

Fifty milligrams of dry HHA was introduced into 400 mL deionized water and stirred for more than 3 hours. During this time, the pH was adjusted drop wise with 0.1 N NaOH to a pH of 10.0 to allow the HHA to completely dissolve. After 3 hours and complete dissolution of the HHA, the pH was adjusted drop wise with 0.1 N HCl down to a pH of 6.7 and filtered through 0.22 μm pore size membrane filter paper. The stock solution was then diluted to 500 mL total volume, including the addition of NaCl and phosphate buffer to make a 0.1 g/L HHA, 70 mM NaCl, and 2 mM phosphate buffer solution.

Fifty milligrams of dry HFA was introduced into 400 mL of deionized water and stirred for more than three hours. Once the HFA had completely dissolved, the pH was adjusted drop wise with 0.1 N NaOH to a pH of 6.7 and filtered through 0.22 μm pore size membrane filter paper. The stock solution was then diluted to 500 mL total volume, including the addition of NaCl and phosphate buffer, to make a 0.1 g/L HFA, 70 mM NaCl, and 2 mM phosphate buffer solution.

Using DLS, the intensity weighted hydrodynamic diameter of the HHA and HFA particles in solution was determined to be 247 and 390 nm, respectively. Also using DLS, the zeta potential of the HHA and HFA particles were determined to be -43 and -12 mV, respectively, based on 14 independent measurements. Both solutions were stored at room temperature in the dark for the entirety of the study, during which time the particle size was stable, as confirmed by periodic DLS monitoring. The HHA and HFA used in this study were characterized in a previous publication by DeLapp et al. [101] and the elemental and

functional group analysis are provided in Tables A.1 and A.2 (A.1).

2.2.3 nC_{60} attachment experiments

The deposition of nC_{60} nanoparticles onto silica surfaces with and without HHA and HFA coatings was explored using a Quartz Crystal Microbalance with Dissipation Monitoring (QCM-D, Q-Sense E4 unit, Biolin Scientific, Stockholm, Sweden). The unit consists of 4 flow modules, each containing a 5 MHz AT-cut quartz crystal sensor. Flowrates were 0.1 mL/min, ensuring laminar flow within the flow module. Temperatures of the solution and flow module were maintained at $\pm$ 0.02 °C by a Peltier element.

The cleaning protocol for the QCM-D sensors is as follows. Before each experiment, the silica coated quartz sensors (QSX303) were soaked in a 2 % Hellmanex II (Hellma Analytics, Mullheim, Germany) solution overnight, rinsed with copious amounts of deionized water, dried with ultrapure N_2 gas, and then cleaned in a UV-Ozone cleaner (Jelight 42 UVO Cleaner, Irvine, CA) for 20 minutes. Immediately after cleaning, the sensors were loaded into the QCM-D for execution of the experiment.

A representative nC_{60} deposition experiment protocol is illustrated in Fig. 2.1. The background solution, 70 mM NaCl and 2 mM phosphate buffer, was flowed over the surface of the sensors until a stable baseline was achieved. The signal was considered stable when the third overtone frequency (f_3) failed to drift more than 0.3 Hz over the course of 10 minutes. Once a stable baseline was achieved, 2 mL of a 0.1 g/L PLL solution that contained the same electrolyte and buffer concentrations was flowed across the sensor surface. During this time, the PLL adsorbed to the silica surface very rapidly. The PLL layer was then rinsed with 2 mL of the background solution. If PLL was the final layer before nC_{60} deposition, the layer construction ended here. In the case of the HHA and HFA experiments, a solution of 0.1g/L HHA or HFA, containing the same electrolyte and buffer concentrations, was then flowed across the rinsed PLL layer until the signal once again stabilized, $\approx$20 minutes. During this time, the oppositely charged HHA or HFA macro-

molecules readily adsorbed onto the rinsed PLL layer, forming a second layer. The rapid adsorption of HHA or HFA onto the PLL layer usually resulted in a shift in f_3 of approximately 20 and 22 Hz, respectively. The mass of HHA and HFA deposited onto the sensor surface was calculated to be approximately 411 and 351 ng/cm^2, respectively, by the Voigt viscoelastic model [95]. A plot of the model calculated masses can be seen in Figure 2.5. Finally, the HHA or HFA layer was then rinsed with 2 mL of the background solution until a stable baseline was achieved. The layer construction portion of all experiments took place at 25 °C.

Once the layers were constructed, the temperature was adjusted to the desired temperature of the nC_{60} deposition experiment. All solutions used in each experiment were held at 2 °C above the set point temperature of the experiment for several hours before the experiment took place to ensure the solutions would not degas on the surface of the sensor. Once a stable baseline was achieved in the background electrolyte, measured amounts of the stock 1 M NaCl and 1 M phosphate buffer were added to the diluted stock nC_{60} suspension to make a nC_{60} concentration of 6 mg/L, with electrolyte and buffer concentrations matching all other solutions. The resulting diluted nC_{60} suspension was then immediately flowed into the flow module and across the surface of the sensor, allowing for nC_{60} deposition and attachment to the sensor surface.

As nC_{60} deposited onto the sensor surface, the mass continually increased, causing a continuous decrease in frequency, as described by the Sauerbrey Relation [93] (Eq. 2.1), where m is the mass of material deposited, C is the crystal constant (17.7ngcm^{-2}Hz^{-1}), and f_n is the frequency at overtone n. The first 120 seconds of frequency drop corresponding with nC_{60} deposition were considered in calculating the initial deposition rate at each experimental condition.

$$\Delta m = -C\frac{1}{n}\Delta f_n \tag{2.1}$$

While nC_{60} deposited onto the sensor surfaces, the first 120 seconds of the shift in the

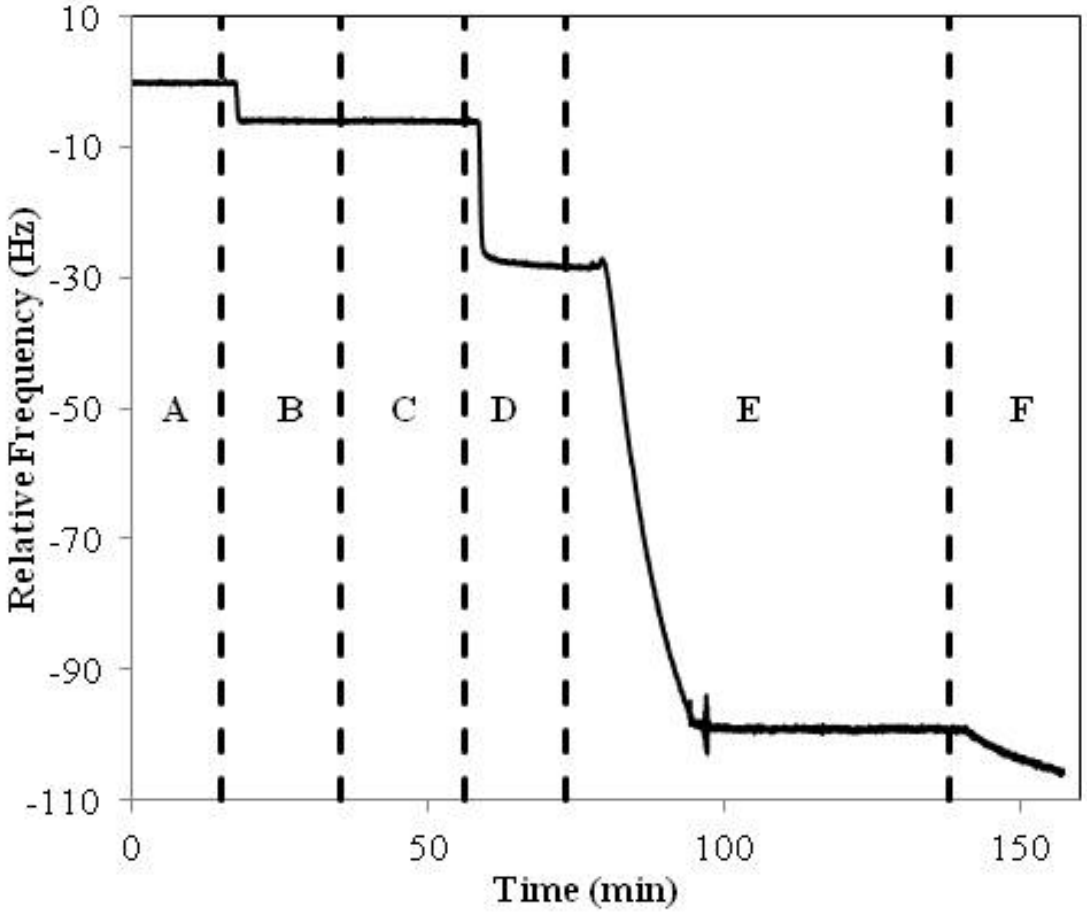

Figure 2.1: Representative nC_{60} deposition experiment. The initial baseline was collected in the background solution (A) before PLL was attached to the silica surface (B). The attached PLL was then washed in the background solution (C) before HHA was attached to the PLL surface (D). The attached HHA was then washed with background solution and the temperature of the sensor and chamber was lowered to 15 °C (E). Once a stable baseline was observed at the new temperature, the nC_{60} nanoparticle suspension with background solution was introduced and attached to the HHA surface (F).

third overtone of frequency (f_3) were used to calculate the initial deposition rates. In order to compare deposition rates at different experimental conditions independent of nC_{60} aggregation effects [61], the deposition rates were normalized by calculating the attachment efficiency factor (α). The attachment efficiency factor was calculated (Eq. 2.2) by normalizing the initial deposition rates to the corresponding initial deposition rate under favorable (nonrepulsive) conditions. Here, the favorable deposition rates are provided by the deposition rates of nC_{60} onto oppositely charged PLL layers at identical experimental conditions.

$$\alpha = \frac{df_3/dt}{\left(df_3/dt\right)_{fav}} \tag{2.2}$$

2.2.4 DLVO interaction energy calculations

By treating the nC_{60} deposition as a sphere-plate interaction, the total interaction energy between the nC_{60} particles and the silica sensor surface was estimated from the sum of the electrical double layer repulsion (V_R) and van der Waals attraction (V_A). Eq. 2.3 [103] was used to calculate the van der Waals attraction, where A is the combined Hamaker constant for the nC_{60} water silica system (4.71 x 10^{-21} J) [64], a is the radius of nC_{60} particles (Table A.3), h is the separation distance between the nC_{60} particle and silica sensor surface, and λ is the characteristic wavelength of interaction (usually assumed to be 100 nm) [104]. Mean values of particle diameter and zeta potential are used in all DLVO calculations.

$$V_A = -\frac{Aa}{6h}\left(1+\frac{14h}{\lambda}\right)^{-1} \tag{2.3}$$

Eq. 2.4 [103] was used to calculate the electrical double layer repulsion, where ε_0 is the dielectric permittivity in a vacuum, ε_r is the relative dielectric permittivity of water (Table A.3), ζ_p is the zeta potential of the nC_{60} particles (-27.2 mV, remained constant over the temperature range investigated according to DLS measurements (Fig. 2.4), ζ_c is the zeta

potential of the silica surface (-30 mV), and κ is the inverse Debye length.

$$V_R = \pi\varepsilon_0\varepsilon_r a\left\{2\zeta_p\zeta_c ln\left[\frac{1+exp(-\kappa h)}{1-exp(-\kappa h)}\right]+\left(\zeta_p^2+\zeta_c^2\right)ln\left[1-exp(-2\kappa h)\right]\right\} \tag{2.4}$$

Eq. 2.5 was used to calculate the inverse Debye length for the electrolyte system [104], where e is the elementary charge, n_j is the number concentration of ions in the bulk solution, z_j is ion valence, k is the Boltzmann constant, and T is the absolute temperature.

$$\kappa = \sqrt{\frac{e^2\sum n_j z_j^2}{\varepsilon_0\varepsilon_r kT}} \tag{2.5}$$

Since the nC_{60} particle radius and relative dielectric permittivity of water vary with temperature, the values used in Eqs. 2.3, 2.4, and 2.5 are summarized in Table A.3. The values for the relative dielectric permittivity of water were obtained from a study by Malmberg and Maryott [105].

2.3 Results and Discussion

2.3.1 Materials characterization

Investigation by Transmission Electron Microscopy (TEM) (Philips CM 20 TEM, Eindhoven, Netherlands) suggested the particles were polydisperse, as seen in Fig. 2.2, where representative images of an aggregate (left image) and individual particles (right image) are shown. DLS measurements confirmed a polydisperse particle distribution with an intensity weighted, mean hydrodynamic diameter of the nC_{60} nanoparticles of 103 nm based on 14 independent measurements and a zeta potential of -42 mV, based on 20 independent measurements. The zeta potential of the suspension was measured over a pH range of 3–10 and the results remained negative over the entire pH range investigated. Figures A.1 and A.2 (A.2) summarize particle size distribution and zeta potential measurements.

The nC_{60} suspension was also characterized throughout the temperature range investigated in this study. The nC_{60} particle size and zeta potential as a function of temperature can be seen in Fig. 2.3 and 2.4, respectively. The figures illustrate that there was no significant change in nC_{60} particle size or zeta potential observed throughout the temperature range investigated.

The mass of the layers formed by depositing HHA and HFA were determined to be approximately 411 and 351 ng/cm^2, respectively, by the Voigt viscoelastic model [95]. A plot of the model calculated masses can be seen in Fig. 2.5. The SOM layers were further characterized thermally, to ensure that the high temperatures did not facilitate desorption of the SOM layers, which would in turn affect nC_{60} deposition. After the layers were constructed, as described in 2.2.3, they were taken through a temperature ramp which encompassed the entire temperature range of the experiment. Upon cooling the SOM layers, the frequency curve returned to its original value in each case, meaning the mass of the layers remained unchanged and desorption was not observed. Representative heating/cooling curves for HHA and HFA can be seen in Fig. 2.6 and 2.7, respectively.

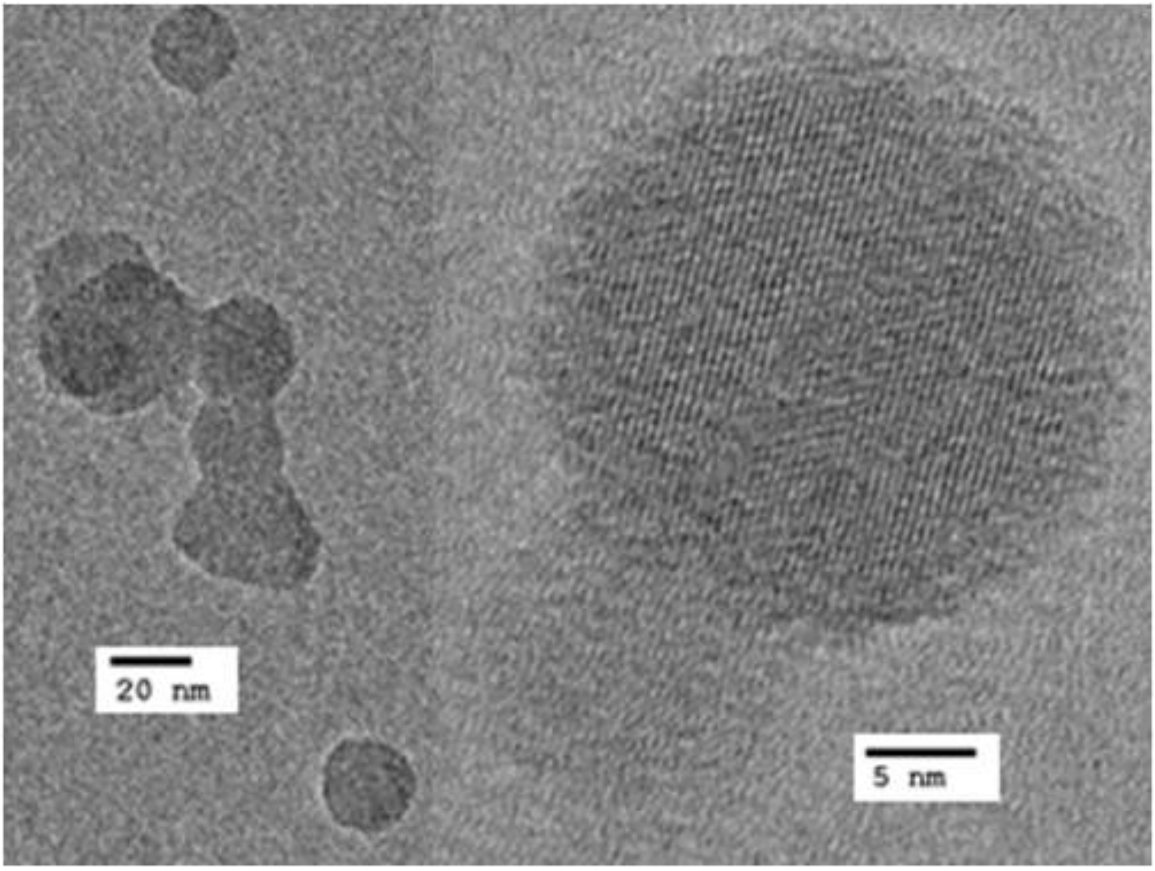

Figure 2.2: Representative nC_{60} TEM images.

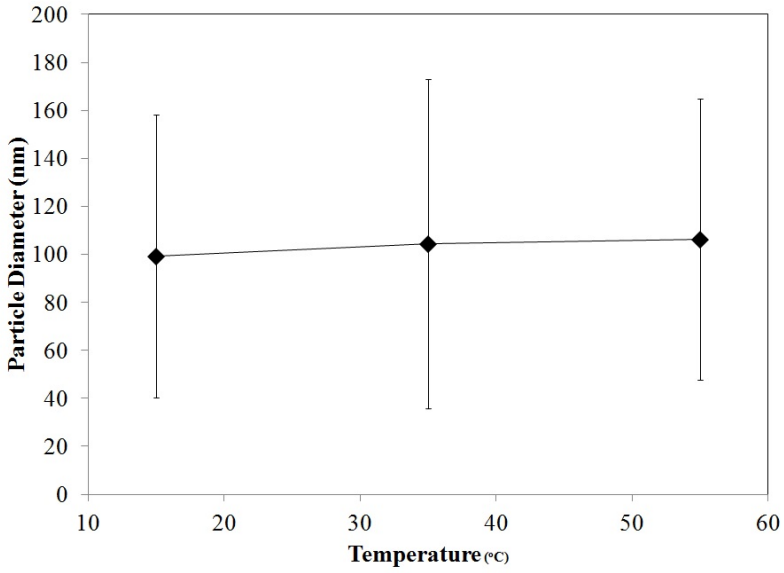

Figure 2.3: Mean hydrodynamic particle diameter of the nC_{60} stock suspensions as a function of temperature. Each point represents 20 independent measurements and error bars represent standard deviation.

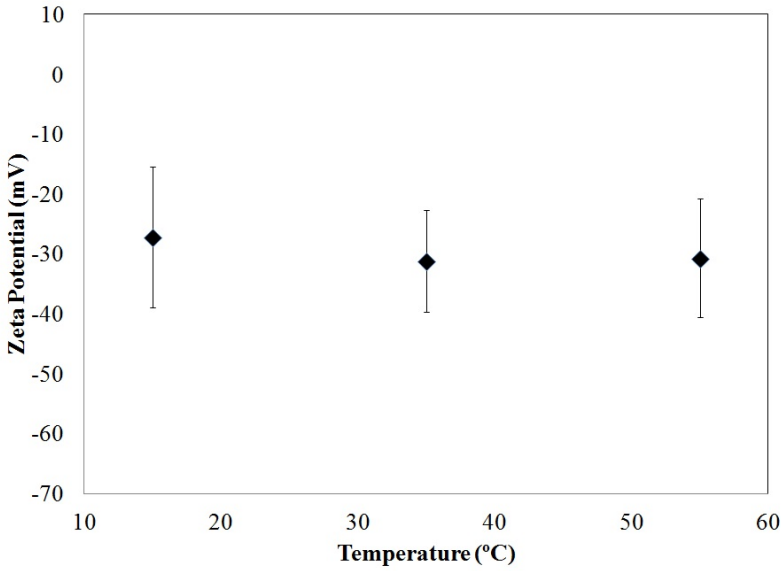

Figure 2.4: Zeta potential of the nC_{60} stock suspension as a function of temperature. Each point represents 14 independent measurements and error bars represent the standard deviation.

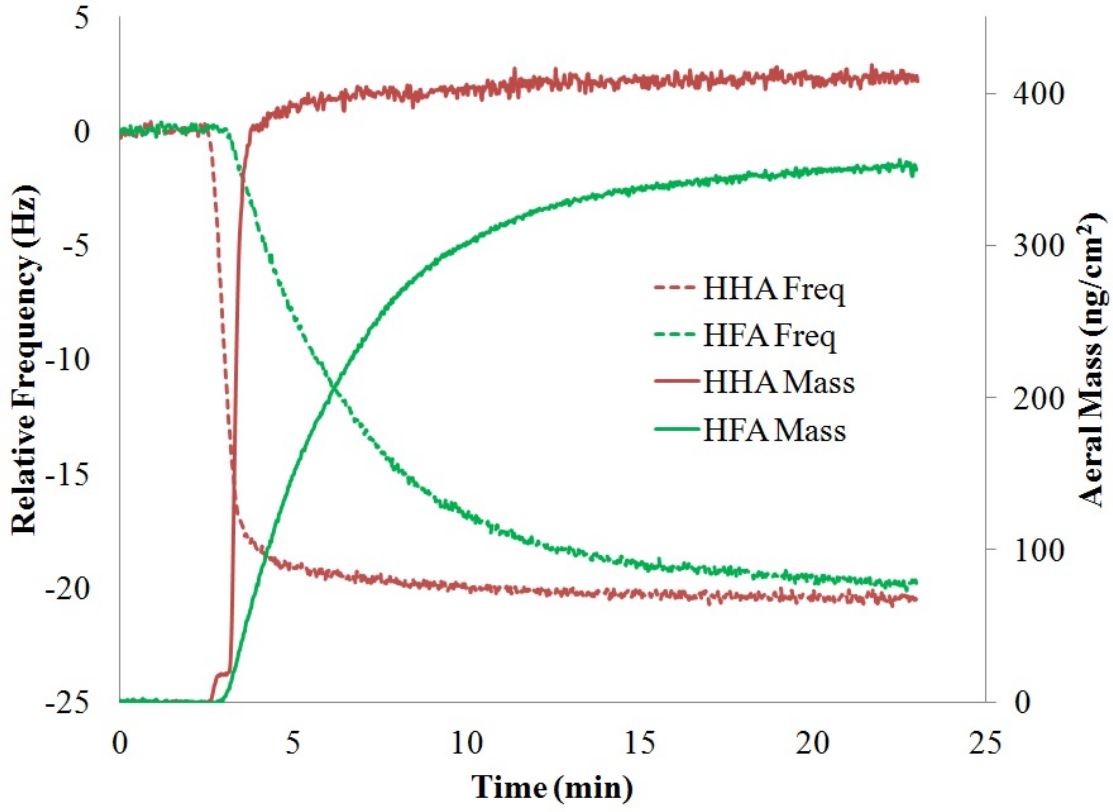

Figure 2.5: Calculated mass of the HHA and HFA layers, by the Voigt viscoelastic model.

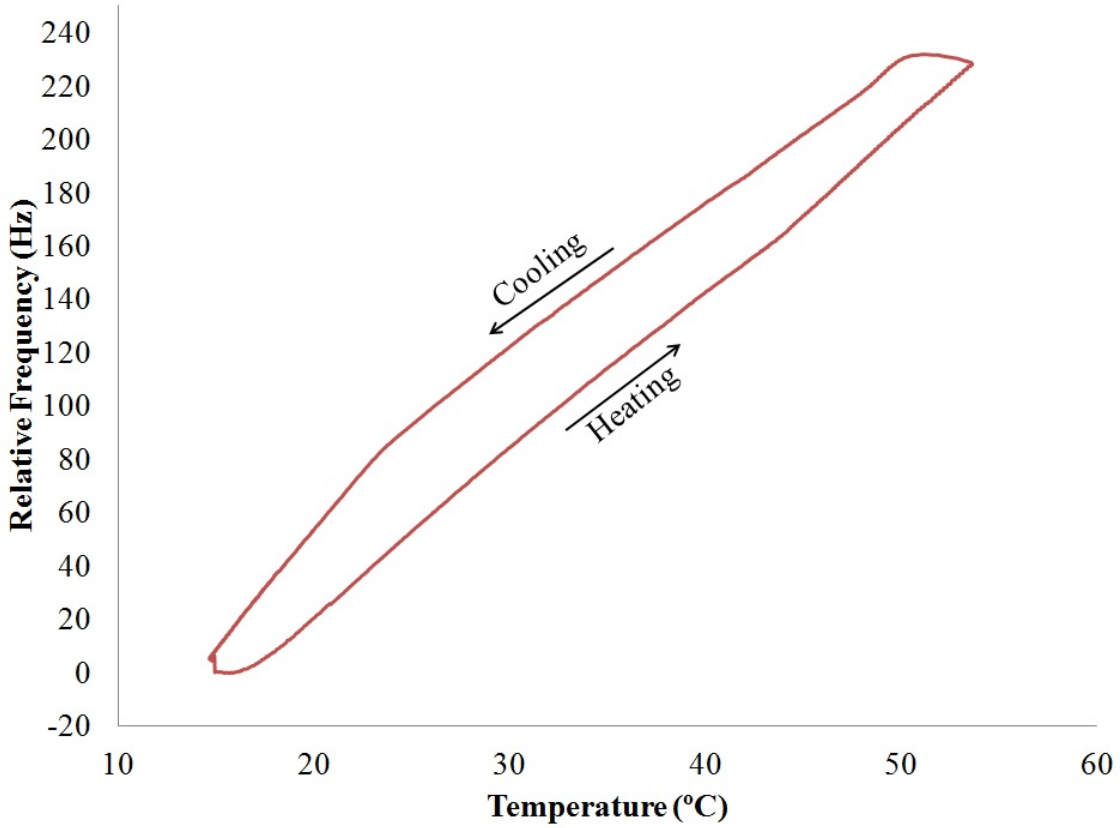

Figure 2.6: The heating/cooling loop of HHA, showing no change in mass over the temperature range investigated.

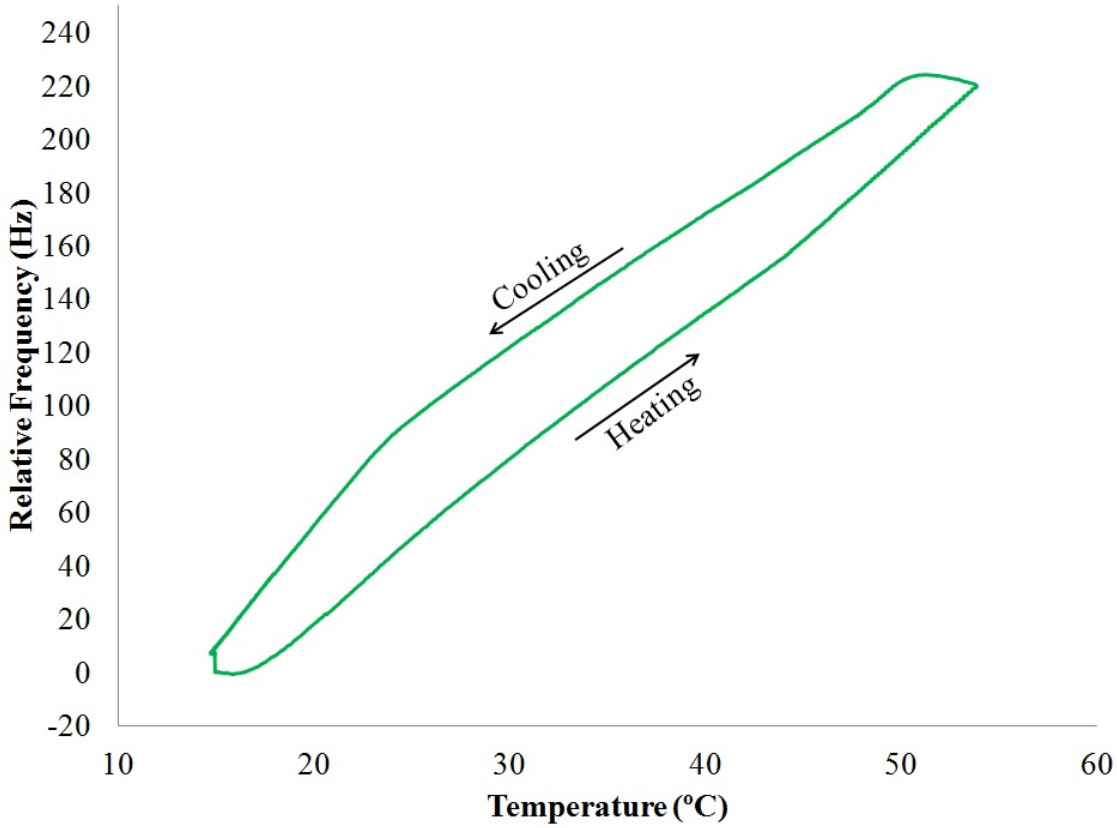

Figure 2.7: The heating/cooling loop of HFA, showing no change in mass over the temperature range investigated.

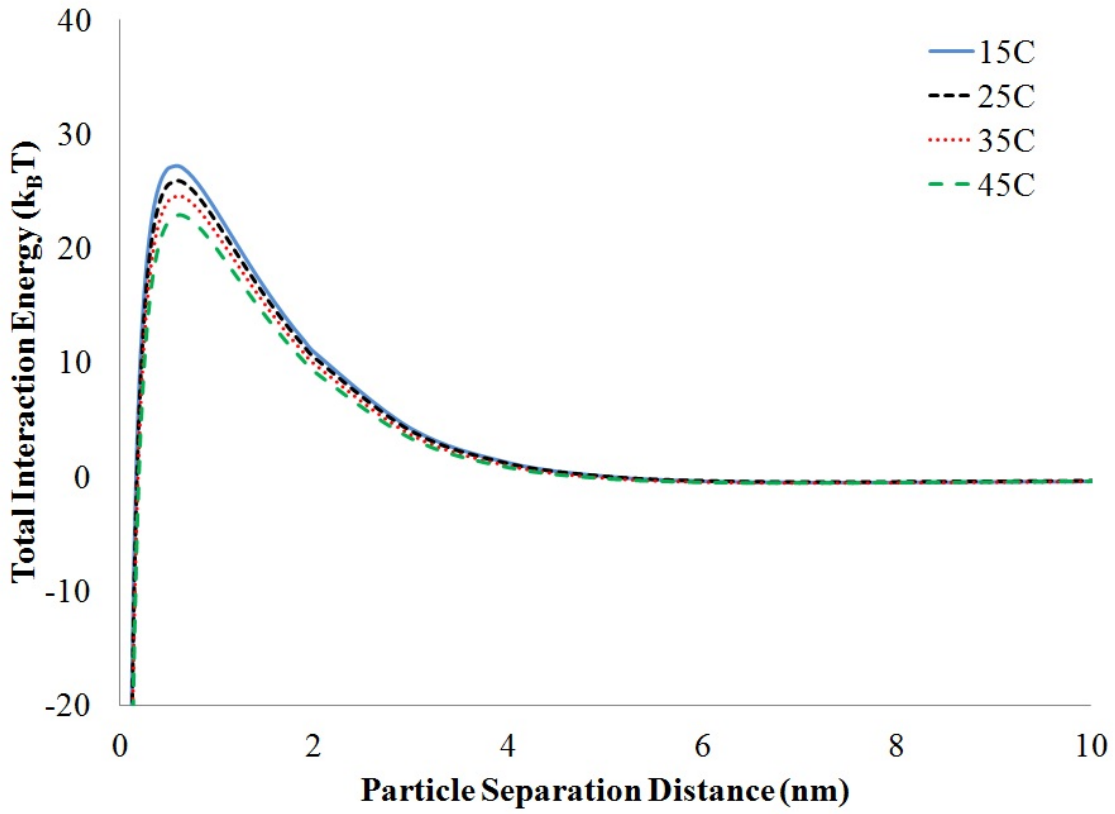

Figure 2.8: Calculated DLVO interaction energy profiles as nC_{60} approaches a bare silica surface.

2.3.2 nC_{60} attachment analysis

The deposition behavior of nC_{60} onto bare silica has been shown to be in qualitative agreement with DLVO theory [61], therefore the total interaction energy profiles for nC_{60} approaching a bare silica surface were calculated for each temperature investigated and presented in Fig. 2.8. As temperature increases, the total interaction energy profiles remain very similar, except for a small decrease in the energy barrier.

For the first time, the attachment efficiency factors of nC_{60}, onto three different surfaces, as a function of temperature are presented in Fig. 2.9. The bare silica attachment trend appears rather flat, with a small net increase, though the total increase does not fall outside the error of the measurements. This can be considered relatively consistent with DLVO predictions (Fig. 2.8), as the energy barrier shows a small decrease with increasing

temperature, which could lead to a negligible increase in attachment. The presence of HHA and HFA coatings cause significant deviations from the bare silica trend. Compared to the attachment onto bare silica, both HHA and HFA hinder nC_{60} attachment at lower temperatures, while HHA enhances attachment at higher temperatures. At the highest temperature investigated, HHA greatly enhances attachment while HFA appears to marginally enhance it, including a very slight overlap of error bars with the bare silica curve. The HHA and HFA trends continuously increase with increasing temperatures, though the rate of increase appears complex, presumably due to the change in physicochemical properties of the SOM layers over the temperature range investigated. The HHA trend displays a rate increase throughout the temperature range investigated, while the HFA trend appears to level off and then recover. The largest increase in attachment for both surfaces occurs in the temperature range of 35–45 °C. This suggests that the SOM layers undergo the largest change in physicochemical properties in this region. Previous studies of the HHA and HFA have illustrated thermal transitions within this region [101], however these studies investigated the materials as a dry, bulk powder. In our current work, the HHA and HFA are examined as thin, hydrated layers, bringing into account additional variables and, because of this, the degree to which these studies apply to the current work is unknown.

2.3.3 Thermal effects on attachment

In order to understand the deviation in attachment onto the HHA and HFA surfaces, the thermal properties of the SOM layers were investigated using the QCM-D. This is a particularly novel approach because the QCM-D has never before been used to thermally characterize SOM layers. First, each SOM layer was constructed following the same procedure as executed for the deposition experiments and as described previously. Then, the layer was exposed to a temperature ramp covering the entire temperature range of this study. The density and viscosity of water are a function of temperature, so the response of the sensor submerged in a solution is also expected to change as a function of temperature

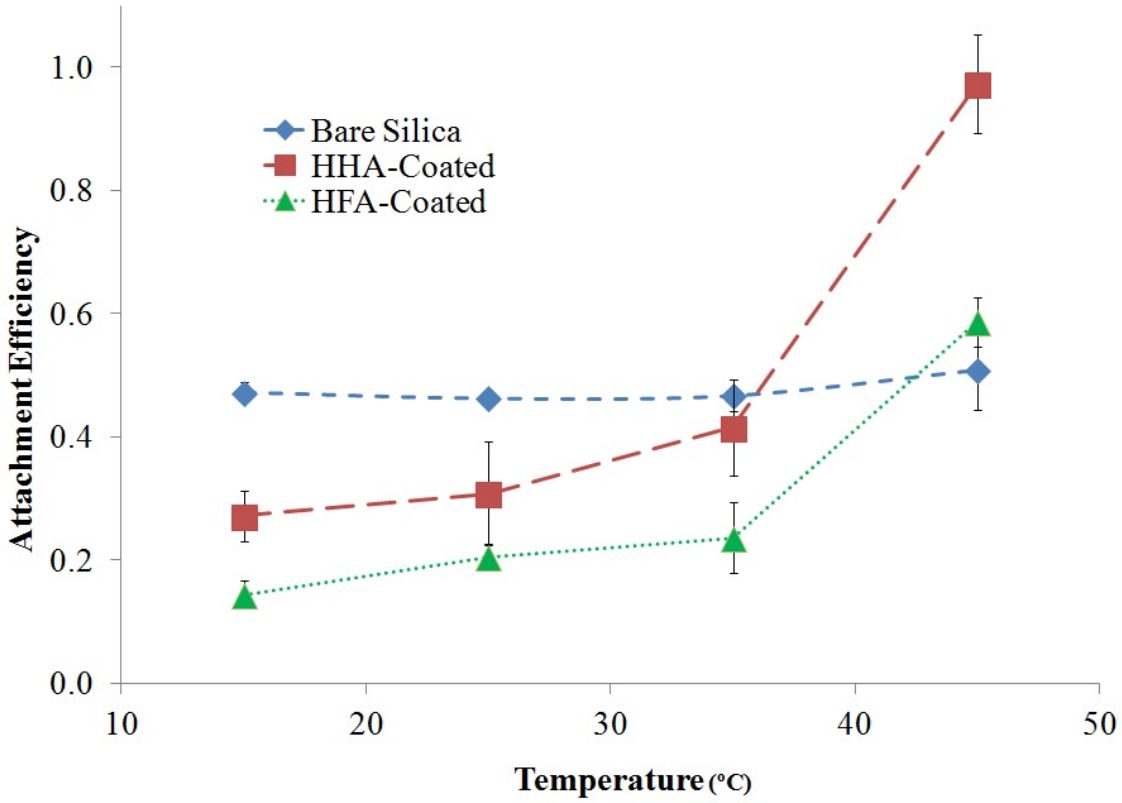

Figure 2.9: nC_{60} attachment efficiencies onto bare, HHA-coated, and HFA-coated silica sensors as a function of temperature. Error bars represent the standard deviation.

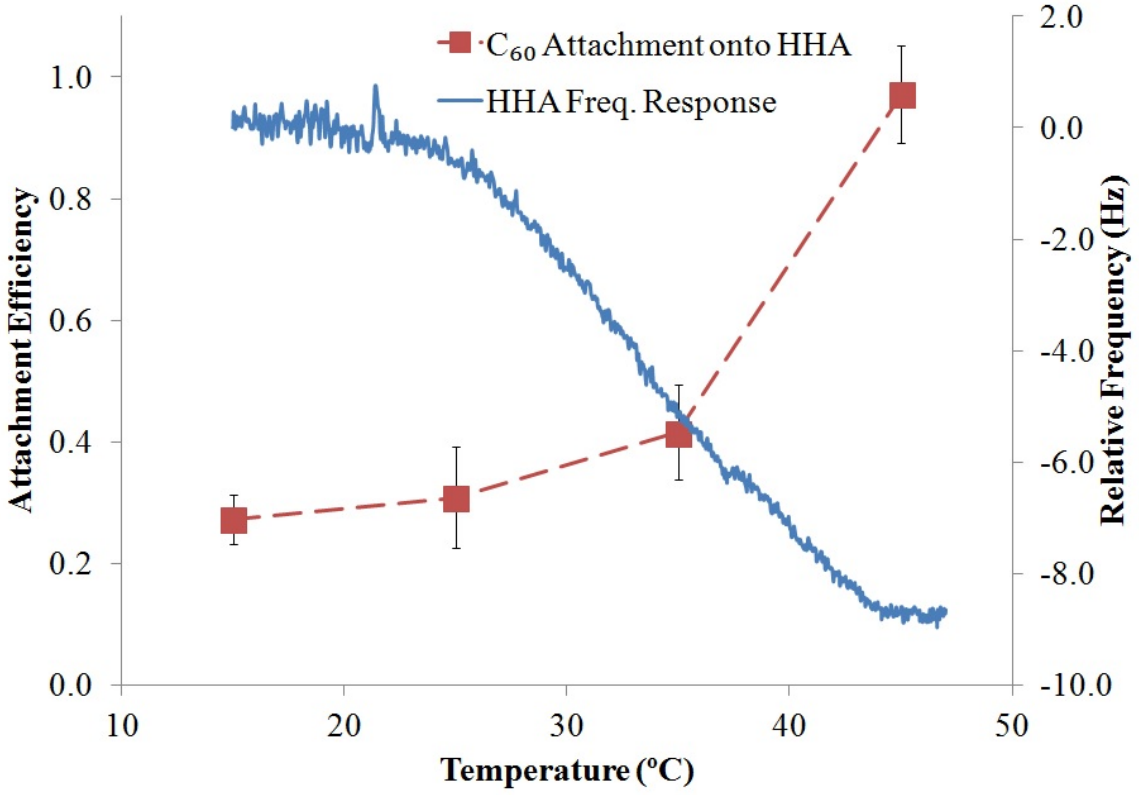

Figure 2.10: Thermal characterization of the HHA layer by QCM-D, with all bulk solution and sensor effects subtracted, compared to the corresponding nC_{60} attachment efficiency trend. The 3rd overtone of frequency is displayed.

[106]. In order to isolate the effects caused only by changes in each SOM layer, the same bare sensor was first taken through an identical temperature ramp and its response was subtracted. In this manner, the QCM-D was utilized to thermally characterize a thin layer of SOM. The frequency curves displayed in Figs. 2.10 and 2.11 represent the response of the HHA and HFA layers, respectively, to a change in temperature. By comparing the SOM layer frequency response to the corresponding nC_{60} attachment trend, we can gain insights into the mechanisms by which the attachment onto each SOM layer deviates from that of bare silica.

The frequency curve provides insight into the mass changes of the layer, including any water molecules that are hydrating the layer. The overall trend of each frequency curve is downwards, indicating an increase in mass (see Eq. 2.1), attributable to the hydration of the

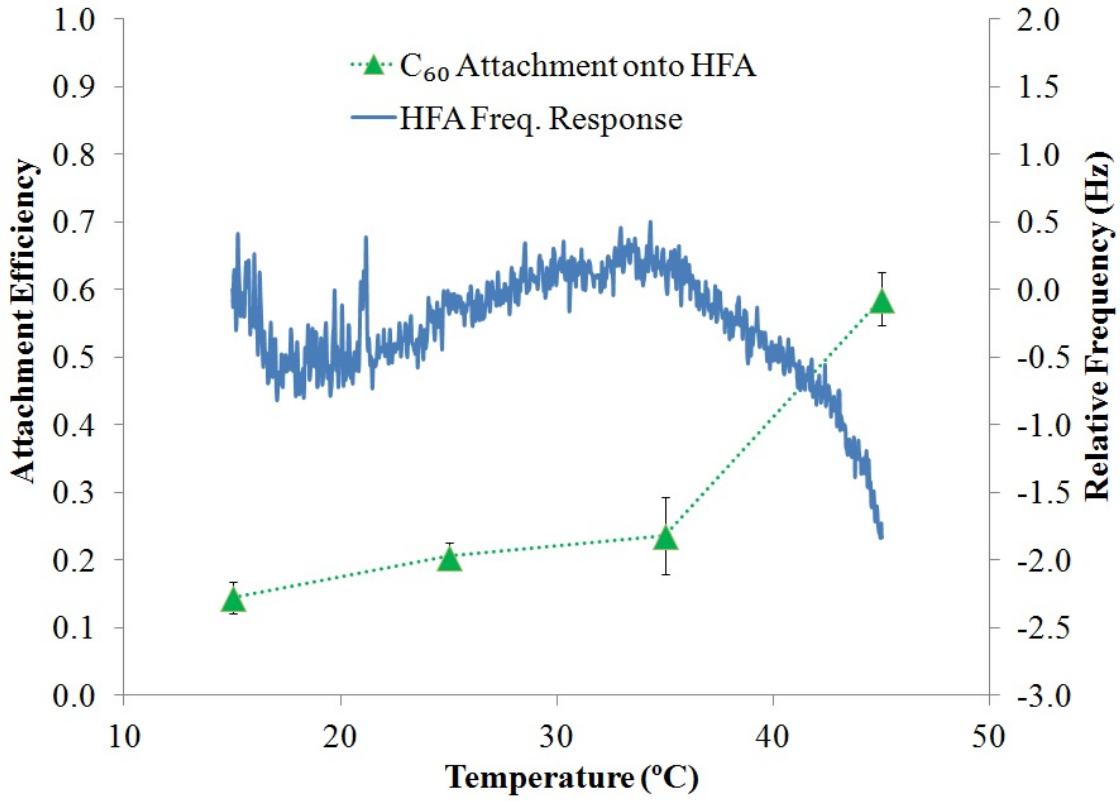

Figure 2.11: Thermal characterization of the HFA layer by QCM-D, with all bulk solution and sensor effects subtracted, compared to the corresponding nC_{60} attachment efficiency trend. The 3rd overtone of frequency is displayed.

SOM layer at increasing temperatures. The observed increase in hydration with increasing temperature is in agreement with a study by Vidyasagar et al. [107], which investigated the thermal characteristics of a polyectrolyte using a similar QCM-D method. As indicated by Figs. 2.10 and 2.11, an increase in hydration (decrease in frequency) corresponds with an increase in attachment for both SOM layers investigated. As the HHA layer begins to hydrate between 15–25 °C, the attachment shows a small increase (Fig. 2.10). As the HHA continues to hydrate more rapidly between 25–35 and 35–45 °C, the attachment also results in a sharper increase. As the HFA layer begins to hydrate in the range of 15–25 °C, the attachment begins to rise as well (Fig. 2.11). As the HFA hydration rate slows and begins to reverse in the range of 25–35 °C, however, the increase in attachment slows and begins to level off. The lack of an observable decrease in attachment in this region suggests that the interaction is a complex one, relying on more than just hydration of the layer. As the HFA layer resumes a rapid hydration rate between 35–45 °C, the attachment shows a correspondingly rapid increase. For these reasons, Figs. 2.10 and 2.11 clearly illustrate a strong correlation between SOM layer hydration and resulting nC_{60} attachment efficiency, which, to our knowledge, has not been illustrated for ENMs.

An increase in hydration of the SOM layers at higher temperatures contribute to the increased attachment behavior through water-assisted disruption of polar SOM contacts, as described by Graber and Borisover [37]. As hydration increases, water molecules penetrate the SOM matrix and reach polar areas that were previously unavailable to nC_{60} attachment, due to inter- or intra-molecular interactions. By hydrating these areas, the water molecules disrupt the interactions between these contacts and provide a new contact for attachment, which was previously unavailable. This effect has been illustrated for the sorption of HOCs by a Pahokee peat hydrated by water [37] and other polar solvents [36]. The results of the current study illustrate a similar effect for the attachment of nC_{60} by two different humics, bringing into account more complexity in the environmental fate and transport of nC_{60}.

Another possible contributing factor to the observed increase in attachment involves

the swelling of the SOM layer. At higher temperatures the SOM layers expand or swell due to increased thermal motions and apparent increased hydration, much like the matrix relaxation observed in previous studies [29, 32]. Swelling will increase the volume of the layers, allowing them to take a more extended conformation from the surface of the sensor and also provide an increasingly cross-linked or bridged mesh of organic matter for the nC_{60} particles to become entangled in. At lower temperatures, the SOM layers dehydrate, which compacts the layer. This compacted layer likely has a more condensed, less extended (smoother) surface with reduced potential for nC_{60} particle entanglement, effectively lowering attachment efficiency (Fig. 2.9). This finding is in agreement with a study by Chen and Elimelech [66] which investigated the deposition of nC_{60} onto an alginate coated silica surface. When the alginate was exposed to a higher electrolyte concentration, the layer compacted and resulted in lower attachment efficiency.

2.4 Conclusions

In this study, we have shown that the attachment of nC_{60} to immobilized layers of HHA and HFA is greatly affected by temperature and that the trend in attachment efficiency onto the SOM layers deviate greatly from that of bare silica. The attachment efficiency onto both SOM layers hinder attachment at low temperatures and then begin to rise as temperatures increase, eventually resulting in enhanced attachment at high temperatures, in the case of the HHA layer. (Fig. 2.9). Based on thermal characterization of the SOM layers compared to the corresponding attachment trends (Figs. 2.10 and 2.11), the attachment efficiency is strongly correlated with hydration of the layer. Regions of rapid hydration correspond to steep increases in attachment and regions of slowed or decreased hydration correspond to lower increases in attachment. Possible mechanisms explaining this phenomenon include water-assisted disruption of polar SOM contacts and hydration induced swelling of the SOM matrix. This thermal effect on the attachment of nC_{60} to SOM may prove to be crucial in understanding the fate and transport of ENMs in areas that are rich in SOM, like the subsurface environment, because humic substances typically represent the dominant organic components in soils and sediments [14]. In areas that see large temperature fluctuations throughout the year, we may see a much larger uptake of ENMs in the warm seasons and less uptake in the cold seasons. Understanding how ENMs interact with individual components of soil is crucial to understanding the fate and transport of ENMs in a complex soil system, leading to their eventual impact on ecosystem and human health. The thermal effect illustrated in the current study may also prove useful in the removal of similar ENMs from wastewater or drinking water, by exploiting the much higher attachment efficiency at increased temperatures. Further studies need to be carried out, however, to investigate the relative importance of other variables which may play a role in ENM interactions with SOM.

Chapter 3

nC_{60} deposition onto humic acid coated silica and the effect of ionic strength

3.1 Introduction

The popularity of engineered nanomaterials (ENMs) has grown rapidly over the last decade, with the ENM market expected to reach a total of $64.2 billion over the next five years [1]. This increase in production will certainly lead to the eventual release of ENMs into the environment through production and manufacturing of the products or use and disposal from the consumer [108]. One particular ENM of note is buckminsterfullerene (C_{60}), which has applications throughout many fields, including biomedical technology, electronics, and optics [2, 3]. Since the solubility of fullerene in water is very low [98], the nano-sized colloidal particle it forms in water (nC_{60}) is the most environmentally relevant form to study. The antimicrobial properties, aquatic toxicity, and potential human toxicity of nC_{60} [3, 9, 10, 109] combined with the inevitable release to the environment raise serious concerns about the environmental fate and transport of nC_{60}.

As with other colloidal particles, the transport of nC_{60} throughout the environment will be determined by its aggregation and deposition processes. These processes are controlled by a complex system of variables including ionic strength, the presence of organic matter, and pH [56]. The aggregation behavior of nC_{60} in clean systems (absent of organic matter) is usually described by the classic Derjaguin-Landau-Verwey-Overbeek (DLVO) theory [58, 59], which describes the stability of aqueous colloids by combining the effects of an electrical double layer repulsion (EDL) and a van der Waals (vdW) attraction. An increase in ionic strength screens the EDL repulsion and lowers the energy barrier to aggregation. Furthermore, the Schulze-Hardy rule [60] states that the valence (z) of counterions play a major role as well, predicting the critical coagulation concentration (CCC) to be proportional to z^{-6}. The aggregation behavior of nC_{60} has been shown to be in agreement with

DLVO theory both in terms of sensitivity to ionic strength and proportionality to z [50, 61].

The deposition of nC_{60} occurs when nC_{60} particles collide with and sorb to an immobile surface in the complex subsurface environment. Relative to the nC_{60} particles, these mineral and soil surfaces can be considered infinitely large particles and therefore deposition can be studied as a form of heteroaggregation [60]. Several studies have monitored the deposition of nC_{60} using both quartz crystal microbalance with dissipation monitoring (QCM-D) [50, 61, 64, 66] and packed column experiments [64, 67, 73, 110–112], however most were conducted in a simple electrolyte system with bare mineral surfaces. As ionic strength increased in the aforementioned QCM-D studies, the attachment efficiency of nC_{60} onto silica surfaces increased until reaching a maximum of 1 at the CCC, suggesting qualitative agreement with DLVO theory. Additionally, two of these studies [61, 66] reported a much larger charge screening effect when a divalent cation (Ca^{2+}) was introduced, suggesting qualitative agreement with the Schulze-Hardy rule. DLVO theory describes the deposition of nC_{60} well in these clean systems, however the subsurface often contains additional variables for consideration, namely the presence of organic matter.

Soil organic matter (SOM) is ubiquitous in the subsurface environment, either dissolved or immobilized (attached) onto the surface of mineral and soil surfaces and humic substances typically represent the dominant organic components in soils and sediments [14]. Dissolved organic matter has been shown to adsorb onto the surface of nC_{60} particles and increase their stability to aggregation and deposition through steric repulsion [50, 66] and, in turn, increase their mobility. The effect of attached soil organic matter (SOM) layers on the deposition behavior of nC_{60}, however, appears to be much more complex. The presence of attached SOM layers has been shown to enhance, hinder, or have no effect on the attachment of nC_{60}, depending on the type of SOM and the ionic strength of solution [50, 64, 66]. One study reported that an alginate layer enhanced nC_{60} attachment in the presence of 10 mM NaCl, while hindering it in the presence of 30 mM NaCl [66]. The variable behavior was attributed to its compaction at higher NaCl concentrations, resulting

in a smoother, more rigid layer, with less room for nC_{60} particle entanglement. Furthermore, in our previous work, we reported that increasing the temperature of a humic acid layer while holding all other variables constant, raised the attachment efficiency of nC_{60} from low attachment ($\alpha = 0.3$) to complete attachment ($\alpha = 1$) [39]. We attributed this to the temperature-dependent hydration of the layer, opening up previously unavailable sorption sites. Since the interaction between nC_{60} and environmentally relevant surfaces will likely play a very important role in the fate and transport of nC_{60} throughout the environment [113], it is clear that more study is needed in order to understand what role attached SOM layers will play.

The purpose of this study is to further the understanding of nC_{60} deposition behavior in the presence of attached SOM layers. By varying the ionic strength of the system, through both ion concentration and valence, while holding all other variables constant, the deposition rate of nC_{60} is directly monitored using a QCM-D. Deposition rate and attachment efficiency curves are then constructed over a range of ion concentrations and valences. By comparing these curves between surfaces of bare silica and humic acid coated silica, the role of ionic strength in nC_{60} deposition onto SOM layers is elucidated, discussed, and compared to DLVO theory. Combined with our previous work regarding the role of SOM layer physicochemical properties [39], this study illustrates the importance of attached SOM layers in the transport of nC_{60} and the need for a better quantitative understanding of its role. A better understanding of these interactions would lead to more precise predictions on the potential pathways of exposure and their eventual impact on ecosystems and human health.

3.2 Materials and Methods

3.2.1 Materials

Sublimed C_{60} powder (>99.9%) was purchased from MER Corporation (Tucson, AZ). Dry Harpeth humic acid (HHA) was isolated as described in our previous publication [101]. Poly-L-lysine hydrobromide (PLL, P1274) and 4-(2-Hydroxyethyl)-1-piperazineethanesulfonic acid (HEPES) were purchased from Sigma-Aldrich (St. Louis, MO). Reagent grade NaCl (S671) and $CaCl_2$ (C79) were purchased from Fisher Scientific (Pittsburgh, PA). Silica-coated QCM-D sensors (QSX-303) were purchased from Q-Sense (Biolin Scientific, Stockholm, Sweden). 900 nm silica microspheres were purchased from Polysciences Inc (Warrington, PA) as a surrogate for estimating the electrophoretic mobility of the silica sensor surface. All solutions were prepared using ultra pure water purified by the Milli-Q Water Purification System from Millipore (Billerica, MA).

3.2.2 Preparation of stock suspensions and solutions

The method used to produce the stock nC_{60} suspension in this study is similar to that provided by Andrievsky et al. [102] and identical to that used in our previous publication [39]. First, approximately 35 mg of C_{60} powder was dissolved in 30 mL toluene, forming a clear, dark purple solution. Then, 5 mL of this mixture was introduced into a beaker containing 50 mL deionized water, forming two distinct phases. This solution was then sonicated (Fisher Sonic Dismembrator 300, Pittsburgh, PA) for more than 3 hours in a fume hood to allow for evaporation of the toluene. The beaker was topped off with deionized water every 20 minutes to account for the evaporated water. The resulting transparent, brown-yellow liquid was filtered through 0.22 μm pore size membrane filter paper (Fisher, GSWP02500), resulting in a clear, bright yellow liquid. This method was repeated a total of 6 times to produce approximately 330 mL of nC_{60} stock suspension.

The resulting nC_{60} stock suspension was determined to have a total carbon content

(Shimadzu TOC-V CPH/CPN, Columbia, MD) of 33.6 mg L^{-1} and a pH of 5.6. The nC_{60} stock suspension was stored in the dark at 4 °C for the entirety of the study and all experiments took place within 4 months of preparation, during which time the nC_{60} stock suspension was stable as confirmed by periodic Dynamic Light Scattering (DLS) measurements (Malvern Zetasizer Nano ZS, Worcestershire, UK).

50 mg of dry HHA was introduced into 400 mL deionized water and stirred for more than 3 hours. During this time, the pH was adjusted drop wise with 0.1 N NaOH to a pH of 10.0 to allow the HHA to completely dissolve. After 3 hours and complete dissolution of the HHA, the pH was adjusted drop wise with 0.1 N HCl down to a pH of 5.6 and filtered through 0.22 μm pore size membrane filter paper. The stock solution was then diluted to 500 mL total volume to make for a concentration of 0.1 g/L HHA.

The HHA stock solution was kept in the dark for the entirety of the study, during which time the solution was stable as confirmed by periodic DLS measurements. The HHA used in this study has been extensively characterized by DeLapp et al. [101] and shown to undergo thermal transitions at elevated temperatures. Due to the constant temperature of 25 °C employed throughout this study, however, no such transition behavior is expected. All prepared solutions were filtered through 0.22 μm pore size membrane filter paper (Fisher, GSWP02500) and pH adjusted to 5.6, so that all experiments could take place at the unadjusted pH of the nC_{60} stock suspension.

3.2.3 nC_{60} aggregation kinetics

Since particle size can control the rate of diffusion, it is important to characterize the aggregation of nC_{60} under all experimental conditions. By mixing measured amounts of concentrated electrolyte and stock nC_{60} immediately before introduction into the DLS, the nC_{60} particle size at each experimental condition can be monitored over time. The nC_{60} concentration and pH were held constant at 6.1 mg L^{-1} and 5.6, respectively, for all experiments throughout this study in order to remain consistent with other relevant studies

[61, 64, 66] and environmentally relevant conditions. The particle size was monitored once per minute, with each point representing 10 independent measurements. In order to calculate the aggregation attachment efficiency factor (α_A) (Eq 3.1), the aggregation rate for each experimental condition was normalized by the aggregation rate under diffusion limited conditions. The aggregation rate under diffusion limited conditions was taken to be the aggregation rate at which an increase in ionic strength did not result in an increase in aggregation rate.

$$\alpha_A = \frac{{da_p}/{dt}}{\left({da_p}/{dt}\right)_{diff\ limited}} \tag{3.1}$$

3.2.4 Electrophoretic mobility measurements

In order to measure the electrophoretic mobility (EPM) of nC_{60} and silica under all experimental conditions, the DLS was used in combination with a universal dip cell (Malvern ZEN1002, Worcestershire, UK). Each reported EPM value was the result of 10 independent measurements. 900 nm silica micsospheres were used as a surrogate for the silica QCM-D sensor surface. EPM values were measured at each experimental condition for uncoated, PLL-coated, and HHA-coated silica particles. In order to coat the negatively charged silica particles with HHA, they were first coated with positively charged PLL, rinsed with DI water, and then coated with HHA. The silica particles were introduced into a 100 mg L^{-1} solution of PLL, stirred for 20 minutes, and then drained through a 0.45 μm pore size membrane filter (Fisher, GSWP02500) while rinsing in DI water, allowing the unbound PLL to pass through, leaving the coated silica particles behind. The process was then repeated for an HHA coating. The uncoated silica particles were also taken through an identical procedure without the addition of PLL or HHA, as a control. The silica concentration was 10 mg L^{-1} for all EPM measurements. Since the particle radius was much larger than the Debye length at each experimental condition investigated in this work, zeta potentials were estimated using the Smoluchowski approximation [114].

3.2.5 QCM-D experiments

The deposition rate of nC_{60} under varying experimental conditions was monitored using a QCM-D (Q-Sense E4 unit, Biolin Scientific, Stockholm, Sweden). Flowrates were 0.1 mL min^{-1}, ensuring laminar flow within the module, as confirmed by a Re of 0.26 (details can be found in B). Temperature was held constant at 25 $\pm$ 0.02 °C by a Peltier element. The nC_{60} concentration and pH were held constant at 6.1 mg L^{-1} and 5.6, respectively, for all experiments throughout this study in order to remain consistent with other relevant studies [61, 64, 66] and environmentally relevant conditions. Before each experiment, the silica coated quartz sensors were soaked in a 2% Helmmanex II solution (Mullheim, Germany) overnight, rinsed with copious amounts of DI water, dried with ultrapure N_2 gas and then cleaned in a UV-Ozone cleaner (Jelight 42, Irvine, CA) for 20 min. The QCM-D experimental protocol is explained in detail below and a representative experimental procedure is illustrated in Fig. 3.1.

For nC_{60} deposition experiments taking place on bare silica, the desired electrolyte type and concentration was first flowed across the sensor surface until a stable baseline was achieved. The signal was considered stable when the third overtone of frequency (f_3) failed to drift more than 0.3 Hz over the course of 10 minutes. The nC_{60} stock was then diluted to 6.05 mg/L with a measured amount of electrolyte to form the desired concentration and immediately introduced into the measurement chamber. As the nC_{60} flowed across the sensor surface, the first 120 seconds of the drop in frequency were used to calculate the initial deposition rates for each set of experimental conditions.

For nC_{60} deposition experiments taking place on PLL or HHA surfaces, the surfaces were first constructed using the following method. The initial baseline was collected in a buffer solution consisting of 10 mM HEPES and 100 mM NaCl. Then, 2 mL of a 0.1 g/L PLL solution was introduced, containing the same HEPES and NaCl concentrations. During this time, oppositely charged PLL attached rapidly to the surface, forming a positively charged layer. The PLL layer was then rinsed with 2 mL of the HEPES solution.

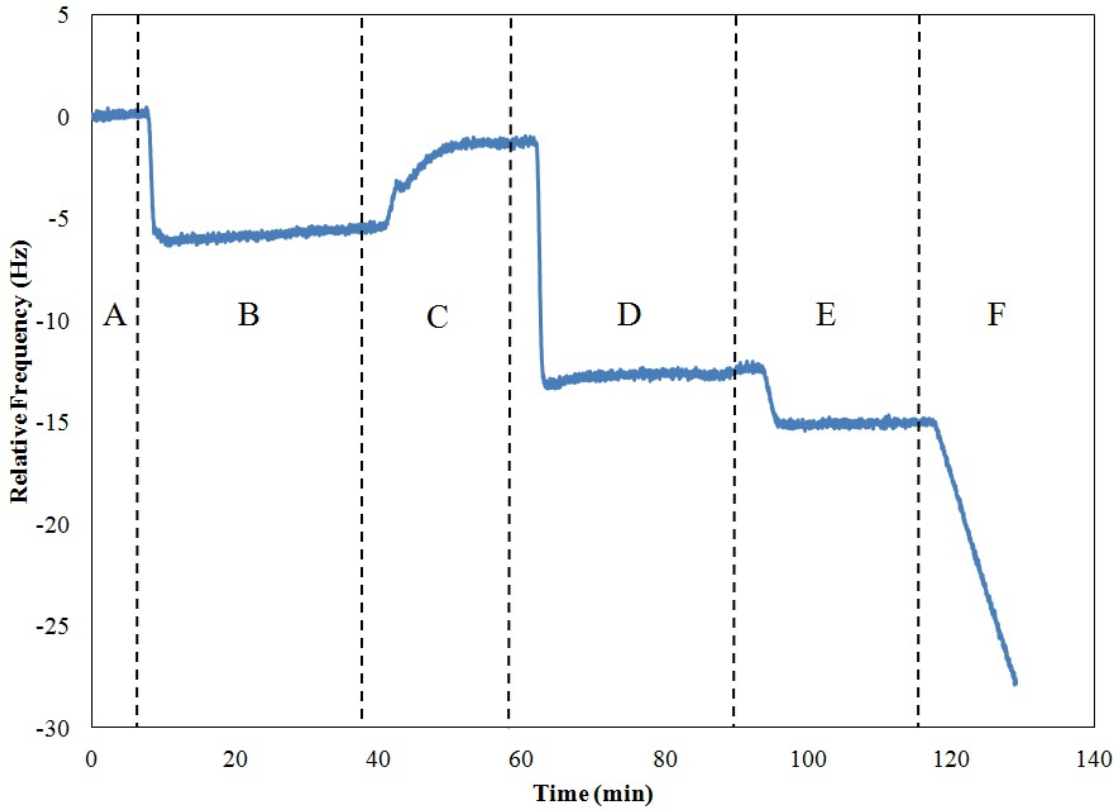

Figure 3.1: Representative nC_{60} deposition experiment. The initial baseline was collected in HEPES solution (A) before PLL was attached to the silica surface and rinsed in HEPES solution (B). The PLL layer was then rinsed in 1 mM NaCl (C) before HHA was attached to the PLL surface and rinsed in 1 mM NaCl (D). Finally, the HHA layer was rinsed in the electrolyte concentration at which the deposition experiment would take place (100 mM NaCl in this case) (E). Once a stable baseline was observed the nC_{60} was mixed with a premeasured volume of electrolyte to form the desired concentration (100 mM NaCl in this case) and immediately introduced onto the sensor surface (F).

If PLL was the terminal layer, then the nC_{60} deposition experiment proceeded from here, as described previously. If not, the PLL layer was then rinsed with 2 mL of 1 mM NaCl, followed by 2 mL of 0.1 g/L HHA. During this period, the negatively charged HHA attached rapidly to the oppositely charged PLL layer, forming a second layer. After the HHA layer was rinsed with 2 mL of 1 mM NaCl, the nC_{60} deposition experiment proceeded as described previously.

3.2.6 nC_{60} deposition kinetics

A continuous increase in mass during deposition results in a continuous decrease in frequency, as described by the Sauerbrey Relation [93], which can be seen in Eq. 3.2, where m is the mass of material deposited, C is the crystal constant (17.7 ng $cm^{-2}Hz^{-1}$), and f_n is the frequency at overtone n.

$$\Delta m = -C\frac{1}{n}\Delta f_n \tag{3.2}$$

In order to compare deposition rates under different experimental conditions, independent of nC_{60} aggregation effects, the deposition attachment efficiency factor was calculated (α_D) as seen in Eq. 3.3. The initial change of the third overtone of frequency with respect to time ($\frac{df_3}{dt}$) was calculated from the first 120 seconds of nC_{60} deposition. Since the nC_{60} particles are negatively charged at all experimental conditions examined (Fig. 3.2), any particles that flow near the positively charged PLL-coated surface will attach, meaning the deposition in this case is limited only by diffusive mass transport. Therefore, the diffusion limited deposition rate ($\left(\frac{df_3}{dt}\right)_{diff\ limited}$) was taken to be the nC_{60} deposition rate onto the PLL-coated surface at each corresponding experimental condition.

$$\alpha_D = \frac{{}^{df_3}\!/_{dt}}{\left({}^{df_3}\!/_{dt}\right)_{diff\ limited}} \tag{3.3}$$

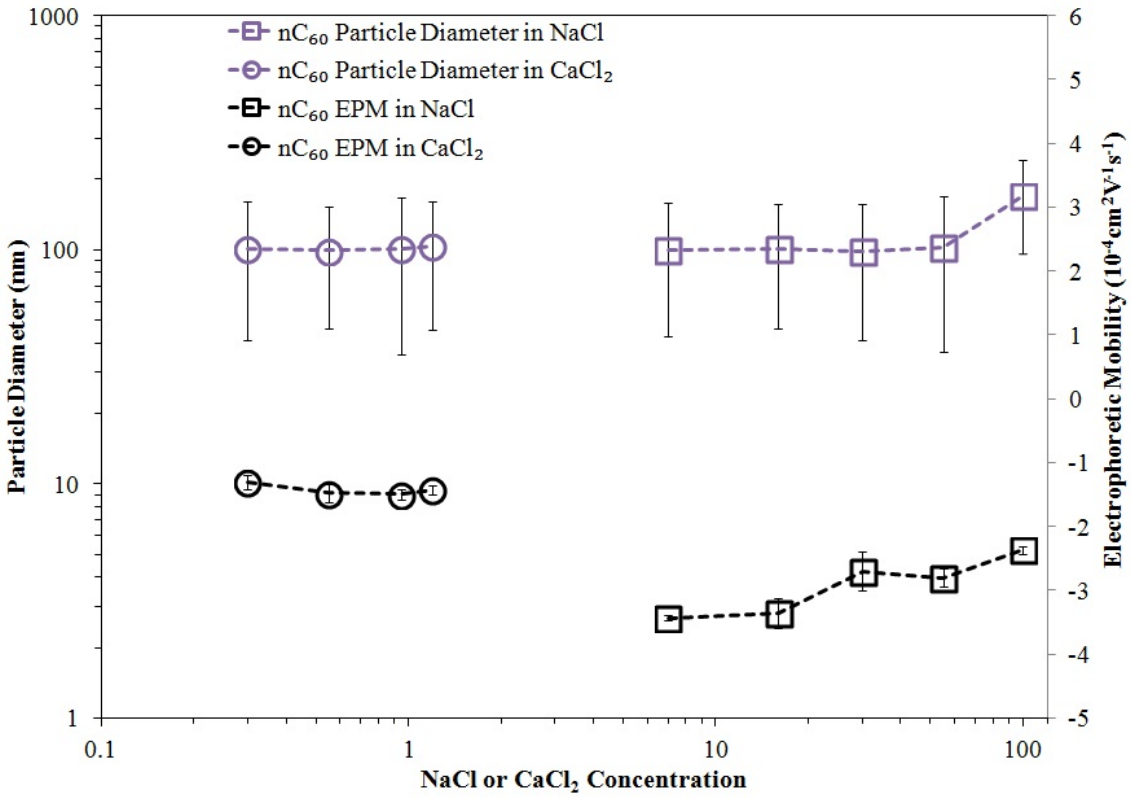

Figure 3.2: The intensity weighted average hydrodynamic particle diameter and electrophoretic mobility of nC_{60} at each NaCl and $CaCl_2$ concentration investigated. Error bars represent standard deviation.

3.2.7 DLVO Interaction Energy Calculations

By assuming a sphere-plate interaction, Eq. 3.4 was used to calculate the van der Waals attraction energy between nC_{60} and the coated or uncoated silica surface [103], where A is the combined Hamaker constant for the nC_{60} water silica system (4.71 x 10^{-21} J) [64], a is the radius of nC_{60} particles at a given electrolyte concentration (Fig. 3.2), h is the separation distance between the nC_{60} particle and silica sensor surface, and λ is the characteristic wavelength of interaction (usually assumed to be 100 nm) [104]. Mean values of particle diameter and zeta potential are used in all DLVO calculations.

$$V_A = -\frac{Aa}{6h}\left(1+\frac{14h}{\lambda}\right)^{-1} \tag{3.4}$$

Eq. 3.5 was used to calculate the electrical double layer repulsion energy between nC_{60} and the coated or uncoated silica surface [103], where ε_0 is the dielectric permittivity in a vacuum (8.85 x 10^{-12} $c^2J^{-1}m^{-1}$), ε_r is the relative dielectric permittivity of water (78.3), ζ_p is the zeta potential of the nC_{60} particles at a given electrolyte concentration (Table 3.1), ζ_c is the zeta potential of the coated or uncoated silica surface at a given electrolyte concentration (Fig. 5), and κ is the inverse Debye length.

$$V_R = \pi\varepsilon_0\varepsilon_r a\left\{2\zeta_p\zeta_c ln\left[\frac{1+exp(-\kappa h)}{1-exp(-\kappa h)}\right]+\left(\zeta_p^2+\zeta_c^2\right)ln\left[1-exp(-2\kappa h)\right]\right\} \tag{3.5}$$

Eq. 3.6 was used to calculate the inverse Debye length for the electrolyte system, where e is the elementary charge, n_j is the number concentration of ions in the bulk solution, z_j is ion valence, k is the Boltzmann constant, and T is the absolute temperature.

$$\kappa = \sqrt{\frac{e^2\sum n_j z_j^2}{\varepsilon_0\varepsilon_r kT}} \tag{3.6}$$

Table 3.1: nC_{60} zeta potential values for use in DLVO calculations, estimated from the electrophoretic mobility values using the Smoluchowski approximation [114].

Electrolyte Concentration	nC_{60} Electrophoretic Mobility ($10^{-4}cm^2V^{-1}s^{-1}$)	Zeta Potential (mV)
7 mM NaCl	-3.43	-44.1
16 mM NaCl	-3.36	-43.1
30 mM NaCl	-2.70	-34.7
55 mM NaCl	-2.80	-36.9
100 mM NaCl	-2.37	-30.5
0.30 mM $CaCl_2$	-1.30	-16.7
0.55 mM $CaCl_2$	-1.55	-19.9
0.95 mM $CaCl_2$	-1.52	-19.5
1.2 mM $CaCl_2$	-1.35	-17.3

3.3 Results and Discussion

3.3.1 nC_{60} aggregation kinetics

Since the size of nC_{60} particles can affect their mass transport rate towards the sensor surface and therefore control their deposition, it is important to first understand their aggregation behavior. Presented in Fig. 3.3 are the aggregation attachment efficiency factors (Eq. 3.1) for a range of NaCl (a) and $CaCl_2$ (b) concentrations. As the ionic strength is increased, the EDL repulsion becomes more suppressed and therefore the energy barrier to aggregation is reduced, allowing the nC_{60} particles to aggregate more rapidly. When the ionic strength becomes high enough, the EDL repulsion is reduced to zero, the energy barrier to aggregation vanishes, and the aggregation rate is limited only by the diffusion of particles towards each other. This concentration is known as the CCC [60]. Above the CCC, α_A values level off at 1, as can be seen in Fig. 3.3. By interpolation of the data in Fig. 3.3 to find the point of intersection between the reaction limited and diffusion limited regimes, the CCC was estimated as 217 mM NaCl (a) and 3.7 mM $CaCl_2$ (b), illustrating a much higher sensitivity to aggregation in the presence of the divalent cation Ca^{2+}. The ratio of CCC values derived here (3.7/217) is proportional to $z^{-5.9}$, where z is the valence of Ca^{2+}. This is in very close agreement with the Schulze-Hardy rule which predicts a value of z^{-6}, [60] and much closer than the previously reported value of $z^{-4.64}$ for nC_{60} [61], though it is worth noting that the properties of nC_{60} have been shown to be somewhat dependent upon preparation method [67].

3.3.2 nC_{60} deposition kinetics

The initial deposition rate of nC_{60} onto the sensor surface was accompanied by a linear change in frequency (Fig. 3.1), suggesting continuous deposition on the clean sensor surface with no ripening or detachment. The Voigt viscoelastic model [95] is typically employed to estimate the mass and thickness of a viscoelastic film [94] such as nC_{60} in

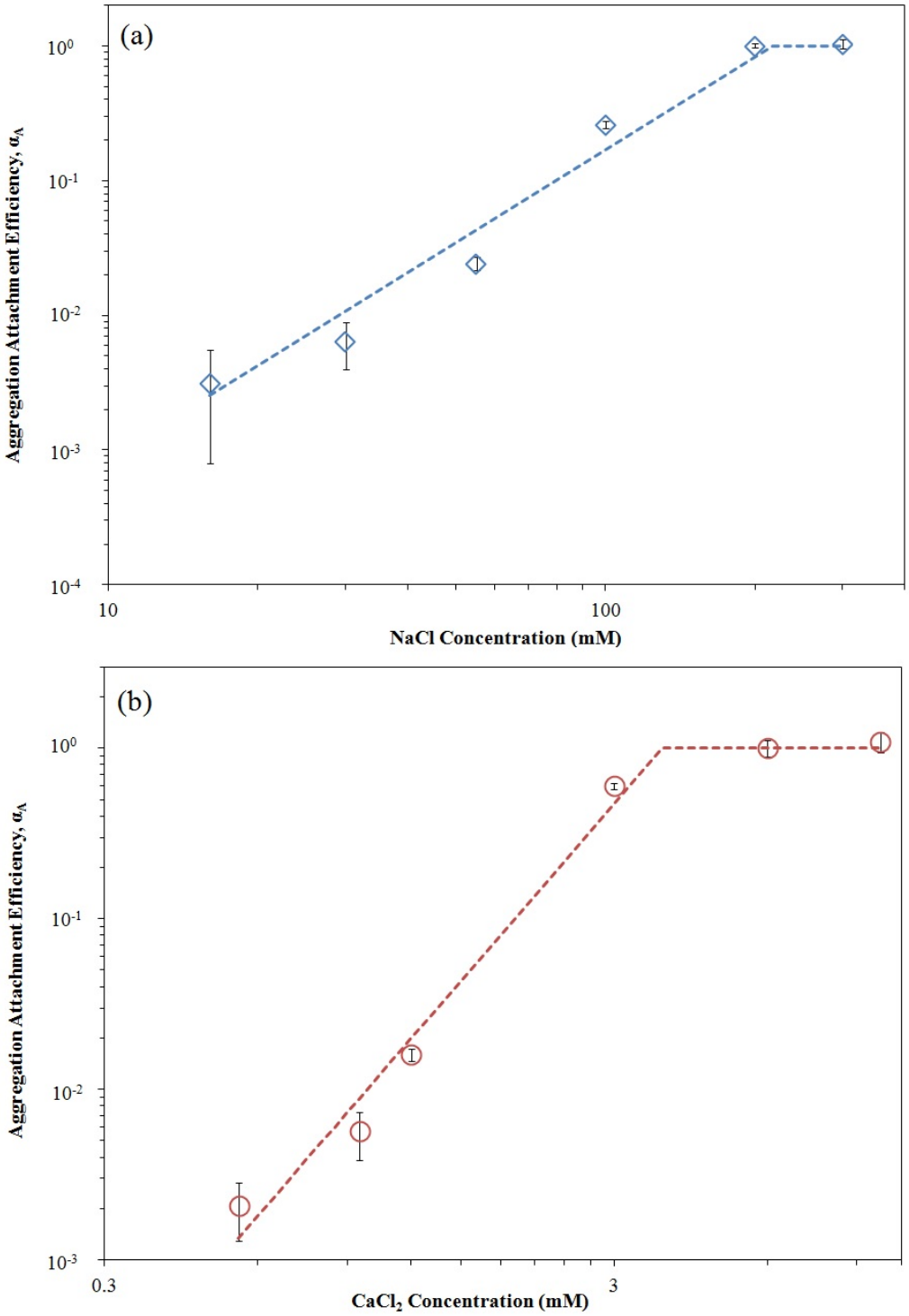

Figure 3.3: nC_{60} aggregation attachment efficiency factors for a range of NaCl (a) and $CaCl_2$ (b) concentrations. Each point consists of three measurements and error bars represent standard deviation.

this study. Because of the limitations of the Voigt model, for example, it assumes a homogenous, uniform layer, the mass calculated includes water, and the density of the layer is assumed and held constant, we chose to quantify deposition rate as the initial slope of the third overtone of frequency.

The nC_{60} deposition rate as a function of NaCl (a) and $CaCl_2$ (b) concentrations onto three different surfaces can be seen in Fig. 3.4. The calculated Peclet number (Pe) for the experiments in this study ranged from $7.94*10^{-8}$ to $4.34*10^{-7}$ (details can be found in B). Pe describes the rate of convective mass transport to diffusive mass transport, therefore such small values suggest diffusive mass transport dominates for all experimental conditions investigated. Since nC_{60} is negatively charged over all experimental conditions investigated (Fig. 3.2)), deposition onto the oppositely charged PLL surface is limited only by diffusion of the particles towards the sensor surface and therefore the deposition onto PLL in Fig. 3.4 represents diffusion limited conditions. As NaCl concentration increases in Fig. 3.4(a), the nC_{60} particle size increases (Fig. 3.3(a)) causing a decrease in diffusive mass transport and a corresponding decrease in deposition for the PLL-coated trend, with the highest decrease occurring as the NaCl concentration in Fig. 3.4(a) approaches the CCC. The PLL-coated trend in the presence of $CaCl_2$ (Fig. 3.4(b)) shows a small decrease throughout, without the sharp decrease observed in Fig. 3.4(a), which can be explained by noticing that the highest $CaCl_2$ concentration in Fig. 3.4(b) is far from reaching the corresponding CCC for $CaCl_2$ in Fig. 3.3(b).

As ionic strength increases, the EDL repulsion between the bare silica surface and nC_{60} is increasingly suppressed, lowering the energy barrier to deposition and therefore increasing the deposition rate for the bare silica trend in Fig. 3.4. As ionic strength increases, it eventually reaches a point where the energy barrier is completely suppressed, the deposition is limited by diffusion alone, and the bare silica and PLL-coated trends coincide, known as the critical deposition concentration (CDC). In this manner, the bare silica trend in Fig. 3.4 represents the summation of the energy barrier reduction and particle aggrega-

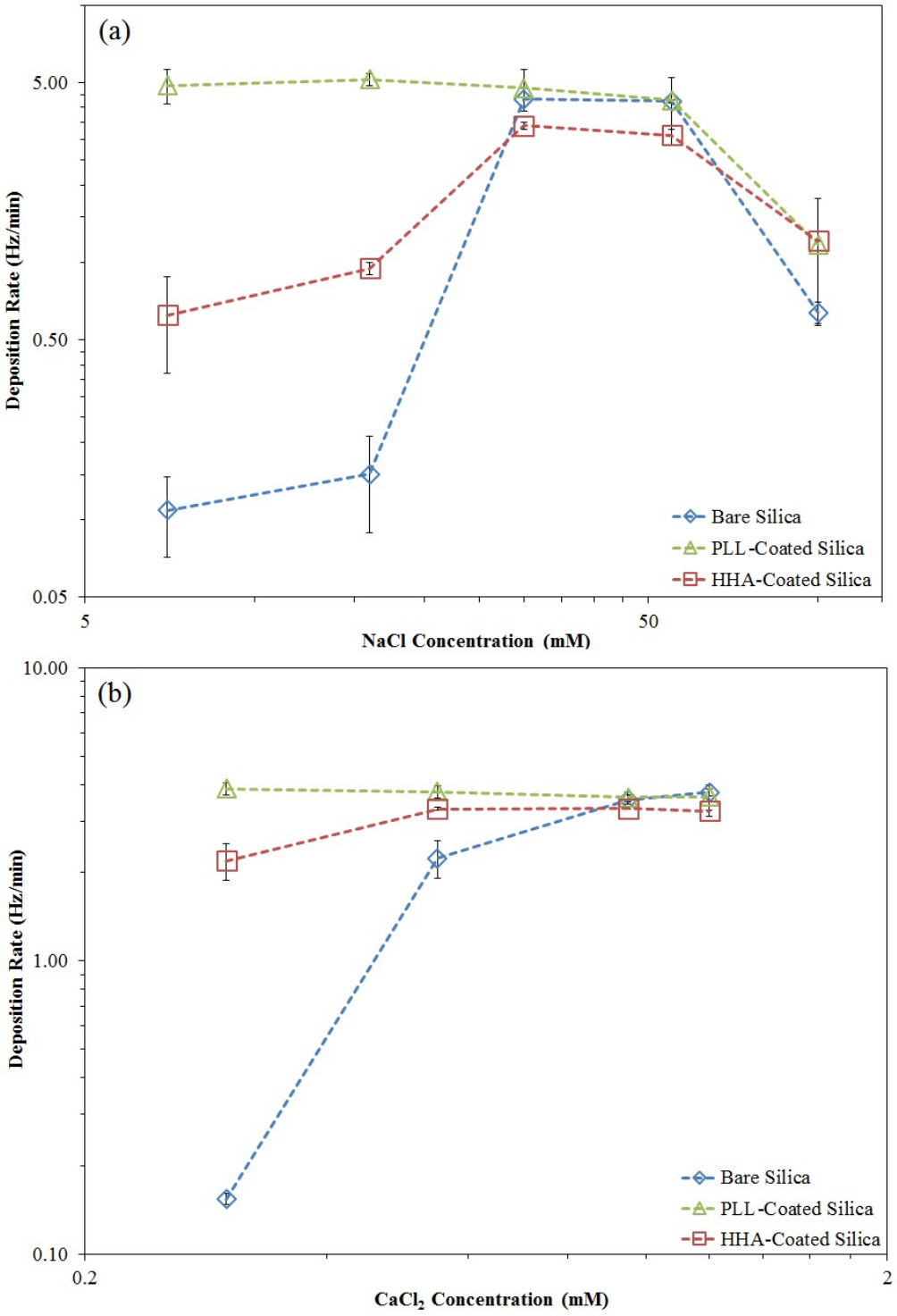

Figure 3.4: nC_{60} deposition rates as a function of NaCl (a) and $CaCl_2$ (b) concentrations onto three different surfaces. Each point consists of three measurements and error bars represent standard deviation.

tion effects. At low NaCl and $CaCl_2$ concentrations, an increase in ionic strength results in a large reduction in the energy barrier, but only a small increase in nC_{60} particle size, so the bare silica deposition trend increases rapidly. Conversely, at high concentrations of NaCl and $CaCl_2$ an increase in ionic strength results in a large increase in nC_{60} particle size but no reduction in the energy barrier, since it is already reduced to zero, so the bare silica deposition trend decreases (Fig. 3.4 (a)) or remains the same (Fig. 3.4 (b)). As explained previously, the lack of a decrease in the bare silica trend in Fig. 3.4 (b) is likely due to the CDC occurring at a $CaCl_2$ concentration far from the CCC. At intermediate concentrations of NaCl and $CaCl_2$, the two effects offset and result in smaller changes to the bare silica deposition trend.

3.3.3 Effect of humic acid layer

In order to elucidate the effect of the HHA coating, the deposition attachment efficiency was calculated at every experimental condition (Eq. 3.3) and presented in Fig. 3.5. For both cations investigated, the HHA coating enhanced nC_{60} attachment at low concentrations and hindered attachment at high concentrations. The HHA coating raised the attachment efficiency an order of magnitude for both of the lowest NaCl concentrations (Fig. 3.5 (a)) and the lowest $CaCl_2$ concentration (Fig. 3.5 (b)). As the concentration increased however, the HHA coating hindered attachment and raised the CDC to near 100 mM NaCl (Fig. 3.5 (a)) or, in the case of $CaCl_2$, failed to reach the CDC within the concentration range investigated (Fig. 3.5 (b)). The presence of the HHA coating caused a hindering of attachment for NaCl concentrations of 30 and 55 mM and $CaCl_2$ concentrations of 0.95 and 1.2 mM. Quite clearly, this behavior deviates from the typical steric stabilization often seen in the presence of DOM [49–52, 66] and further validates the variable nature observed in other deposition studies of NOM coatings [39, 50, 64, 66]. In order to explain the observed behavior of the HHA-coating, the electrophoretic mobility (EPM) of silica with and without coatings of HHA was measured and presented in Fig. 3.6.

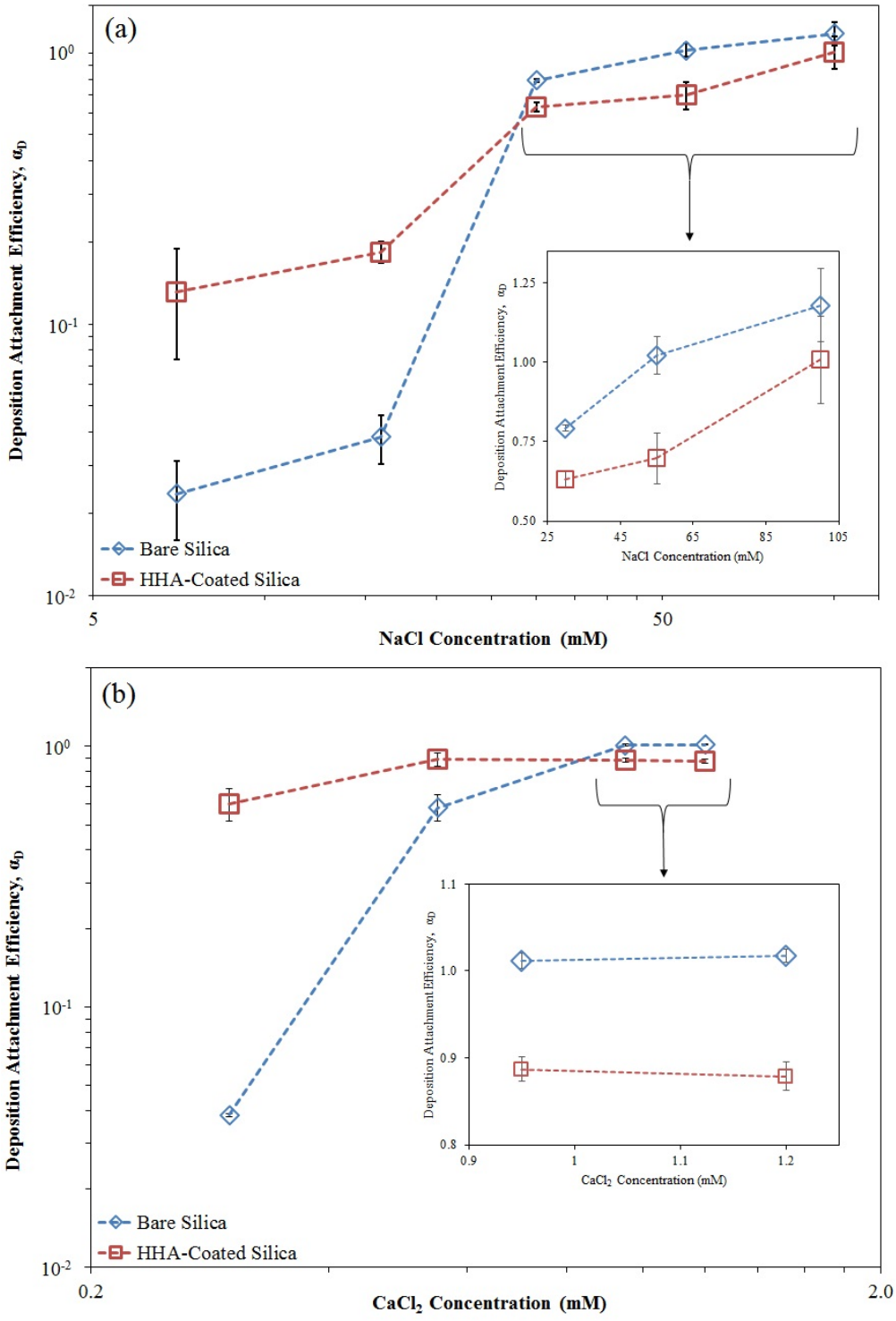

Figure 3.5: nC_{60} deposition attachment efficiency factors as a function of NaCl (a) and $CaCl_2$ (b) concentrations onto bare and HHA-coated silica. Each point consists of three measurements and error bars represent standard deviation. Figure insets provide a more detailed view of experimental values at high electrolyte concentrations, presented on an arithmetic scale.

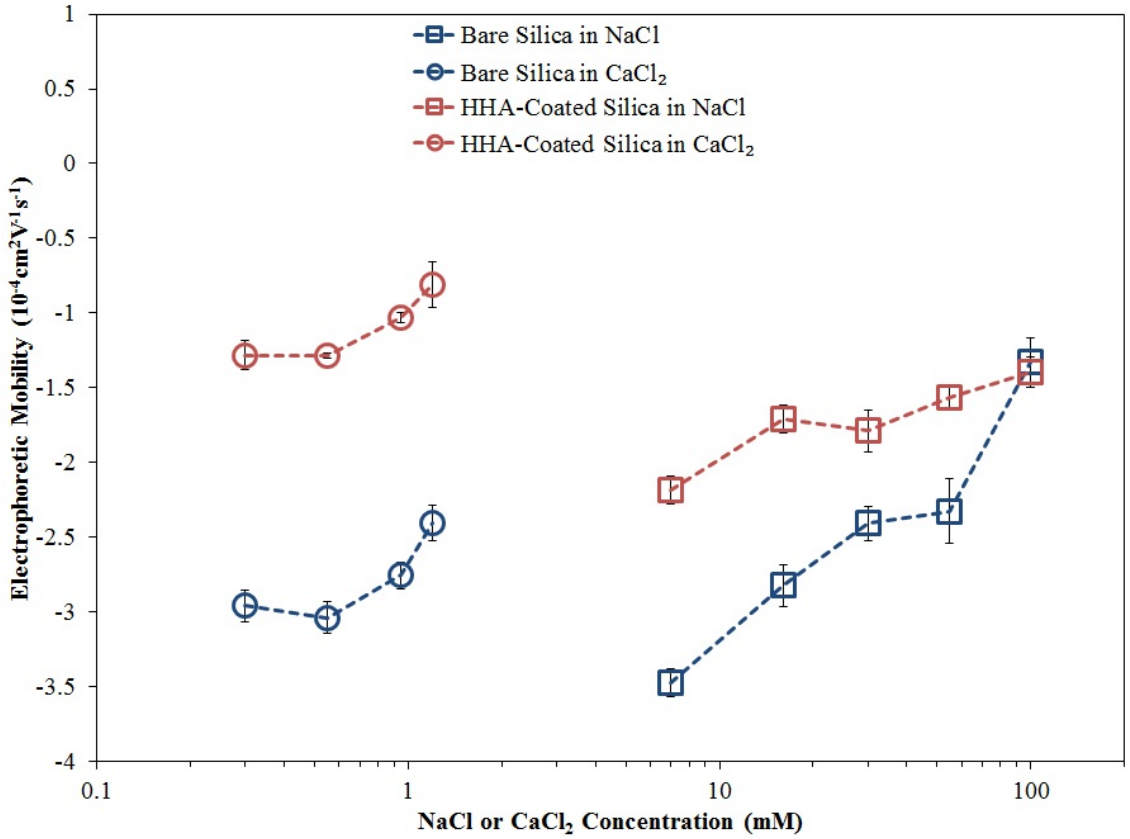

Figure 3.6: Electrophoretic mobility measurements of 900 nm silica microspheres with and without coatings of HHA, as a function of NaCl and $CaCl_2$ concentration. Each value was the result of 10 independent measurements and error bars represent standard deviation.

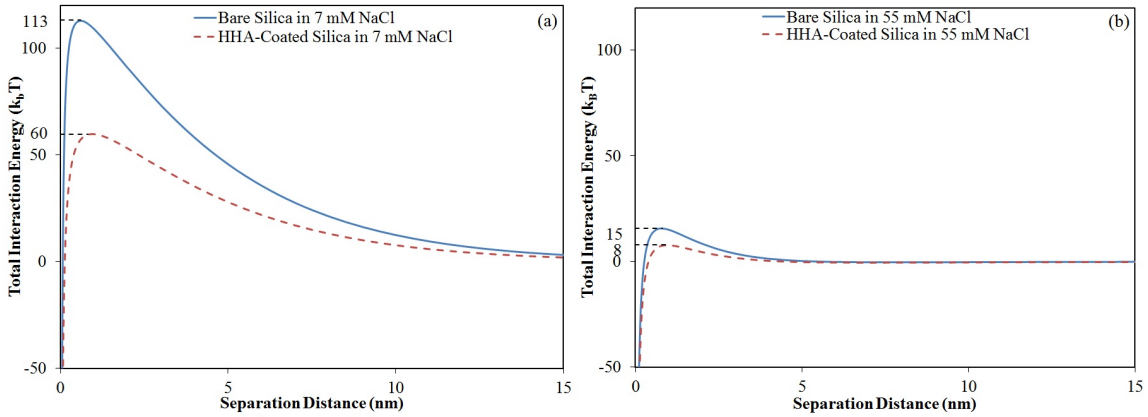

Figure 3.7: DLVO interaction energy profile of nC_{60} approaching a silica surface with and without a HHA coating in the presence of 7 (a) and 55 (b) mM NaCl.

The bare silica remains negatively charged throughout the concentration range investigated (Fig. 3.6), as expected from reported zeta potential values of SiO_2 thin films [115] and silica sands [64]. Interestingly, however, the HHA coating reduced the surface charge (closer to neutral) of the silica throughout all concentrations investigated, except for the case of 100 mM NaCl, at which point the two values were statistically identical. A less negatively charged (closer to neutral) surface would certainly provide less resistance to nC_{60} deposition through a reduction in electrostatic repulsion, which is evident by the enhanced nC_{60} attachment at low NaCl and $CaCl_2$ concentrations (Fig. 3.5). If this were the only contributing effect, however, enhanced attachment would continue throughout the entire range of concentrations investigated, instead of hindering nC_{60} attachment at higher concentrations, as observed in Fig. 3.5. In order to further understand the complex interactions taking place in this system, a DLVO interaction energy profile was calculated for a 100 nm nC_{60} particle approaching a silica surface with and without a coating of HHA, with properties matching the nC_{60} (Fig. 3.2 and Table 3.1), silica (Fig. 3.6), and HHA coating (Fig. 3.6) measured in this study.

In the presence of 7 mM NaCl, the DLVO interaction energy curve predicts a much lower energy barrier to nC_{60} deposition when the silica surface is coated with HHA (Fig. 3.7 (a)) as observed in Fig. 3.5 (a). At a concentration of 55 mM NaCl (Fig. 3.7 (b))

DLVO predicts a much larger EDL screening effect and therefore the energy barrier to nC_{60} deposition is much lower for both cases, bare silica and HHA-coated silica. In the presence of 55 mM NaCl, the energy barrier to nC_{60} deposition is still slightly smaller onto the HHA-coated silica, due to a reduction in surface charge. The significance of this difference, however, is much lower since the energy barrier has nearly disappeared at the increased NaCl concentration. Since DLVO does not correctly predict the attachment hindering behavior of the HHA coating at increased NaCl and $CaCl_2$ concentrations, a non-DLVO force is likely contributing.

The structure of immobilized macromolecules has been shown to depend on ionic strength [116, 117] and, in particular, NOM layers have been shown to condense with increased ionic strength [66, 118]. At increased NaCl and $CaCl_2$ concentrations, the HHA layer compacts and has a more condensed, less extended (smoother) surface with reduced potential for nC_{60} particle entanglement, effectively lowering attachment efficiency (Fig. 3.5). Furthermore, the compaction of the HHA layer may reduce the amount of available hydrophobic regions for nC_{60} attachment, contributing to the reduction in attachment efficiency. This finding is in agreement with two studies which have reported a reduction in nC_{60} attachment due to the compaction of alginate [66] and humic acid [39] layers.

3.4 Conclusions

In this study, we have shown that the presence of a HHA coating can both hinder and enhance nC_{60} attachment onto a silica surface, depending on solution chemistry. At low electrolyte concentrations, the HHA coating enhances nC_{60} attachment for both mono and divalent cations. By lowering the surface potential of the silica surface, the HHA coating significantly reduces the energy barrier to nC_{60} deposition. As electrolyte concentration rises, the HHA coating eventually results in a hindering of attachment for both mono and divalent cations. Though still lowering the surface potential of silica, the HHA coating doesn't significantly lower the energy barrier to deposition at these elevated electrolyte concentrations, due to the significant suppression of EDL repulsion resulting in a near zero energy barrier to nC_{60} deposition. Furthermore, the structure of the HHA coating likely condenses at elevated electrolyte concentration, leading to a more compact and smoother surface with less potential for nC_{60} particle entanglement, contributing to the observed reduction in attachment efficiency. Because of the aforementioned reasons, we hypothesize that the summation of two contributing forces are responsible for the observed trend in nC_{60} attachment onto HHA-coated silica: (1) the reduction in electrostatic repulsion due to the HHA-coating and (2) HHA layer compaction at increased NaCl and $CaCl_2$ concentrations.

Based on the findings presented in this study and our recent work [39], attached SOM layers play a complex role in the deposition behavior of nC_{60}. If similar contributions exist for other types of ENMs, SOM will play a major role in determining the environmental fate and transport of ENMs. Fully understanding the contributions from SOM may prove crucial to predicting potential pathways of exposure and their impact on ecosystems and human health.

Chapter 4

The attachment of colloidal particles to environmentally relevant surfaces and the effect of particle shape

4.1 Introduction

Colloidal transport through the subsurface environment is a topic of great importance and intense study to the field of environmental engineering. Seemingly immobile toxins can attach to the surface of mobile colloids and be readily transported through the subsurface, greatly enhancing their risk to ecosystems and human health, or in some cases, the colloid itself is the toxin of concern [119]. Many natural colloids are nonspherical in shape, including plate and rod shaped clay [68], various bacterial shapes (e.g. ellipsoid, ovoid, and rod shaped) [69, 70], and some engineered nanomaterials (e.g. carbon nanotubes) which exhibit an aquatic toxic potential [3]. Despite the ubiquity of nonspherical colloids, only a limited number of studies have focused on the role of shape with regard to colloidal transport [71, 72, 74, 75, 120].

Aside from advection, dispersion, and diffusion, colloidal transport also depends on the kinetic rate at which particles attach to soil and grain surfaces with which they collide. Since most of the aforementioned studies exclusively employ column experiments, the mechanisms behind the particle-surface attachment cannot be isolated. To date, only one study has attempted to isolate the role of shape on particle deposition. Seymour et al. [71] reported a much higher deposition rate of spherical carboxylate-modified polystyrene particles as compared to 2:1 and 4:1 stretched versions of the same particles. These experiments, however, were conducted under favorable conditions (i.e. a positively charged, PLL-coated silica surface), lacking an energy barrier to deposition and limiting the environmental relevance of the findings. No study to date has investigated the role of shape on colloidal particle attachment to environmentally relevant surfaces.

Derjaguin-Landau-Verwey-Overbeek (DLVO) theory [58, 59] describes the attractive and repulsive forces between a colloidal particle and a surface. Several studies have investigated the attachment of colloidal particles to bare mineral surfaces in simple electrolyte solutions [61, 63, 65, 66, 104, 121, 122] and the results appear to be in good qualitative agreement with DLVO theory. The attachment deviates significantly from DLVO theory, however, in the presence of natural organic matter (NOM), whether dissolved in solution [64, 66, 104, 123, 124] or coated onto the depositional surface [39, 63, 64, 66, 80, 104, 124, 125]. When dissolved in solution, NOM adsorbs to the surface of colloidal particles and typically limits their deposition through steric hindrance, a force not considered by DLVO theory. When the depositional surfaces are pre-coated with NOM, however, the results tend to be much more complex. Pre-coating silica surfaces with various NOM have been shown to hinder, enhance, or have no effect on attachment, depending on the type of NOM [39, 66], ionic strength of solution [63, 64, 66], and temperature [39]. Chen and Elimelech [66] reported that an alginate layer enhanced nC_{60} attachment in the presence of 10 mM NaCl, while hindering it in the presence of 30 mM NaCl. The variable nature was attributed to the alginate layer's compaction at higher NaCl concentrations, resulting in a smoother, more rigid layer, with less room for nC_{60} particle entanglement. In our recent work [39], we reported that increasing the temperature of a humic acid layer while holding all other variables constant, raised the attachment efficiency of nC_{60} from low attachment ($\alpha = 0.3$) to complete attachment ($\alpha = 1$). We attributed this to the temperature-dependent hydration of the layer, opening up previously unavailable sorption sites. Quite clearly, more research is needed into the effect of NOM coatings on colloidal particle attachment.

The purpose of this study is to isolate the role of shape on the attachment of colloidal particles to environmentally relevant surfaces by combining quartz crystal microbalance with dissipation monitoring (QCM-D), atomic force microscopy (AFM), and dynamic light scattering (DLS) experiments. For the first time, we present attachment efficiency curves for colloidal particles onto NOM coated silica surfaces, as a function of particle shape and

ionic strength. By comparing the attachment results with DLS surface measurements and AFM topography images, we elucidate and discuss the mechanisms driving the complex attachment behavior observed. The results presented here suggest that colloidal particle shape will play an important role in predicting transport, especially in the presence of NOM. A better understanding of the role of shape in the attachment of colloidal particles to environmentally relevant surfaces will lead to a more accurate prediction of colloidal particle transport, aiding in risk assessment of potential exposure pathways.

4.2 Materials and Methods

4.2.1 Materials

200 nm carboxylate-modified polystyrene (PS) spheres were purchased from Phosphorex (107, Hopkinton, MA). Dry Harpeth humic acid (HHA) was isolated and characterized as described in our previous publication [101]. Alginic acid sodium salt (alginate, A2158), poly-L-lysine hydrobromide (PLL, P1274), and 4-(2-Hydroxyethyl)-1-piperazineethanesulfonic acid (HEPES) were purchased from Sigma-Aldrich (St. Louis, MO). Reagent grade NaCl (S671) was purchased from Fisher Scientific (Pittsburgh, PA). Silica-coated QCM-D sensors (QSX-303) were purchased from Q-Sense (Biolin Scientific, Stockholm, Sweden). 900 nm silica microspheres were purchased from Polysciences Inc (Warrington, PA) as a surrogate for estimating the electrophoretic mobility of the silica sensor surface. All solutions were prepared using ultra pure water purified by the Milli-Q Water Purification System from Millipore (Billerica, MA).

4.2.2 Preparation of stretched PS particles

The method described here is based on a procedure previously published by Champion et al. [126]. First, 10% (wt/vol) polyvinyl alcohol (PVA, Sigma-Aldrich) solution was introduced into 80 °C Milli-Q water, and stirred for 30 minutes to achieve complete dissolution of PVA. 100 mg glycerol (Sigma-Aldrich) and 2.5 mL of 1% solid content (0.0625% (wt/vol) particle/water) PS spheres were added to the PVA solution. The solution mixture was then poured onto a 12 x 12 cm clean film plate and was set to dry for 24 hours to form a thin film. The film was then cut into four pieces and subsequently placed in a stretching apparatus (Fig. 4.1). The stretching apparatus was submerged in a 125 °C mineral oil bath for 5 minutes and stretched to a 2:1 ratio. This temperature is close to the glass transition temperature of polystyrene particles, which allows the particles to stretch to the desired ratio. The stretched film was then cooled to room temperature and cut from the apparatus.

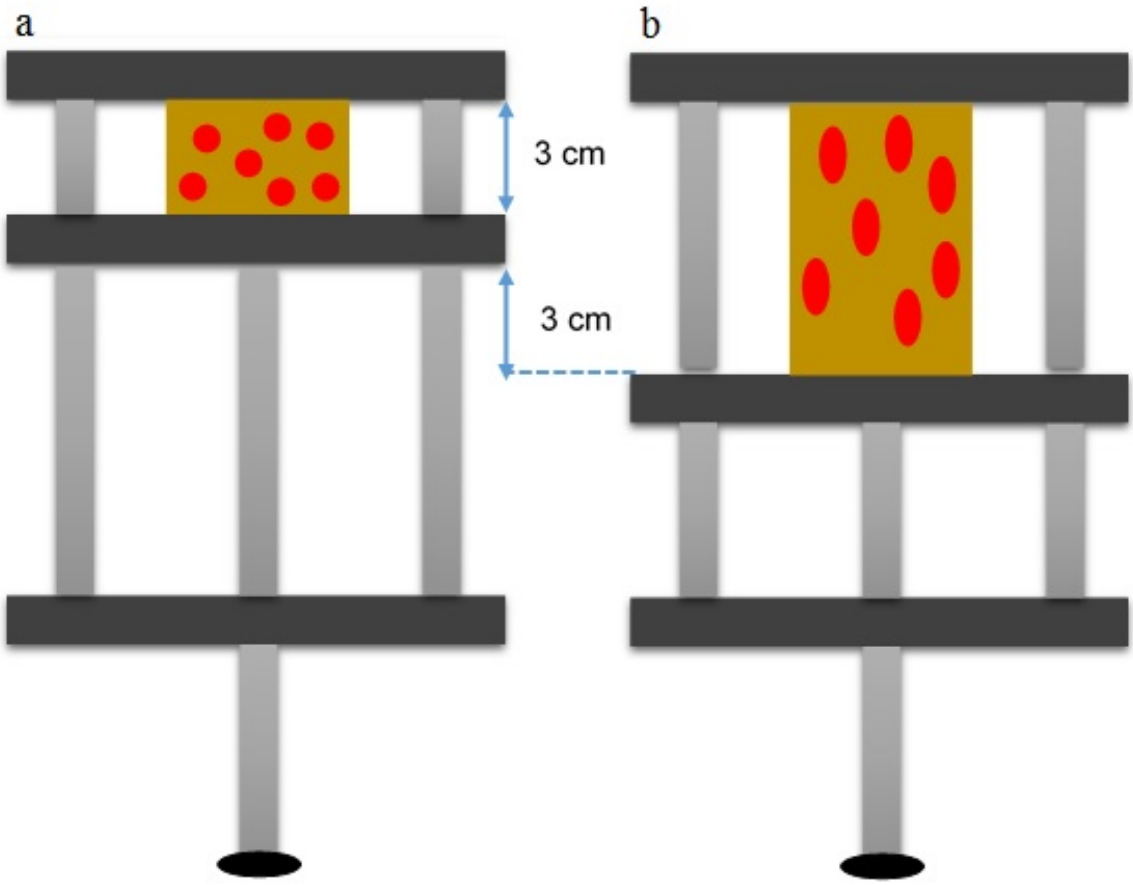

Figure 4.1: Diagram of the particle stretching apparatus before (a) and after (b) stretching.

After being cleaned by 100% isopropyl alcohol (IPA) for at least two hours, the film was dissolved in 70 °C water for several hours. Finally, the stretched PS particles were cleaned with IPA and extracted using a series of centrifugation (Eppendorf Centrifuge 5840R).

In order to determine the concentration of the stretched particles, a calibration curve was constructed using known concentrations of stock PS particles and UV-vis spectrophotomemtry (NanoDrop 2000 Thermo Scientific, Wilmington, DE). The stock stretched PS suspension was determined to have a concentration of 129 mg L^{-1}.

4.2.3 Preparation of HHA solution

In order to prepare the HHA solution, 50 mg dry HHA was introduced into 400 mL deionized water and stirred for more than 3 hours. During this time, the pH was adjusted drop wise with 0.1 N NaOH to a pH of 10.0 to allow the HHA to dissolve. After nearly complete dissolution of the HHA, the pH was adjusted drop wise with HCl down to 7.0. The alginate stock solution was prepared by stirring 50 mg dry alginate in 400 mL deionized water overnight, after which time the alginate was adjusted drop wise with 0.1 N NaOH to a pH of 7.0. Both HHA and alginate stock solutions were filtered through 0.22 μm pore size membrane filter paper (Fisher, GSWP02500) and kept in the dark for the entirety of the study, during which time they remained stable to aggregation as confirmed by periodic DLS measurements. The resulting HHA and alginate stock solutions were determined to have a total carbon content (Shimadzu TOC-V CPH/CPN, Columbia, MD) of 110 and 102 mg L^{-1}, respectively.

All prepared electrolyte solutions were filtered through a 0.22 μm pore size membrane filter paper and pH adjusted so that all attachment experiments could take place at a pH of 7.0.

4.2.4 Characterization measurements

Because particle size can control diffusion rate, DLS (Malvern Zetasizer Nano ZS, Worcestershire, UK) was utilized to measure the size of spherical PS particles at each experimental condition investigated. Five independent runs at 1 minute each were performed for each particle size measurement, with each resulting data point consisting of 5 independent measurements.

Image J software was used to measure the length of major and secondary axes of the stretched PS particles. Figs. A.3, A.4, and A.5 show the distribution of major and minor axis of the stretched PS particles and their ratio based on the Image J measurement of

100 particles. Additional shape related parameters including averaged ellipticity, effective diameter, and surface area are provided in Tab. 4.1. The method for calculating these values is summarized in A.3.

Electrophoretic mobility (EPM) measurements were conducted for the spherical and stretched PS particles at each experimental condition by DLS in conjunction with a universal dip cell (Malvern ZEN1002, Worcestershire, UK). Each reported value of EPM was the result of 10 independent measurements. In order to estimate the EPM values of the silica depositional surfaces utilized in this study, 900 nm silica microspheres were used as a surrogate. EPM values were measured for uncoated, HHA-coated, and alginate-coated silica at each experimental condition. In order to coat the silica microspheres, they were first introduced into a 100 mg L^{-1} solution of PLL, stirred for 20 minutes and then drained through 0.45 μm pore size membrane filter paper (Fisher, GSWP02500) while being rinsed with DI water, allowing all unbound PLL to pass through, but leaving the positively charged, PLL-coated silica particles behind. The process was then repeated for a HHA or alginate coating. All EPM measurements were conducted at a silica concentration of 10 mg L^{-1}. Since the particle radius was much larger than the Debye length at each experimental condition investigated in this work, zeta potentials were estimated using the Smoluchowski approximation [114].

4.2.5 Attachment experiments

The deposition rate of spherical or stretched PS was monitored using a QCM-D (Q-Sense E4 unit, Biolin Scientific, Stockholm, Sweden) under varying experimental conditions. Flowrates were held constant at 0.1 mL min^{-1}, resulting in laminar flow within the module as confirmed by a Reynolds Number of 0.26. PS particle concentration and pH was held constant at 6 mg L^{-1} and 7, respectively, in order simulate environmentally relevant conditions. All experiments took place at a temperature of 20 °C, which was held constant by a Peltier element. The QCM-D sensor cleaning protocol is as follows. Before

each experiment, the silica QCM-D sensors were soaked in a 2% Hellmanex II solution (Hellma Analytics, Mullheim, Germany) overnight, rinsed in DI water, and dried in ultra-pure N_2. The sensors were then cleaned in a UV-Ozone cleaner (Jelight 42, Irvine, CA) for 20 minutes immediately before being loaded into the QCM-D.

A representative QCM-D experiment can be seen in Fig. 4.2, with a detailed experimental protocol as follows. A baseline was first collected in a HEPES solution (10 mM HEPES, 100 mM NaCL). The signal was considered stable when the third overtone of frequency (f_3) failed to drift more than 0.3 Hz over the course of 10 minutes. Then, a layer of positively charged PLL was constructed on the silica surface by flowing a solution of 0.1 g L^{-1} PLL, 10 mM HEPES, and 100 mM NaCl until the signal stabilized. The PLL layer was then washed in the HEPES solution to remove any unbound PLL from the surface. A 1 mM NaCl solution was then introduced until a stable signal was reached, followed by a 0.1 g L^{-1} HHA or alginate solution containing 1 mM NaCl. The negatively charged HHA or alginate readily adsorbed to the oppositely charge PLL surface, forming a second layer. Once the signal stabilized, the HHA or alginate layer was washed in 1 mM NaCl to remove any unbound particles and then a solution of the ionic strength of interest was introduced. Once the signal stabilized, the stock suspension of spherical or stretched PS was diluted to 6 mg L^{-1} with a measured amount of concentrated NaCl solution to form the same ionic strength and then immediately introduced into the measurement chamber. As the PS suspension flowed across the sensor surface, the first 120 seconds of the drop in frequency were used to calculate the initial deposition rates for each set of experimental conditions.

As particles attach to the sensor surface, mass increases, corresponding to a continuous decrease in frequency, as described in the Sauerbrey relation [93]. The Sauerbrey relation can be seen in Eq. 4.1, where m is the mass deposited, C is the crystal constant (17.7 ng cm^{-2} Hz^{-1}) and f_n is the frequency at overtone n.

$$\Delta m = -C\frac{1}{n}\Delta f_n \tag{4.1}$$

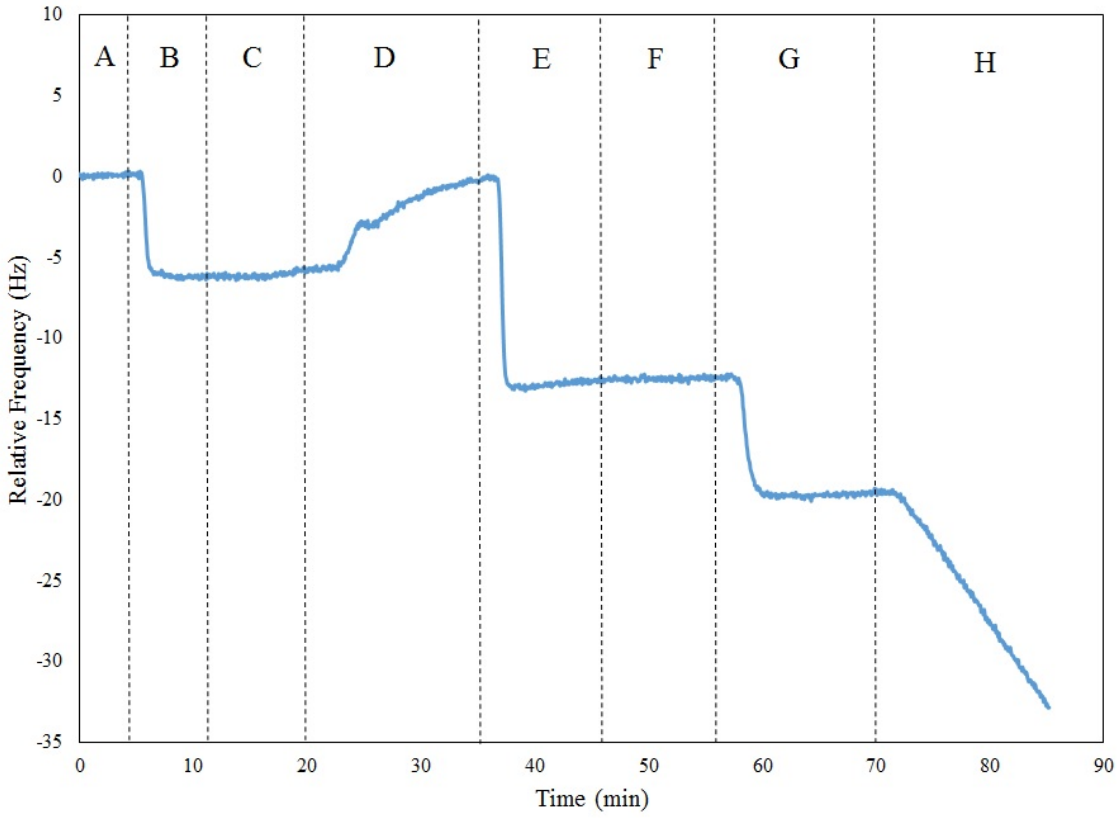

Figure 4.2: Representative attachment experiment. A baseline is collected in HEPES (A) before PLL is adsorbed to the surface (B), followed by a rinse in HEPES (C). 1 mM NaCl is introduced (D) before HHA or alginate is adsorbed to the surface (E) and rinsed with 1 mM NaCl (F). Finally, the ionic strength of interest is introduced (G) and once a baseline is reached, stretched or spherical PS particles are introduced in a solution of the same ionic strength (H).

In order to compare the particle attachment between varying ionic strengths independent of aggregation and diffusion effects, the deposition attachment efficiency (α) was calculated from Eq. 4.2, where $^{df_3}/_{dt}$ is the initial deposition rate of the third overtone of frequency calculated from the first 120 seconds of frequency drop and $(^{df_3}/_{dt})_{diff\ limited}$ is the diffusion limited deposition rate, under identical experimental conditions. The diffusion limited deposition rate was measured by flowing the PS particles over the PLL layer at each experimental condition investigated. Since the PS particles are negatively charged and the PLL layer is positively charged, there is no energy barrier to deposition and any PS particles that flow near the PLL surface will attach, therefore the deposition is limited only

by diffusion of the PS particles to the sensor surface.

$$\alpha = \frac{df_3/dt}{\left(df_3/dt\right)_{diff\ limited}} \tag{4.2}$$

4.2.6 AFM images

A Bruker Dimension Icon AFM (Billerica, MA) was used to image the HHA and alginate surfaces. The HHA or alginate layer was constructed as described in the experimental procedure, carefully removed from the QCM-D, dried in N_2, and loaded into the AFM for imaging. The AFM was operated in tapping mode, using a silicon cantilever. The nominal tip characteristics were 8 nm radius of curvature, 40 N/m spring constant, and 300 kHz resonant frequency.

4.2.7 DLVO interaction energy calculations

Eq. 4.3 [103] was used to calculate the van der Waals attraction between spherical or stretched PS and HHA or alginate surface. A is the combined Hamaker constant (4.71 x 10^{-21} J), a is the particle radius (for stretched particles, the average of the major and minor axis was used), h is the separation distance, and λ is the characteristic wavelength of interaction (usually taken to be 100 nm). Mean values of particle diameter and zeta potential were used in all DLVO calculations.

$$V_A = -\frac{Aa}{6h}\left(1+\frac{14h}{\lambda}\right)^{-1} \tag{4.3}$$

Eq. 4.4 [103] was used to calculate the electrical double layer repulsion between spherical or stretched PS and HHA or alginate surface. ε_0 is the dielectric permitivity in a vacuum (8.85 x 10^{-12} $c^2J^{-1}m^{-1}$), ε_r is the relative dielectric permittivity of water (80.1), ζ_p is the zeta potential of the PS particles at a given electrolyte concentration, ζ_c is the zeta potential of the HHA or alginate surface at a given electrolyte concentration, and κ is the inverse

Debye length. Since the particle radius was much larger than the Debye length at each experimental condition investigated in this work, zeta potentials were estimated using the Smoluchowski approximation [114].

$$V_R = \pi\varepsilon_0\varepsilon_r a\left\{2\zeta_p\zeta_c ln\left[\frac{1+exp(-\kappa h)}{1-exp(-\kappa h)}\right]+\left(\zeta_p^2+\zeta_c^2\right)ln\left[1-exp(-2\kappa h)\right]\right\} \tag{4.4}$$

Eq. 4.5 was used to calculate the inverse Debye length. e is the elementary charge, n_j is the number concentration of ions in the bulk solution, z_j is ion valence, k is the Boltzmann constant, and T is the absolute temperature.

$$\kappa = \sqrt{\frac{e^2\sum n_j z_j^2}{\varepsilon_0\varepsilon_r kT}} \tag{4.5}$$

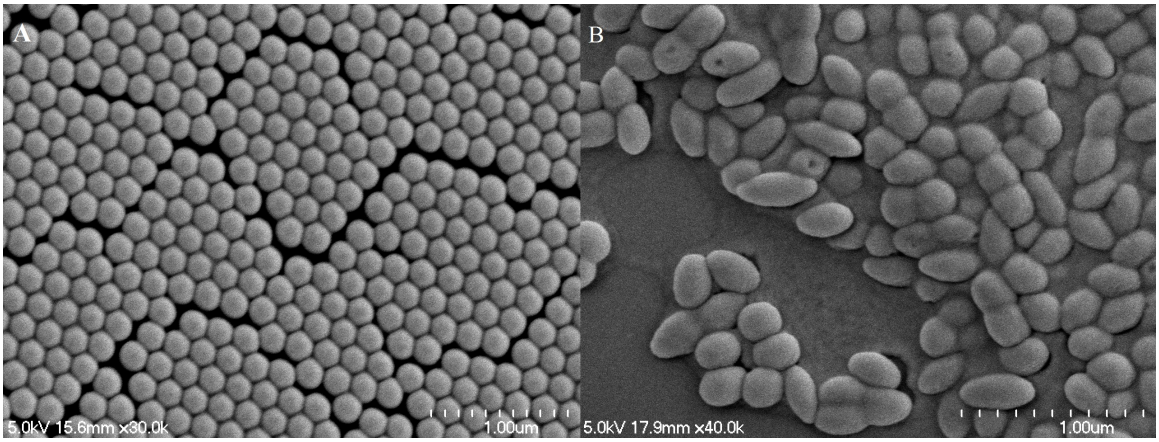

Figure 4.3: Representative SEM images of spherical (A) and stretched (B) PS particles.

Table 4.1: Detailed characteristics of spherical and stretched PS particles.

Particle Characteristic	Spherical (Unstretched) PS Particles	Sretched (2:1) PS Particles
Major axis diameter (nm)	208±3	278±13
Minor axis diameter (nm)	190±3	175±5
Ellipticity	0.37±0.04	0.72±0.03
Surface area (μm^2)	0.120±0.003	0.138±0.008

4.3 Results and Discussion

4.3.1 Particle and surface characterization

Spherical and stretched PS particles were investigated by SEM (Hitachi S4700) and representative images can be seen in Fig. 4.3a and 4.3b, respectively. SEM images of the stretched PS particles were used to quantify the shape of the particles using Image J software. Major axis diameter, minor axis diameter, ratio of axis diameters, ellipticity, surface area, and effective diameter were all estimated for both the spherical and stretched PS particles. A summary of the shape quantification can be seen in Tab. 4.1, with details provided in A.3. After stretching, the major to minor axis ratio was raised from 1:1 to 1.6:1 and the ellipticity was nearly doubled.

The diameter of spherical PS and EPM of spherical and stretched PS were measured as

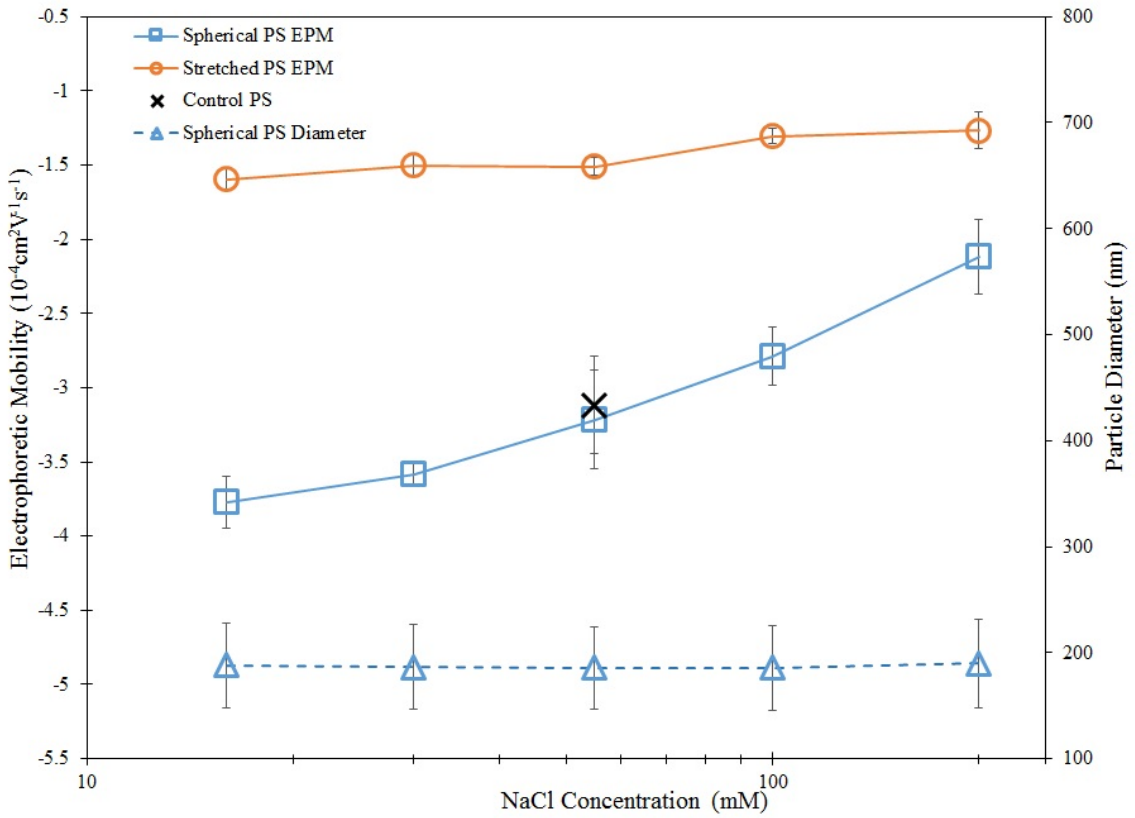

Figure 4.4: EPM measurements of spherical and stretched PS and particle diameter of spherical PS. The control value refers to spherical PS which were exposed to an identical experimental routine as the stretched PS, without being stretched. Each value was the result of 10 independent measurements and error bars represent standard deviation.

a function of ionic strength and can be seen in Fig. 4.4. The spherical PS particle diameter was as expected, based on the nominal 200 nm particle size reported by the manufacturer. The spherical PS diameter remained constant over the ionic strength range investigated, suggesting there was no significant aggregation of the particles.

Both spherical and stretched PS were negatively charged, with the stretched PS carrying a smaller charge (closer to neutral) throughout the entire ionic strength range investigated. Several previous studies have reported a change in EPM between spherical and stretched particles [71, 74, 127–129]. One such study [71], using identical particles to those used here, reported that the EPM of PS particles decreased (closer to neutral) as aspect ratio increased, therefore the sensitivity of EPM to aspect ratio reported here is consistent with

previous studies. The sensitivity of EPM to aspect ratio could be a result of altered charge density due to a change in surface area, or an altered surface due to residual chemicals from the particle stretching process. In order to evaluate which of these possible contributors had a larger effect, a control group of spherical particles was taken through an identical stretching procedure without being stretched, exposing the control group to all the same chemicals. As can be seen in Fig. 4.4, the EPM of the control particles remained statistically identical to that of the spherical PS particles, similar to the reported control in the aforementioned study [71]. This suggests that an altered charge density of the stretched particles is the main contributor to the EPM sensitivity to aspect ratio observed here and elsewhere. The same control group was also used in attachment experiments, to further validate this finding.

The EPM of each depositional surface was also measured and reported in Fig. 4.5. Each surface was negatively charged throughout the ionic strength range investigated and the EPM of the HHA and alginate surfaces were statistically identical at each ionic strength. These findings are in agreement with previous reports for silica surfaces coated with similar NOM [39, 64]. We observed a positive charge for PLL-coated silica, validating it's use to obtain the deposition rate of negatively charged spherical and stretched PS under diffusion-limited conditions (Eq. 4.2).

4.3.2 Attachment experiments

For the first time, we report the attachment efficiency of spherical and stretched PS particles onto HHA and alginate coated silica surfaces as a function of ionic strength in Fig. 4.6. In the presence of the HHA coated silica surface, we observed a higher attachment of spherical than stretched PS at low ionic strengths. At a NaCl concentration of 100 mM, we observed similar attachment values for spherical and stretched PS and above 100 mM NaCl, we observed a higher attachment of stretched than spherical PS. The attachment of the control particles, which were exposed to all the same chemicals as the stretched

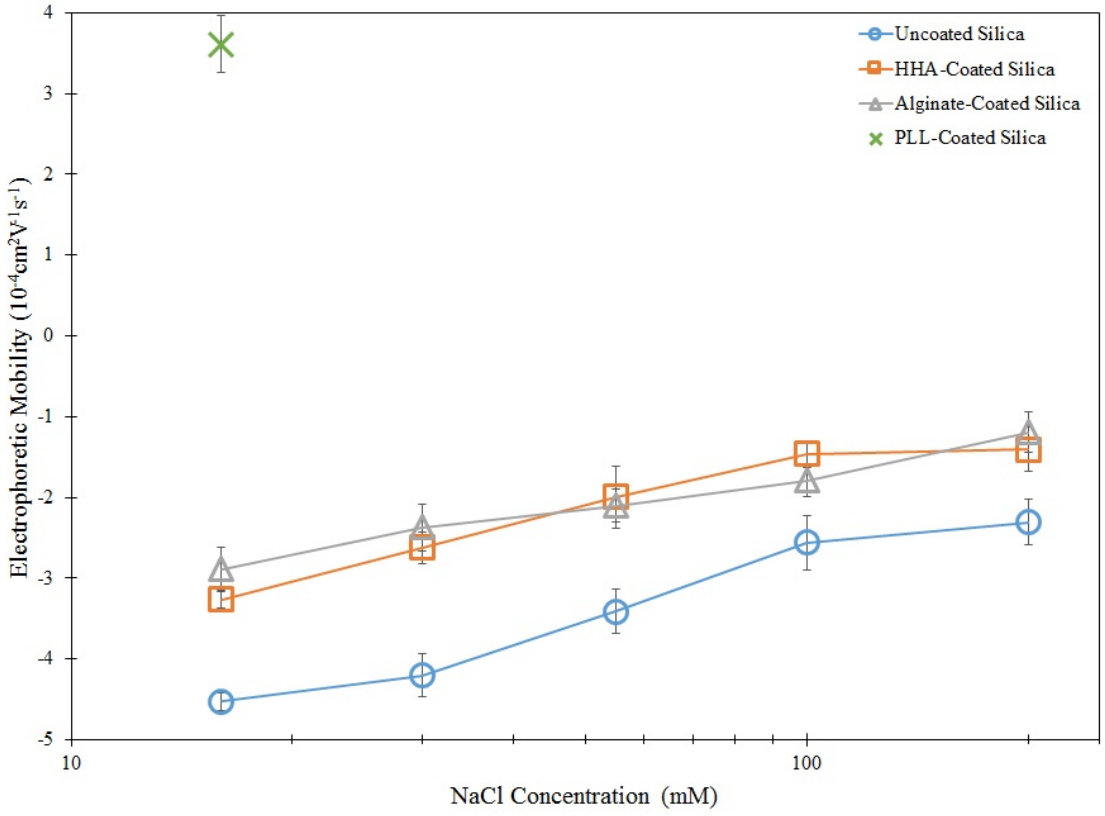

Figure 4.5: EPM measurements of each depositional surface as a function of ionic strength. Each value was the result of 10 independent measurements and error bars represent standard deviation.

particles without being stretched, didn't deviate from the attachment of the spherical PS. This confirms that the observed differences in attachment between spherical and stretched particles are due to the differences in particle shape, rather than a surface alteration as a result of exposure to the chemicals required in the stretching procedure. This finding is in agreement with a previous study [71] which reported similar deposition rates between spherical PS and control particles, despite observing differences for stretched PS. Attachment of spherical and stretched PS onto the alginate coated silica surface, however, were statistically identical for all ionic strengths investigated, except for a small deviation at 30 mM NaCl.

According to DLVO theory, as ionic strength increases, the electrical double layer repulsion between the negatively charged PS and NOM coated surfaces (Figs. 4.4 and 4.5, respectively) is suppressed and the energy barrier to deposition is decreased. At high enough ionic strength, the energy barrier to deposition vanishes and the particle deposition is only limited by diffusion, meaning at and above this concentration, the attachment efficiency is equal to 1. The attachment of stretched and spherical PS onto alginate (Fig. 4.6b) is lowest at the lowest ionic strength, gradually increases with increasing ionic strength, and equals 1 at and above 100 mM NaCl, therefore these trends are in good qualitative agreement with DLVO theory.

The attachment of stretched PS onto HHA (Fig. 4.6a) follows a similar trend, again as predicted by DLVO theory. The attachment of spherical PS onto HHA, however, deviates significantly from the predicted trend. Total DLVO interaction energy was calculated for stretched and spherical PS onto both NOM surfaces at each ionic strength. The interaction energy profiles for spherical and stretched PS onto HHA are presented in Fig. 4.7 in the presence of 16 (a) and 200 (b) mM NaCl. At 16 mM NaCl, the predicted energy barrier to deposition for spherical PS is much larger than that of stretched PS, which is in contradiction with the observed attachment at the same experimental condition (Fig. 4.6a). The calculated energy barrier to deposition at 200 mM NaCl, while somewhat diminished, does

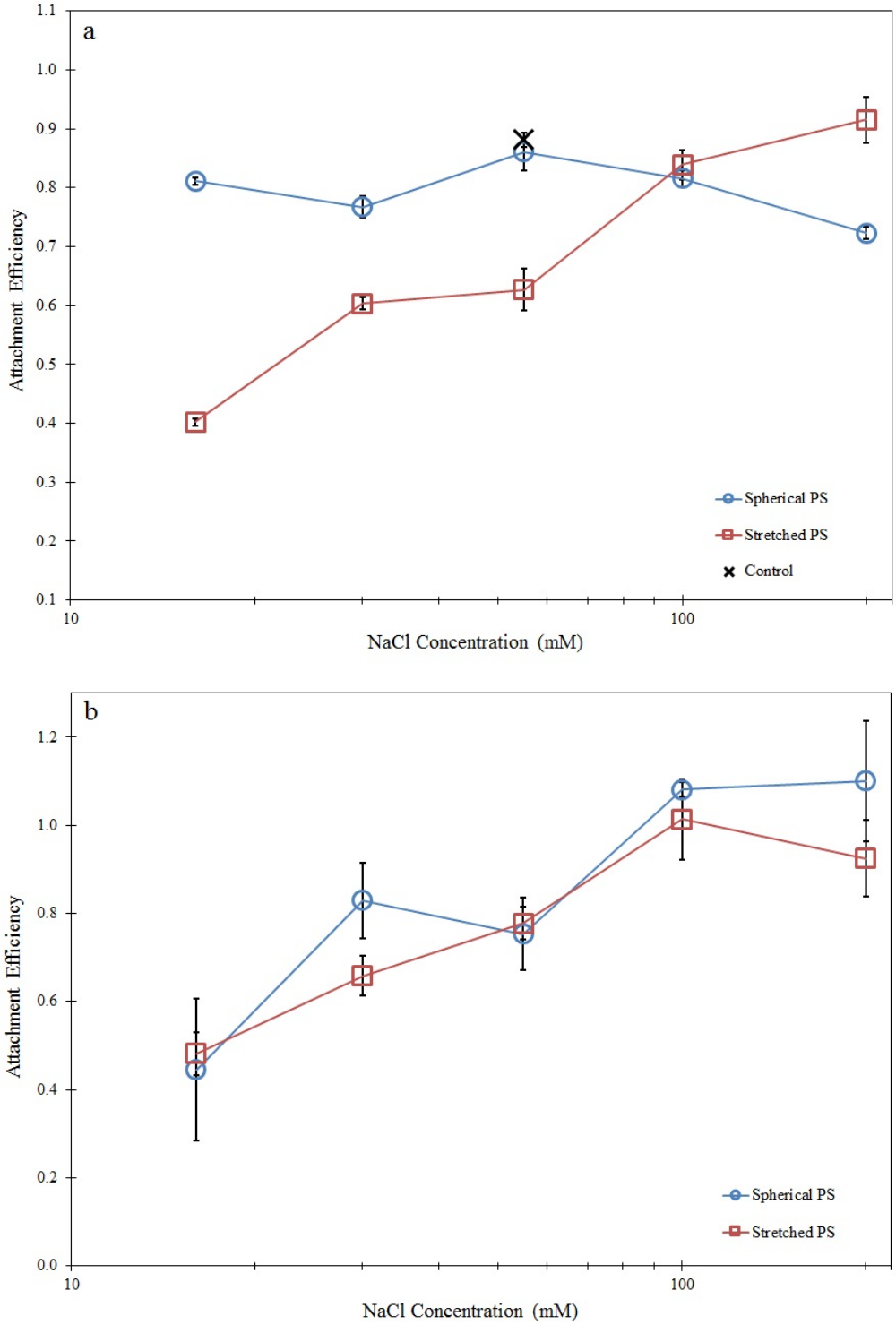

Figure 4.6: Attachment efficiency of spherical and stretched PS particles onto HHA (a) and alginate (b) coated silica surfaces as a function of ionic strength. Each value was the result of at least 4 independent measurements and error bars represent standard deviation.

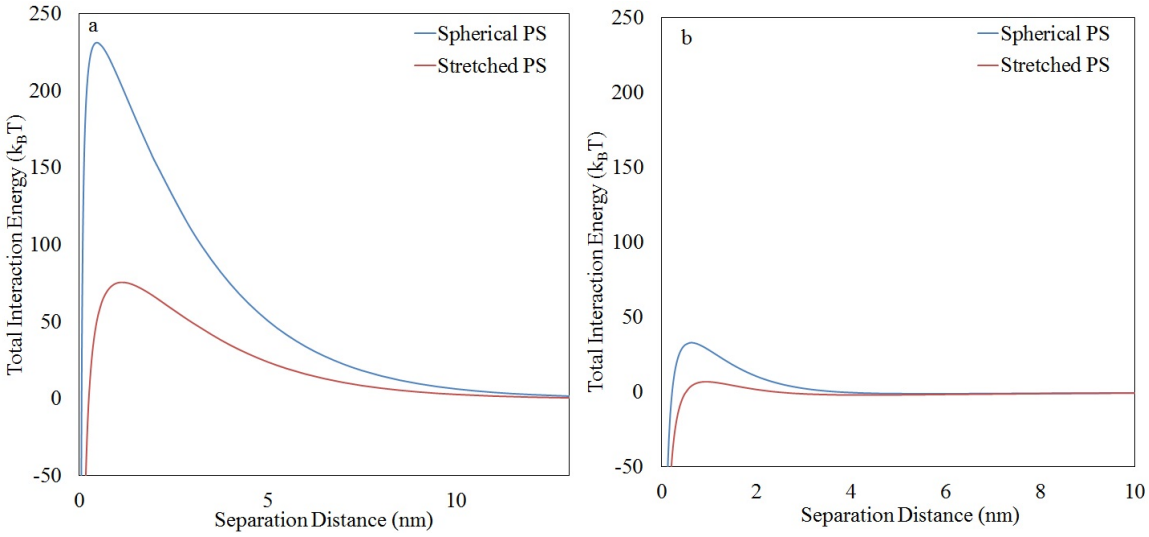

Figure 4.7: Calculated DLVO interaction energy for the deposition of spherical and stretched PS onto HHA in the presence of 16 (a) and 200 (b) mM NaCl.

in fact correctly predict the relative values of attachment at this condition. Since DLVO theory fails to correctly predict attachment at low ionic strength onto HHA, a non-DLVO force is most likely contributing.

4.3.3 Mechanistic insights

Both HHA and alginate layers were explored using AFM and representative images are reported in Fig. 4.8 a and b, respectively. The topography of the HHA surface is very heterogeneous, with large peaks extended from the surface, and a higher relative roughness. The topography of the alginate surface is smoother, with much fewer peaks extending from the surface relative to HHA. The rougher, more extended surface of the HHA layer possesses more voids than the alginate layer, and therefore an increased potential for particle entanglement. The smaller size of the spherical PS particles allow for entanglement in these relatively small voids, while the nearly doubled major axis diameter of the stretched PS hinder particle entanglement. Furthermore, investigation by the Voigt viscoelastic model [95] estimates that the mass of the HHA layer is more than 5 times larger than the mass of the alginate layer (Fig. 4.9). This also suggests that the HHA layer provides a much larger

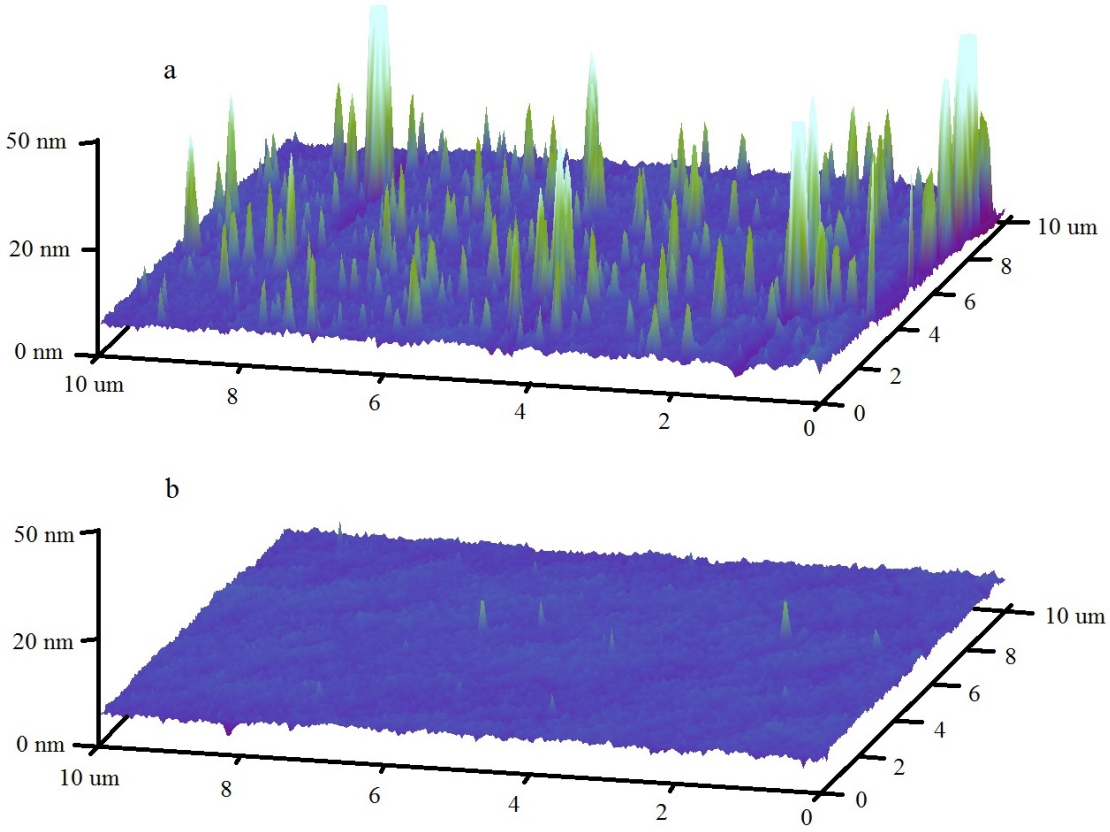

Figure 4.8: Representative AFM images of HHA (a) and alginate (b) coated silica surfaces.

mesh for particle entanglement. These findings are in agreement with two previous studies which reported increased attachment of spherical nC_{60} onto NOM coated surfaces in the presence of low ionic strength solutions [39, 66]. Particle entanglement, in this manner, is not considered in DLVO theory, and is therefore likely the main contributor to the observed deviation from DLVO theory at low ionic strength.

Immobilized macromolecule structure has been reported to depend heavily on the ionic strength of solution [116, 117]. Furthermore, NOM layers have been reported to condense in the presence of high ionic strength solutions [61, 66]. As ionic strength increases, the HHA layer condenses, likely induced by increased inter- and intra-molecular crosslinks, forming a smoother, less extended surface with fewer voids for particle entanglement. Since the condensed surface has a lower potential for particle entanglement, the particle

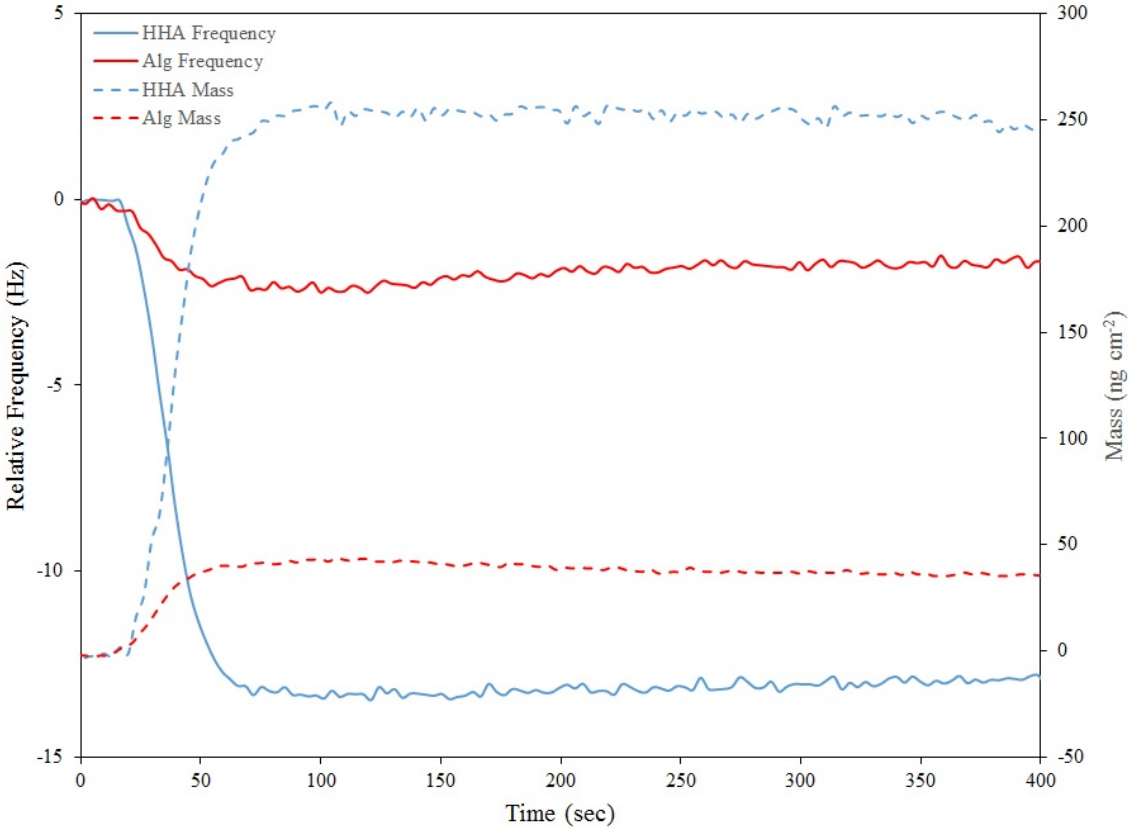

Figure 4.9: The mass of HHA and alginate layers as estimated by the Voigt viscoelastic model, plotted against the relative frequency of deposition.

entanglement effect seen at low ionic strength diminishes and DLVO forces dominate at high ionic strength. Since the size and shape of the spherical PS particles provide them no increased potential for attachment on the smoother surface, the reduced energy barrier to deposition (Fig. 4.7) allows the stretched PS to attach more readily than the spherical PS. Two previous studies have reported reduced attachment of spherical particles onto NOM layers as ionic strength increased [39, 66], however none have yet illustrated the dependency on aspect ratio reported in this study.

4.4 Conclusions

In this study, we showed that the attachment of colloidal particles onto NOM-coated surfaces can be greatly affected by the shape of the particles, depending on ionic strength and the type of NOM coating. In the presence of the alginate surface, the attachment of both spherical and stretched PS qualitatively agreed with DLVO theory. In the presence of the HHA surface, however, deviations from DLVO theory were observed. At low ionic strengths, spherical PS attached to HHA at a much higher rate than stretched PS. This deviation from DLVO theory can be explained by the increased surface heterogeneity and roughness observed for the HHA surface. More voids present in the HHA layer allows for a higher potential of spherical PS particle entanglement, while the enlarged major axis of the stretched particles hinder their ability to become entangled in the extended HHA surface. As ionic strength increases, the HHA layer condenses and the potential for spherical particle entanglement is reduced. At high ionic strengths, the HHA layer condenses to a point where DLVO forces dominate and the stretched particles attach at a higher rate than spherical particles, due to a reduced energy barrier to deposition.

Complex interactions exist between colloidal particles and environmentally relevant surfaces and, based on the findings presented in this study, it is clear that the shape of colloidal particles can play a major role in such interactions. If similarly complex interactions exist for other types of environmentally relevant surfaces, particle shape may greatly affect the environmental fate and transport of colloidal particles. A complete understanding of the role of particle shape will improve the accuracy of colloidal particle transport predictions, aiding in the assessment of risk and potential exposure pathways.

Chapter 5

Predicting particle attachment efficiency from physicochemical characteristics: a machine learning approach

5.1 Introduction

The work presented in this chapter is part of a collaborative effort [130] and is presented here with permission from the co-authors. Environmental applications of engineered nanomaterials (ENMs) have tremendous potential to enhance remediation of pollutants in the subsurface, to improve sustainability of nano-formulated plant protection products in comparison to traditional pesticides, and to improve nano-based plant nutrient delivery [131–133]. However, the increased production of ENMs, coupled with their apparent aquatic toxicity, [3, 9, 10] raise serious concerns about the fate and transport of these materials in the environment.

Our understanding of ENM transport in the subsurface is far from complete. Similar to larger, colloidal particles, the transport behavior of ENMs in the subsurface environment is a function of numerous deposition processes, which are controlled by a complex system of physical and chemical factors [56]. Despite numerous qualitative investigations that examine the influence of physical chemical factors on ENM transport [39, 61, 63–66, 81, 82, 104, 116, 121, 122, 124], relatively few quantitative insights have been gained. One contributing factor for the slow rate of progress is that it is not yet possible to identify and separate natural nanomaterials from engineered nanomaterials in complex environmental matrices [134]. As a result, investigation of ENM transport, particularly for high production volume nanomaterials (e.g., TiO_2 and ZnO), is limited to examination in simple, artificial soil systems. Another critical factor is that ENM transport is primarily investigated through experimentation with soil columns. Soil columns have been in use for more than 130 years and are the foundation for most fluid dynamics, but are too coarse to sufficiently understand

nano-scale processes. While advanced imaging techniques, such as high-resolution X-ray computed tomography of soil columns, enable non-destructive transport characterization, the scanning resolution is typically between 0.84μm – 4.4μm, which is too large to resolve ENMs, which are by definition less than 100 nm [135].

Quartz crystal microbalance with dissipation monitoring (QCM-D) enables real-time monitoring of nanoscale mass deposition. QCM-D monitors the deposition rate of particles onto an oscillating sensor surface, isolating deposition kinetics, and allowing for a direct measure of attachment efficiency (α) without contributions from convection or filtration, unlike traditional soil column experiments. α is an important kinetic transport parameter and is widely used in colloid filtration theory (CFT) to quantify the likelihood of a particle attaching to a surface after a collision. It is important to note that several closed-form correlations have been developed to predict α [136–140], although none explicitly consider the physicochemical conditions which have been reported to affect the value of α, including ionic strength [61, 63, 65, 66, 81, 104, 121, 122], pH [122–124], charge of particle and collector surface [39, 61, 63–66, 80, 104, 121–125], presence of organic matter, whether dissolved in solution [64, 66, 104, 123, 124] or coating the collector surface [39, 63, 64, 66, 80, 104, 124, 125], temperature [39], and particle shape [71, 82]. Furthermore, while the qualitative influence of these conditions on α has been well studied and, in some cases, reasonable mechanistic explanations are provided (e.g., agreement or disagreement with Derjaguin-Landau-Verwey-Overbeek (DLVO) theory [58, 59]), a predictive model of α that explicitly considers these conditions has not yet been developed.

Machine learning allows us to develop empirical models from complex systems where the underlying relationships between the data are too complex to develop by hand [83]. Machine learning has been successfully applied to a wide range of complex problems, including speech and computer vision, self driving cars, search engines, and medical diagnoses [84–87]. In two recent studies [88, 89], machine learning was applied to predict the toxicity and biological impacts of ENMs, based explicitly on the molecular properties

of the nanomaterial. Despite the successes of machine learning in a wide range of applications, it has not been applied to the complex task of modeling environmental transport until very recently. A very recent study by Goldberg et al. [90] employed ensemble machine learning (random forest) regression and classification to predict the retained fraction (RF; the fraction of materials retained during a soil column experiment in comparison to the total mass of materials injected into the column) and shape of retention profile (RP) using a database of more than 200 nanomaterial column transport experiments amassed from published literature. Goldberg et al. [90] reported that their model was able to predict the RF with a mean squared error between 0.025–0.033, and the RP with an expected F1-score (the weighted harmonic mean of precision and recall) between 60–70%. Further, by recursively removing physical and chemical features to optimize model predictive performance, the authors were able to rank the importance of the physicochemical state features (e.g., pH, ionic strength, nanomaterial type, etc.) to ENM transport.

The high variability in reported α values under seemingly similar experimental conditions is one reason why these data have not yet been successfully modeled. For example, the presence of an attached layer of natural organic matter (NOM) has been reported to hinder, enhance, or have no effect on α under similar solution conditions [64, 66, 81]. The purpose of this work is to combine all of the available α data in order to identify which of the complex set of variables are most important and, ultimately, produce a predictive model for α based on the identified variables. Here, 299 total experiments with 13 physicochemical features each were chosen from 12 publications [39, 61, 63–66, 81, 82, 104, 116, 121, 122, 124] to form the largest QCM-D derived α database to date. Ensemble machine learning (gradient boosting decision trees) was employed to empirically relate the physicochemical state (i.e., physicochemical training features) to the α values (i.e., target feature) measured by QCM-D. Grid search hyper parameter optimization with cross validation (GSHPOCV) and recursive feature elimination with cross-validation (RFECV) were employed to optimize model performance. To identify the physicochemical features most

important to prediction, RFECV results from 100 model runs were aggregated and investigated to identify the physical and chemical features critical to predicting α. The predictive, empirical model presented here will aid in identifying which physicochemical characteristics are most influential to α. An improved understanding of transport parameters is key to accurately predicting the impact of new particle types and making risk-informed regulatory decisions, or even designing new ENMs to be safe from the ground up.

5.2 Methods

5.2.1 Database

The database developed for this work includes 299 separate experiments extracted from 12 peer-reviewed QCM-D particle transport studies [39, 61, 63–66, 81, 82, 104, 116, 121, 122, 124]. From each experiment, 13 physicochemical training features were recorded and 1 target experimental result feature i.e., α was chosen. Studies which reported particle deposition rate but not particle attachment efficiency were not included in the database. As mentioned previously, in order to calculate α from particle deposition rates, the favorable deposition rate at identical experimental conditions must be known, and so without this knowledge, α could not be extrapolated from particle deposition rates. Furthermore, studies which explored particle deposition onto oppositely charged surfaces were not considered, as $\alpha = 1$ in these cases, by definition. The investigated applicability domain and range of training and target features employed for this study are presented in Table 5.1.

Table 5.1: Investigated domain of physicochemical training and target features.

Training Features	Range Investigated
Particle Type	C60, $C60_{20h-UV}$, $C60_{7D-UV}$, ZnO, PS, MS2RNA, BL21RNA, MWCNTs, $MWCNTs_{LO}$, $MWCNTs_{HO}$, TiO_2
Debye Length	0.5 – 56.2 [nm]
Salt Type	NaCl, $CaCl_2$
Particle ζ-potential	-48.5 – 3.31 [mV]
Collector ζ-potential	-79.6 – -21.4 [mV]
pH	5.2 – 8
Dissolved NOM Type	None, SRHA, EHA, Alg
Dissolved NOM Concentration	0 – 10 [mg/L]
Immobilized NOM layer	None, HHA, HFA, SRHA, EHA, Alg
Temperature	15 – 45 [°C]
Shape	Sphere, ellipsoid, tube
Suspension Preparation Method	Liquid-liquid exchange, direct sonication, commercial stock
Particle Concentration	5 – 100 [mg/L]

Target Features	Range Investigated
α	$4.1 \cdot 10^{-4}$ – 1.7 [-]

Alg: alginate; 7D-UV: 7 day UV exposure; 20h-UV: 20 hour UV exposure; EHA: Elliott humic acid; HHA: Harpeth humic acid; HFA: Harpeth fulvic acid; LO/HO: Lowly/highly oxidized; MWCNTs: multi-walled carbon nanotubes; NOM: natural organic matter; SRHA: Suwannee River humic acid; PS: polystyrene, MS2/BL21 RNA: RNA extracted from bacteriophage MS2 and *E. coli* BL21

The physicochemical features (listed in Table 5.1) were chosen based on three criteria:

(i) features that have been reported to affect α, i.e. particle type, presence of NOM, salt

type, Debye length (through ionic strength), temperature, shape;

(ii) features that affect interaction energy, i.e. Debye length, ζ-potential of particle and collector, pH; and

(iii) features that have been reported to affect particle properties, i.e. suspension preparation method, particle shape.

Particle size was excluded as a physicochemical feature because the diffusion rate influences both favorable and unfavorable deposition conditions equally and therefore has no net effect on α. Furthermore, there were large inconsistencies in particle size reporting, due to simultaneous particle aggregation during QCM-D experiments for certain particle types exposed to high ionic strengths. Dissolved NOM, which consists of NOM dissolved in solution within the particle suspension and likely adsorbed to the particle surfaces, is differentiated from the immobilized NOM layer, which is attached to the sensor surface by electrostatic layer-by-layer (LbL) assembly. In some cases, the values for zeta potential of particle or collector surface were not reported, so values were interpolated from reports of identical particle or surface type under similar solution conditions. When electrophoretic mobility was reported, zeta potential was estimated using the Smoluchowski approximation [114].

A graphical depiction of the relationship between the training and target features is shown in Figure 5.1. Each circular layer represents a training feature of the database and the legend located at the top of the figure denotes the order of the circular layers, starting with the innermost circular layer. The outermost layer is the target feature, α. Each layer is color coded by value, according to the values (or range of values) listed below the legend. A value of zero (or the absence of a NOM layer or dissolved NOM) is represented by the color white in each layer. For more precise browsing, a live figure is provided online [141].

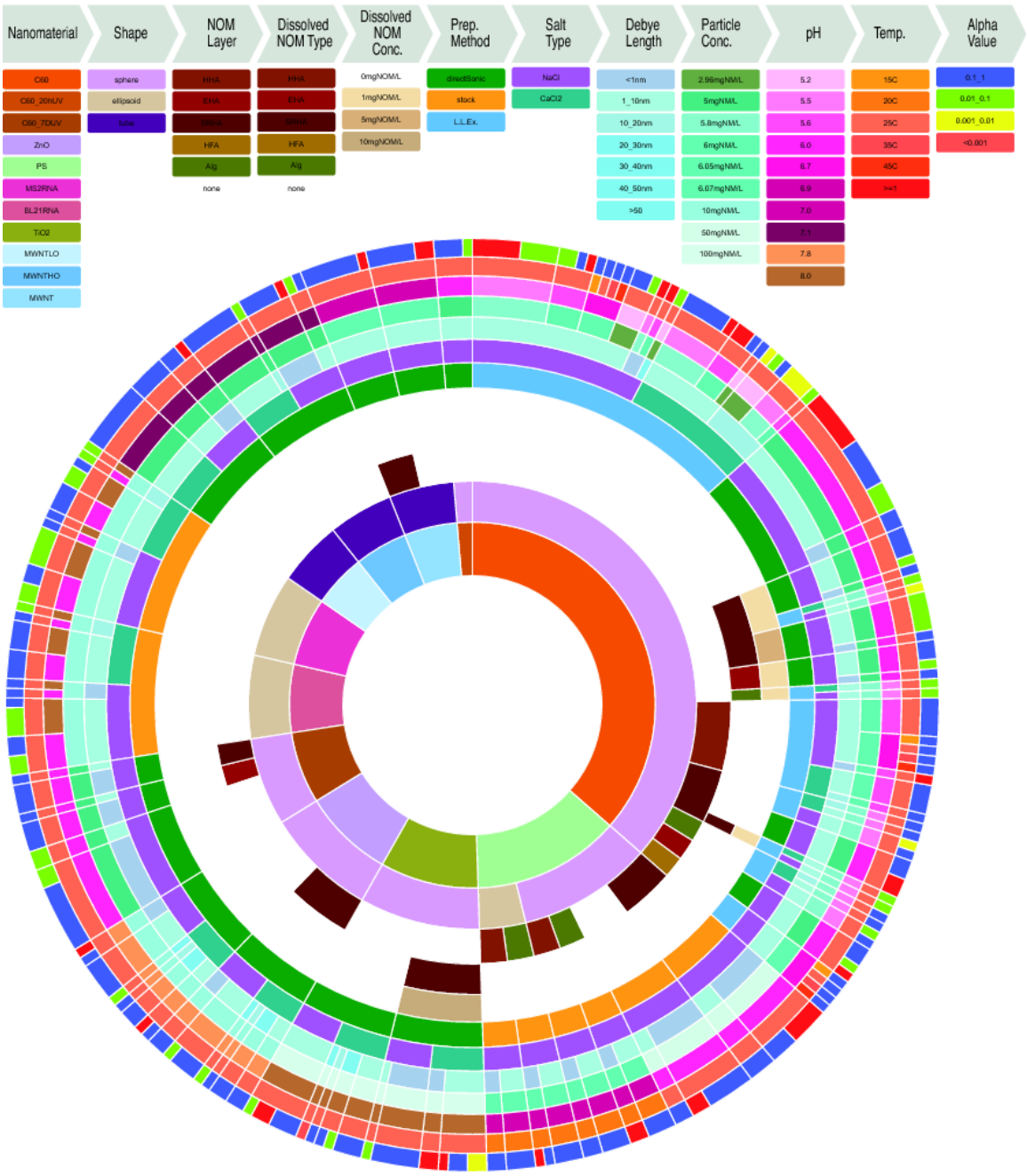

Figure 5.1: Graphical representation of the α database amassed for this work.

5.2.2 Machine learning

To attain the best prediction performance, several machine learning regression methods (random forest, ADA boosting, decision tree, and gradient boosting) were evaluated simultaneously with the provided model structure (Figure 5.2), which includes automated hyper parameter optimization (GSHPOCV) and feature selection sub routines (RFECV). Python and scikit-learn package [142] were employed for model construction and the entire model is available for distribution online. In this work, we present gradient boosting regression as it provided higher prediction performance with lower variance in comparison to the other methods.

Gradient boosting regression is an ensemble machine learning method that combines a series of decision trees in a forward stage-wise fashion. In the first stage, a single-layer decision tree is trained to fit the regression data. In each sequential stage, a new single-layer decision tree is fit to the previous models' residuals and appended to previous layer(s). By sequentially fitting the residuals, the model iteratively increases its ability to predict observations modeled poorly by the previous steps. Overfitting occurs when trees are added in excess, which increases the likelihood that the model considers noise within the training data to be important. Standard gradient boosting regularization strategies were employed to prevent overfitting by calibrating the number of stages to minimize the test-train deviance (Appendix C), restricting the tree complexity (number of nodes), and by employing a learning rate parameter <1 to shrink the contribution of each tree as it is added to the model. Note that the learning rate and the number of boosting stages parameters are selected by GSHPOCV and propagated throughout for each model run.

5.2.3 Model structure

To provide internal estimates of error and generalizability, the database was partitioned into training, cross validation, and testing data sets (the testing partition is called the 'hold-

out' partition to prevent confusion with cross validation testing). A schematic of the model structure is shown in Figure 5.2 and supplemented with a textual description.

Overall, 100 model runs were performed. For each model, all usable experiments within the database were randomly assigned to the holdout (15%) or training (85%) data sets. No training was performed on the holdout set. Next, grid search hyper parameter optimization with cross validation (GSHPOCV) was performed to identify the best performing combination of model parameters (i.e., the parameter combination that resulted in the highest R^2 cross-validation score) [142]. A description of the GSHPOCV routine, and a breakdown of the investigated hyper parameter space are provided in Appendix C. Following GSHPOCV, recursive feature elimination with 5-fold cross validation (RFECV) was employed to identify the minimum number of training features required to maximize model performance [90, 142]. A description of the RFECV routine is provided in Appendix C. The training set was then 'trimmed' to the features identified by RFECV and a new model was trained on the trimmed training set and evaluated against the holdout set (i.e., the holdout set training features [physicochemical features] are fed into the model and accuracy of the model to predict α is evaluated in comparison to the ground truth values.)

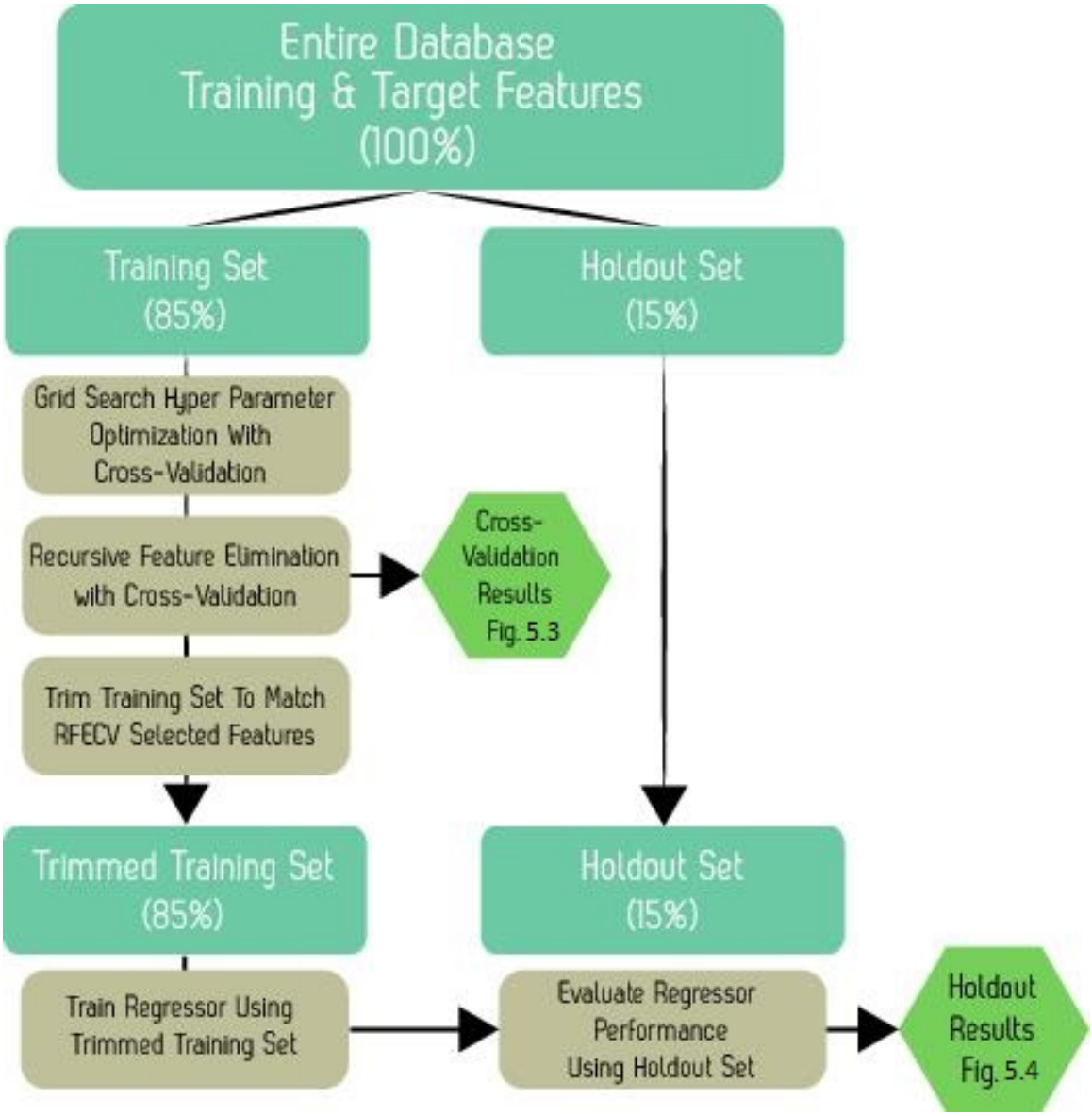

Figure 5.2: Graphical depiction of data partitioning scheme and model structure. The fraction of training and target features employed for each step are shown in parentheses. In the first step, the database is divided into the holdout set (15%) or the training set (85%). No training is performed on the holdout set training features. Grid search hyperparmeter optimization with cross validation (GSHPOCV) is employed to determine the optimum machine learning parameters on which to train the model, which are employed throughout the rest of the model run. Next, unimportant features are removed from the database using recursive feature elimination with cross validation (RFECV; Figure 5.3). The model is retrained on the trimmed training set and evaluated using the holdout set to produce the holdout results(Figure 5.4).

5.3 Results and Discussion

5.3.1 Recursive feature elimination with cross validation

The performance of the model (measured as R^2) to predict α as a function of the number of features selected during RFECV training can be seen in Figure 5.3. The performance associated with predicting α during RFECV is a very conservative estimate of the generalized performance of the predictive model and is not representative of overall model performance because it is trained on a reduced data set (68% of the total database is employed for RFECV score; 85% is employed for prediction against the holdout set). It can be seen from Figure 5.3 that performance increased when the model is trained with larger feature set sizes, as expected, with a marked increase in performance (20% median performance gain) occurring between 7 and 8 features chosen. Progressing from 8 to 13 features continues to decrease the variance in model performance, decreases the observation frequency of outliers, and improves the remaining outlier score (i.e., outliers move closer to the bulk of the data). In terms of cross validation performance, there are diminishing returns to adding more features. Median performance increases by 5% between 8 and 10 features, however a performance increase of only 2% is observed between 10 and 13 features.

5.3.2 Attachment efficiency prediction performance

The model performance in predicting α for the holdout set as a function of the number of RFECV selected features to train the model can be seen in Figure 5.4. The lack of performance data below 8 features indicates that the model performance was never optimal when fewer than 8 features were employed for model training. The median performance to predict α in the holdout set was higher for each feature set size as compared to the RFECV performance. This is to be expected because the model was trained on the entire trimmed training database (additional 17% in comparison to the RFECV).

In order to identify the highest performing model utilizing the fewest number of fea-

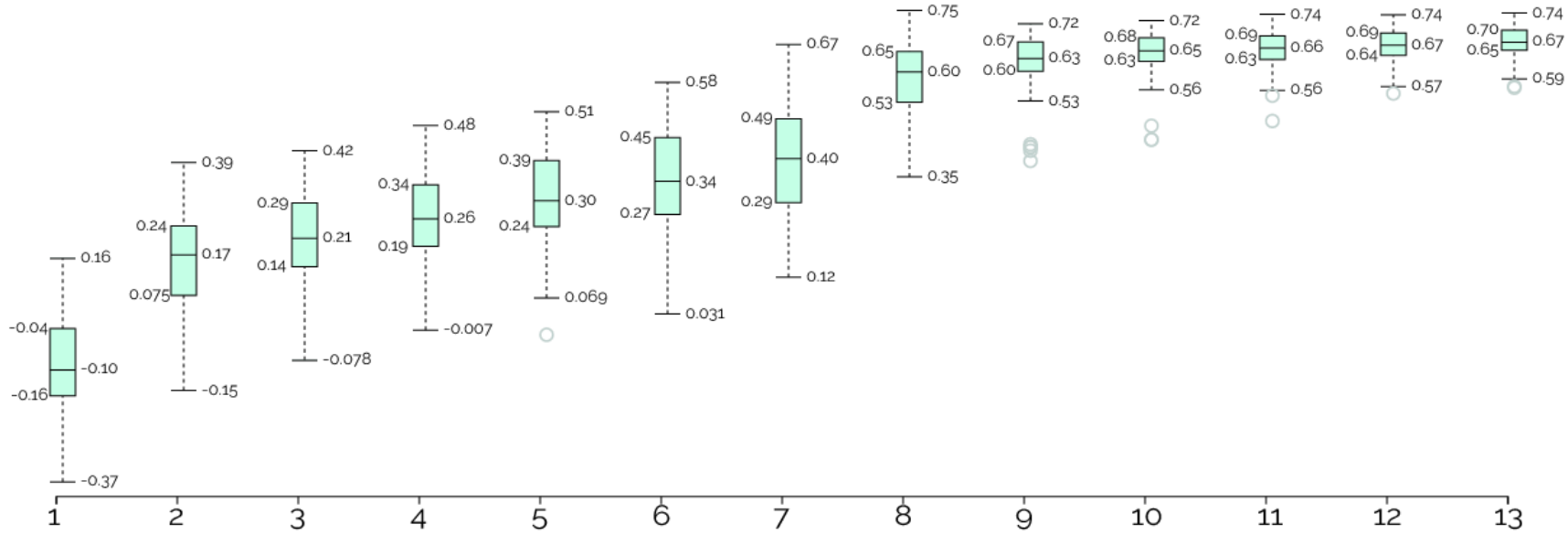

Figure 5.3: Aggregate model performance in predicting α in the cross validation test fold during the 500 RFECV model runs. The model performance (measured as R^2) as a function of number of features chosen is shown, with the box plots representing the minimum, maximum, median, and interquartile range of R^2 values. Circles represent statistical outliers.

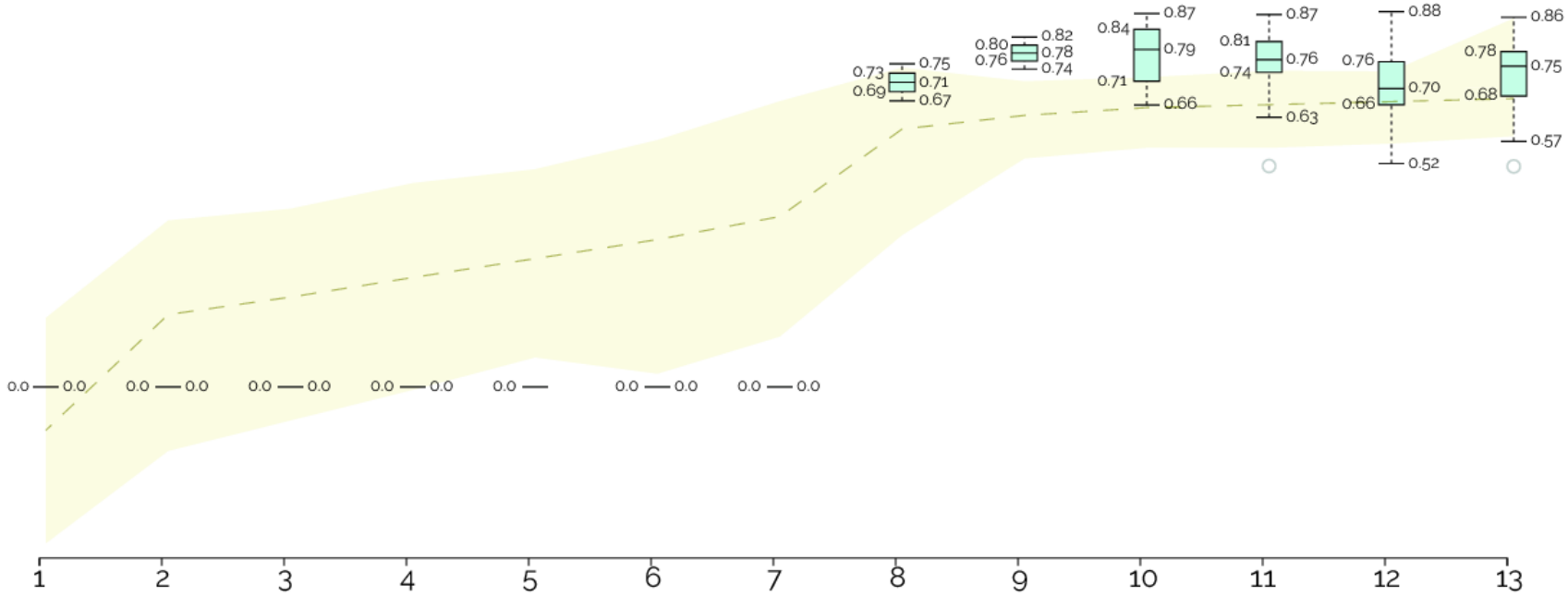

Figure 5.4: Aggregate model performance in predicting α in the holdout set as a function of the number of RFECV selected features. For each model run, the database was trimmed to the number of features selected by RFECV, the model was retrained on the trimmed database, and then the α prediction accuracy (measured as R^2) was evaluated using the holdout set. Box plots represent the minimum, maximum, median, and interquartile range of R^2 values. Circles represent statistical outliers. The minimum to maximum range of RFECV cross validation R^2 values are represented by the green shading, with the dotted line representing median values for model performance comparison.

tures, the optimum result was chosen using Equation 5.1, where $n_{features}$ is the number of features employed for a given feature set size, R^2_{median} is the median R^2 value corresponding to the aggregated median predictive accuracy of holdout scores for a given feature set size, r_{IQ} is the interquartile range of the aggregated holdout scores for a given feature set size, and $F_{observation\ \%}$ is the percentage of model runs that result in a given optimum feature set size. A summary of the values utilized in determining the optimum model and the resulting optimum result value from Equation 5.1 are reported in Table 5.2.

$$\text{Optimum result} = \max\left(\frac{1}{n_{features}} \cdot \frac{1}{(1-R^2_{median})} \cdot \frac{1}{r_{IQ}} \cdot F_{observation\ \%}\right) \tag{5.1}$$

Table 5.2: Summary of values utilized in determining the highest performing model with the fewest number of features and resulting optimum values using Equation 5.1.

Feature Set Size	8	9	10	11	12	13
RFECV Selection Frequency	2%	2%	6%	14%	19%	57%
Median R^2	0.71	0.78	0.79	0.76	0.7	0.75
Interquartile Range	0.04	0.04	0.13	0.07	0.1	0.1
Optimum Result Value	0.22	0.25	0.22	0.76	0.53	1.75

The highest median performance corresponded to a selection of 10 features, however RFECV only selected an optimal model of 10 features in 6% of the total model runs. Feature sets consisting of 8 and 9 features reported the lowest variance (interquartile range), however feature sets of size 8 and 9 were chosen for only 2% of the total RFECV model runs, respectively. This indicates that there is a subset of data that can be predicted more accurately with fewer features. In general, however, model prediction performance is more frequently optimal for feature sets consisting of 13 features. Feature sets of 13 features were chosen for 57% of model runs. The next most frequently observed feature set sizes consisted of 12 and 11 features, and were observed for 19% and 14% of the model runs, respectively. Due to the corresponding high model performance, high RFECV selection

frequency, and low interquartile range, the model consisting of all 13 identified physicochemical features was chosen as the optimum. This result suggests that the relationship between the 13 physicochemical features chosen in this study and α is a complex one that likely depends heavily on all chosen features.

5.3.3 Implications of database findings

By analyzing the range of features investigated within the α database in comparison to environmentally relevant conditions, future α experiments can be guided towards areas in need. Figures 5.5 and 5.6 illustrate the range of ionic strength conditions and dissolved NOM content, respectively, explored within the α database. The cross-hatched areas within each figure represent the range of ionic strength conditions and dissolved NOM content reported in typical groundwater, according to Freeze and Cherry [143].

It can be seen in Figure 5.5 that the typical groundwater ionic strength range (0-25 mM) is covered quite well by the majority of the experiments explored within the α database, however there are quite a few experiments at ionic strengths well above this range. Because these experiments fall so well outside the range of typical groundwater, any observed effects are likely not applicable or important to transport through the subsurface environment, unless a brackish or saline area is being considered. While some experiments do fall within the typical groundwater dissolved NOM concentration range (0.1-10 mg/L) in Figure 5.6, the majority of the experiments within the α database were performed in the absence of dissolved NOM. Because the presence of NOM has been shown to alter α quite drastically (depending on the type of NOM and solution conditions present), the conclusions drawn from these studies are likely not applicable to transport through the natural environment, unless an area of unusually low NOM content is being considered. Because of these findings, future α experiments should include dissolved NOM in the typical concentration range (0.1-10 mg/L) to maximize the utility of experimental findings.

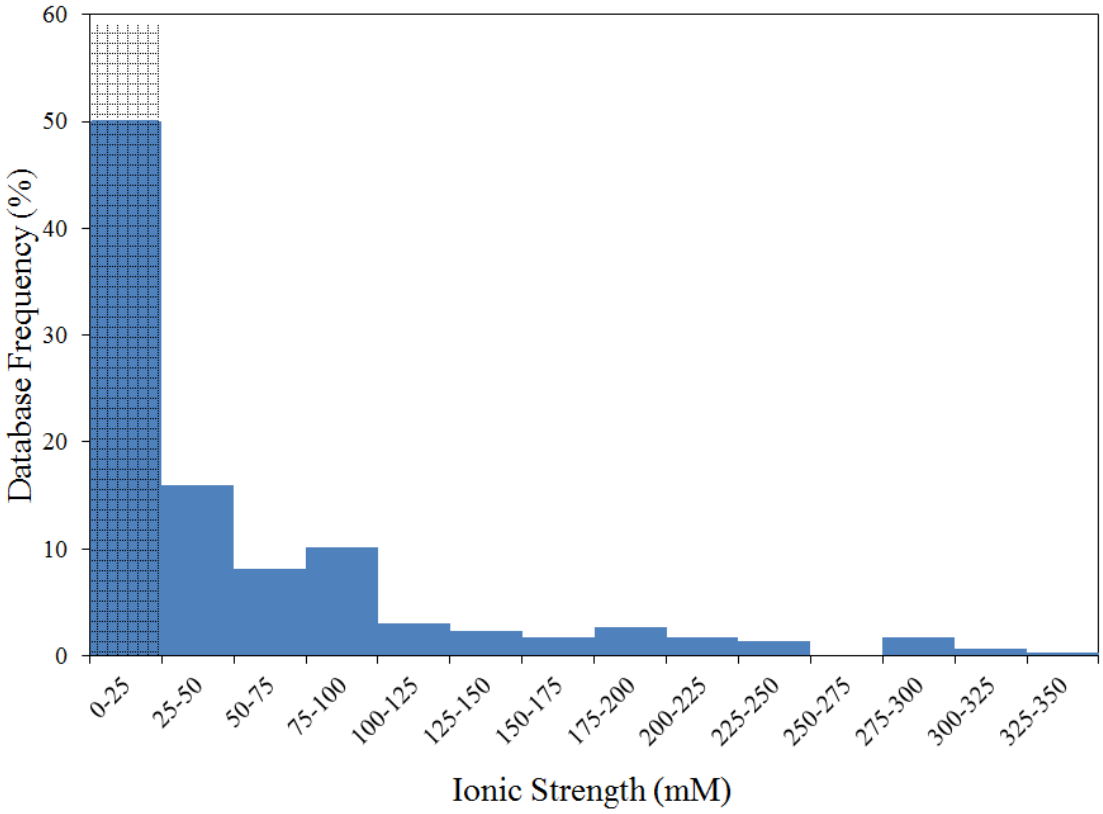

Figure 5.5: Range of ionic strength conditions explored within the α database, expressed as the percentage of total experiments. The cross hatched area represents the ionic strength range of typical, fresh groundwater [143].

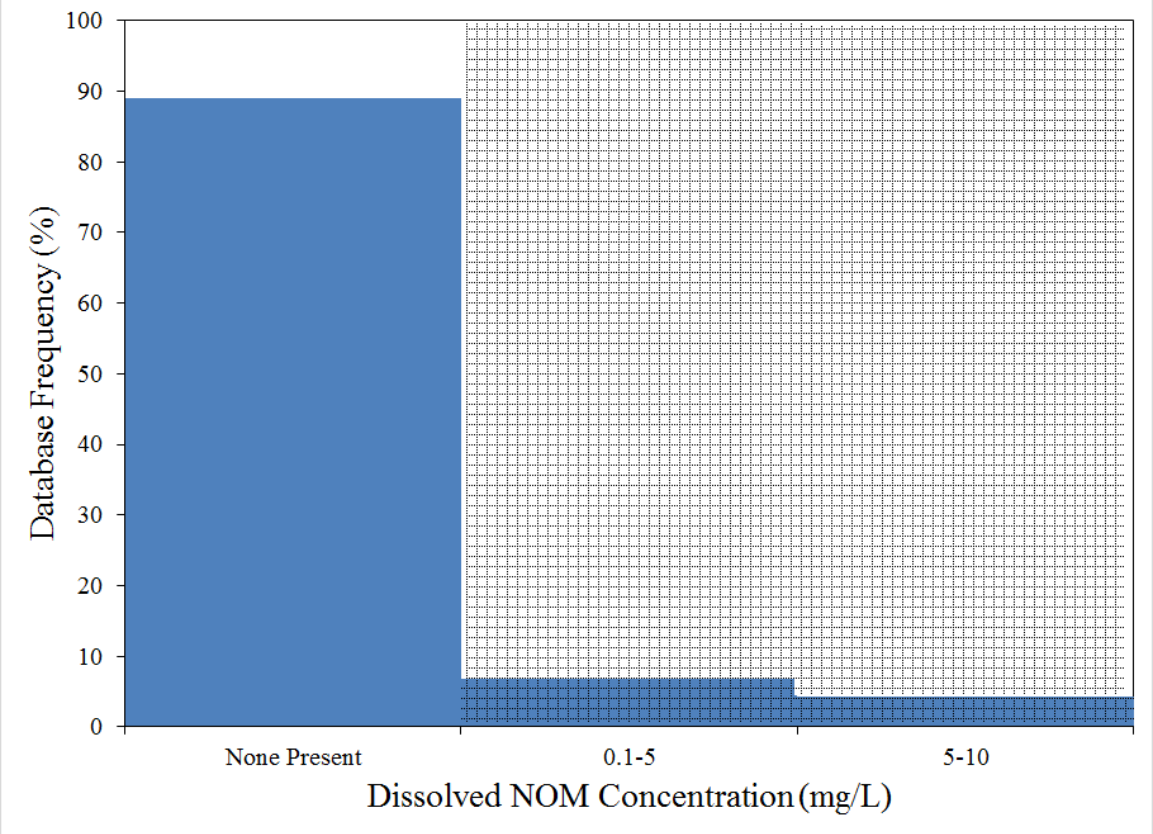

Figure 5.6: Range of dissolved NOM concentrations explored within the α database, expressed as the percentage of total experiments. The cross hatched area represents dissolved NOM concentration range of typical groundwater [143].

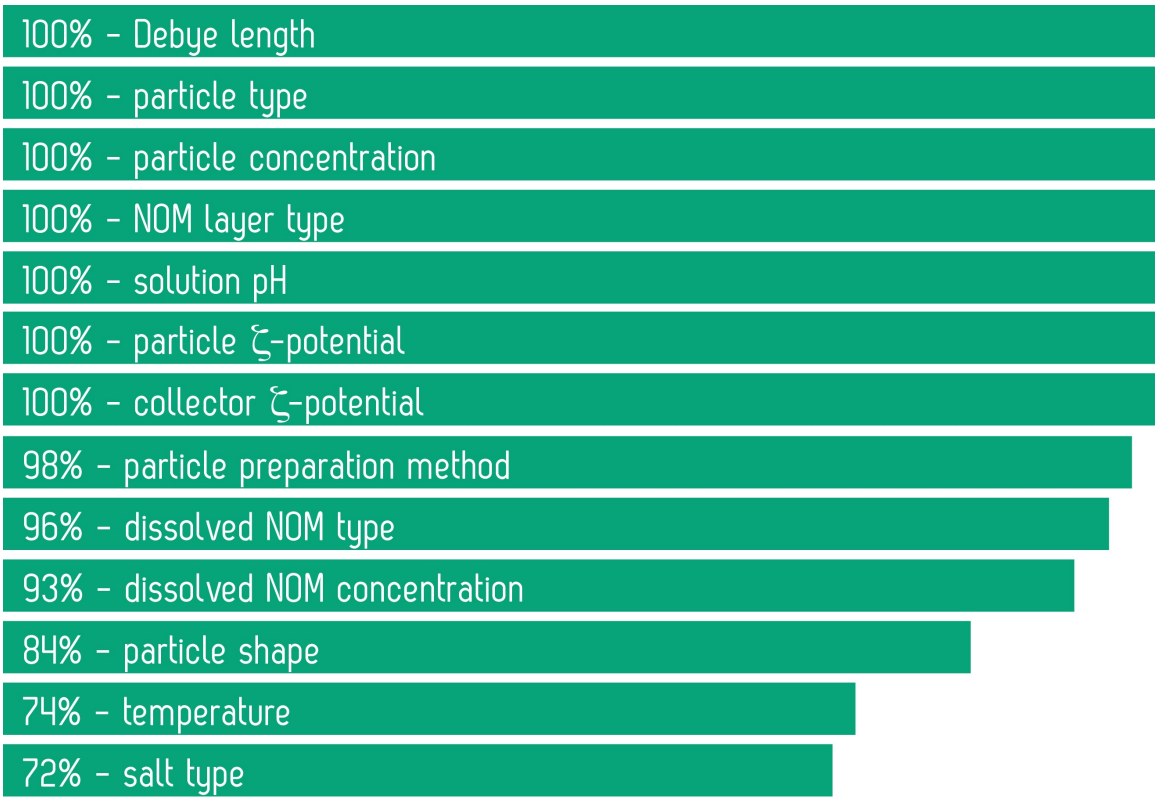

Figure 5.7: Relative feature importance, reported as percentage of total model runs in which each feature was included in the optimal model to predict α.

5.3.4 Implications of model findings

In order to identify the features most important to accurately predicting α, a ranked chart is presented in Figure 5.7 based on the percentage of total model runs in which each feature was included in the optimal model to predict α.

The features included in the optimal predictive α model with 100% frequency were not surprising, as they have been the focus of many quantitative α studies, including the studies utilized in the training database for this work (i.e., Debye length, particle type, particle concentration, NOM layer type, solution pH, particle ζ-potential, and collector ζ-potential). The feature chosen in the optimal model with the lowest relative frequency, salt type, might seem surprising at first due to the importance of ion valence on particle-surface interaction energy [58, 59]. It should be noted, however, that the salt type is included within

Debye length (as ionic strength) and so the results presented here suggest that the salt type has a somewhat limited influence on top of influencing Debye length. Furthermore, this finding is in agreement with a recent study by Goldberg et al. [90], which reported that salt type was of relative low importance to predicting the retained fraction of ENMs in column experiments when a random forest machine learning model was trained on the data. Temperature was reported to be the second least frequent feature included in the optimal model (albeit still quite often at 74%), despite having been reported to greatly alter the α of nC_{60} onto NOM coated surfaces in a study by McNew and LeBoeuf [39]. The authors do report, however, that temperature has no effect on nC_{60} attachment to uncoated surfaces. These findings seem to agree with our ranking of temperature below other features which have been shown to affect α regardless of the presence or absence of a NOM layer.

The shape of the learning curve presented in Figures 5.3 and 5.4 in combination with the relatively high model performance for predicting the holdout set suggest that the α database amassed for this work is well suited to prediction by a machine learning model. This finding also validates the selection of the 13 features used to train the model, by confirming that these features describe the changes in α well. While it is possible that an important parameter was overlooked (e.g. Hamaker constant), the results presented here indicate that there is enough information provided by the physicochemical characteristics of the particles and depositional system to predict α with relative accuracy. This is not surprising, however, since most transport parameters are controlled by the physicochemical properties of the system, and therefore would provide redundant information if they were to be included in a model based explicitly on physicochemical characteristics. Whether or not this finding extends to α values measured by column experiments or other transport parameters, however, is not yet known. Further, applicability beyond the investigated experimental domain is not known and the model must be retrained, and re-evaluated, when new data is added.

While there has been tremendous focus on developing mechanistic models to predict

ENM transport, our mechanistic understanding, even in simple, synthetic systems, is insufficient to enable prediction [79]. As a result, the applicability of mechanistic methods outside the experimental state on which the models are conditioned is too limited, primarily because the influence of physicochemical conditions on transport is not well understood and it is difficult to gain process understanding using conventional experimental and modeling methods.

In this work, we provided an empirical method to disentangle the complex interaction between physicochemical conditions and α to enable the prediction of α under a wide range of complex environmental and particle conditions. Model performance results indicated that the prediction of α is dependent on all 13 features, which evidences the complex relationship between α and the physicochemical state. In this work, we provided an empirical method to sort out the complexity and enable prediction of alpha under a range of complex conditions. The optimum model chosen in this work consisted of all 13 features, illustrating the complex relationship between α and the chosen features, which depends heavily on all physicochemical features identified in this work. This finding suggests that future mechanistic models for predicting α should focus on all features identified in this work, especially those selected for prediction in the optimum model with 100% (or near 100%) frequency, i.e. Debye length, particle type, particle concentration, NOM layer type, solution pH, particle and collector ζ-potential, particle preparation method, and dissolved NOM type. The features identified as most important to the quantitative prediction of α in this work have been previously reported to qualitatively affect the value of α [39, 61, 63–66, 81, 82, 104, 116, 121, 122, 124], further validating the findings presented in this work. Finally, the findings presented here should be used to conduct informed experiments. By measuring and reporting the features identified as important within this work, future α experimentalists can ensure their work to be as quantitatively useful as possible and efficiently aid in the future effort of constructing a mechanistic model to describe α.

The approach developed herein provides a fundamentally new method to understand

particle transport. As such, the method could be used to support risk-informed decisions concerning particle fate and transport by predicting transport behaviors of new and potentially dangerous materials. This enables a sophisticated understanding of risk without waiting on the development of a mechanistic model. Furthermore, this approach could support innovation of new materials as well, by allowing particles to be designed safely from the ground up. With a better understanding of exactly which physicochemical characteristics of the particle affect transport, the transport of a new material could be considered during development. By tweaking these characteristics, particle transport can be controlled from the very beginning, leading to a diminished environmental impact before the particle is even manufactured.

5.4 Conclusions

In this work, we presented an empirical model to predict α explicitly based on physicochemical characteristics of the particles and depositional environment. The observed model performance (Figures 5.3 and 5.4) indicates that prediction of the α database was well captured by the machine learning method chosen and the 13 physicochemical characteristics selected. Results from predicting the holdout set (Table 5.2) suggest that the relationship between α and the prediction features is a complex one, relying on all 13 physicochemical features selected. The features reported as most important to the accurate prediction of α (Figure 5.7) are in agreement with previous studies and the features reported as less important are either somewhat redundant (salt type) or have been previously shown to only affect α under certain conditions (temperature).

In summary, the intended utility of this work is threefold by:

(i) providing an accurate, quantitative prediction of α based explicitly on physicochemical characteristics;

(ii) directing future mechanistic modeling efforts towards the physicochemical characteristics most critical to prediction of α; and

(iii) guiding future experiments as to which characteristics are most important to measure and report in order to maximize the scientific benefit of results.

In conclusion, the results presented here illustrate that the relationship between α and the explored physicochemical conditions is too complex to be investigated by a single study alone. Only through compilation of reported α experiments from many different authors and incorporation into an all encompassing model, were we able to predict α based explicitly on physicochemical conditions. Furthermore, similar steps need to be taken to improve the understanding of all aspects of particle transport. Only through compilation of data in coordination with advanced modeling techniques can we make progress towards an all

encompassing understanding of transport. In short, we need to close the gaps between experimental understanding and quantitative predictive modeling, in order to maximize the benefit of the high quality transport data being reported on a regular basis.

Chapter 6

Conclusions and Future Work

6.1 Conclusions

The work presented in this dissertation has centered around quantitatively investigating the relationship between particle attachment efficiency and several physicochemical and solution characteristics. Each chapter has focused on a different characteristic, building on knowledge from the previous one. The work culminates with Chapter 5, which combines all of the data presented in previous chapters with all relevant published data to produce a predictive model for particle attachment efficiency based explicitly on physicochemical characteristics.

Chapter 2 focused on varying the type and physicochemical properties of SOM layers in order to identify their role in particle attachment efficiency. The work presented in Chapter 2 illustrated that the attachment of nC_{60} to immobilized layers of HHA and HFA is greatly affected by temperature and that the trend in attachment efficiency onto the SOM layers deviate greatly from that of bare silica. Both types of SOM layers hinder attachment at low temperatures. The attachment efficiency then begins to rise as temperature increases, eventually resulting in enhanced attachment at high temperatures, in the case of the HHA layer (Fig. 2.9). Based on thermal characterization of the SOM layers compared to the corresponding attachment trends (Figs. 2.10 and 2.11), the attachment efficiency is strongly correlated with hydration of the layer. Regions of rapid hydration correspond to steep increases in attachment and regions of slowed or decreased hydration correspond to lower increases in attachment. Possible mechanisms explaining this phenomenon include water-assisted disruption of polar SOM contacts and hydration induced swelling of the SOM matrix. This thermal effect on the attachment of nC_{60} to SOM may prove to be crucial in understanding the fate and transport of ENMs in areas that are rich in SOM, like

the subsurface environment, because humic substances typically represent the dominant organic components in soils and sediments. In areas that see large temperature fluctuations throughout the year, we may see a much larger uptake of ENMs in the warm seasons and less uptake in the cold seasons. Understanding how ENMs interact with individual components of soil is crucial to understanding the fate and transport of ENMs in a complex soil system, leading to their eventual impact on ecosystem and human health. The thermal effect illustrated in Chapter 2 may also prove useful in the removal of similar ENMs from wastewater or drinking water, by exploiting the much higher attachment efficiency at increased temperatures.

Chapter 3 focused on investigating the role solution chemistry plays on attachment efficiency by varying the salt concentration and ion valence. Results from Chapter 3 indicate that the presence of a HHA coating can both hinder and enhance nC_{60} attachment onto a silica surface, depending on solution chemistry. At low electrolyte concentrations, the HHA coating enhances nC_{60} attachment for both mono and divalent cations. By lowering the surface potential of the silica surface, the HHA coating significantly reduces the energy barrier to nC_{60} deposition. As electrolyte concentration rises, the HHA coating eventually results in a hindering of attachment for both mono and divalent cations. Though still lowering the surface potential of silica, the HHA coating doesn't significantly lower the energy barrier to deposition at these elevated electrolyte concentrations, due to the significant suppression of EDL repulsion resulting in a near zero energy barrier to nC_{60} deposition. Furthermore, the structure of the HHA coating likely condenses at elevated electrolyte concentrations, leading to a more compact and smoother surface with less potential for nC_{60} particle entanglement, contributing to the observed reduction in attachment efficiency. Because of the aforementioned reasons, we hypothesize that the summation of two contributing forces are responsible for the observed trend in nC_{60} attachment onto HHA-coated silica:

(i) the reduction in electrostatic repulsion due to the HHA-coating, and

(ii) HHA layer compaction at increased NaCl and $CaCl_2$ concentrations.

Chapter 4 investigated the role of shape on the attachment efficiency of PS particles. Results from Chapter 4 indicate that the attachment of colloidal particles onto NOM-coated surfaces can be greatly affected by the shape of the particles, depending on ionic strength and the type of NOM coating. In the presence of the alginate surface, the attachment of both spherical and stretched PS qualitatively agreed with DLVO theory. In the presence of the HHA surface, however, deviations from DLVO theory were observed. At low ionic strengths, spherical PS attached to HHA at a much higher rate than stretched PS. This deviation from DLVO theory can be explained by the increased surface heterogeneity and roughness of the HHA surface observed by AFM. More voids present in the HHA layer allows for a higher potential of spherical PS particle entanglement, while the enlarged major axis of the stretched particles hinder their ability to become entangled in the extended HHA surface. As ionic strength increases, the HHA layer condenses and the potential for spherical particle entanglement is reduced. At high ionic strengths, the HHA layer condenses to a point where DLVO forces dominate and the stretched particles attach at a higher rate than spherical particles, due to a reduced energy barrier to deposition.

Chapter 5 incorporated all the data from Chapters 2, 3, and 4 along with attachment efficiency data amassed from literature to empirically model the attachment efficiency as an explicit function of 13 identified physicochemical characteristics of the particle and depositional system. The observed model performance (Figures 5.3 and 5.4) indicates that prediction of the attachment efficiency database was well captured by the machine learning model applied and the 13 physicochemical characteristics selected. Holdout prediction results (Table 5.2) demonstrate that the relationship between attachment efficiency (i.e., target feature) and the physicochemical state (i.e., training features) is complex and relies on all 13 physicochemical features selected. The physicochemical features reported as most important to the accurate prediction of attachment efficiency (Figure 5.7) are in agreement with previous studies and the features reported as less important are either somewhat redundant (salt type) or have been previously shown to only affect attachment efficiency under

certain conditions (temperature). In summary, the intended utility of the work presented in Chapter 5 is threefold by:

(i) providing an accurate, quantitative prediction of attachment efficiency based explicitly on physicochemical characteristics;

(ii) directing future mechanistic modeling efforts towards the physicochemical characterstics most critical to prediction of attachment efficiency; and

(iii) guiding future experiments as to which characteristics are most important to measure and report in order to maximize the scientific benefit of results.

The work presented in Chapters 2, 3, and 4 indicate that the presence of SOM layers can greatly affect the attachment efficiency of colloidal particles. Depending on the type of SOM (Chapters 2 and 5), ionic strength of solution (Chapter 3), and particle shape (Chapter 4), attachment efficiency can be hindered, enhanced, or remain unchanged. These findings clearly suggest that SOM layers, which are ubiquitous in the subsurface environment, will play a major role in the deposition processes of colloidal particles and therefore may influence their transport. Fully understanding the transport contributions of SOM layers may prove crucial to predicting the fate and transport of colloidal particles through the subsurface environment and, in turn, their eventual impact on the environment. Combined with the predictive model presented in Chapter 5, these results indicate that the physicochemical characteristics of the system alter attachment efficiency through many, complex pathways.

In summary, the work presented in this dissertation indicates that attachment efficiency is influenced by many physicochemical features and describing this relationship is too complex for a single study, or series of studies, alone. Only through a compilation of attachment experiments, both contained within this dissertation and amassed from recent publications, were we able to predict attachment efficiency based explicitly on physicochemical features with relative accuracy. The results presented in Chapter 5 should prove encouraging to the field of environmental science, however. It illustrates that if we can combine high

quality transport data from many sources with advanced machine learning techniques, we can make progress towards an all encompassing understanding of transport, allowing us to make impactful, risk-informed decisions in the present day, before we fully understand the theory and mechanisms driving environmental transport.

6.2 Future Work

The work presented in this dissertation has improved the understanding of how ionic strength, particle shape, and the presence of attached SOM affect the attachment efficiency of colloidal particles. Though these improvements certainly aid in our mechanistic understanding of attachment, studying one factor alone is not enough to result in a true, impactful advancement of transport knowledge. Only through the compilation of all of our work and all recently published similar work were we able to create a database with sufficient complexity to predict attachment efficiency with acceptable accuracy. Though the model presented in Chapter 5 predicts attachment efficiency for a wide range of physicochemical characteristics, it is only applicable for the range of values available in current literature, and therefore included in the database. As additional data is published investigating physicochemical characteristics outside of this range, the database will need to be updated and the model retrained. Only through this iterative process can we hope to produce a model robust enough to predict attachment efficiency in real, environmental conditions. Furthermore, the database created in Chapter 5 should be used as a guide for future attachment efficiency experiments. By utilizing the database, scientists can identify any gaps that need to be filled or relevant characteristics which have not yet been explored.

In this same manner, similar steps should be taken to improve the understanding of all aspects of particle transport. Only through compilation of data in coordination with advanced modeling techniques can we make progress towards an all encompassing understanding of particle transport. In short, we need to close the gaps between experimental understanding and quantitative predictive modeling, in order to maximize the benefit of the high quality transport data being reported on a regular basis. Not only will the future of predictive modeling benefit from a comprehensive database, but so will the future of experimental transport science. A database will inform experimental scientists which areas are lacking so that they can focus their efforts accordingly, improving the efficiency of transport research. The improved predictive models which arise from such databases will

also help identify which characteristics are crucial to predicting transport, informing the experimental scientist exactly which characteristics to measure and report. Only through this kind of closed loop can we hope to accurately predict particle transport in a system as complex as the natural environment.

BIBLIOGRAPHY

[1] A. McWilliams. Nanotechnology: A realistic market assessment, 2014. URL http://www.bccresearch.com/market-research/nanotechnology/nanotechnology-market-assessment-report-nan031f.html.

[2] M.S. Mauter and M. Elimelech. Environmental applications of carbon-based nanomaterials. *Environmental Science & Technology*, 42(16):5843–5859, 2008.

[3] A. Nel, T. Xia, L. Madler, and N. Li. Toxic potential of materials at the nanolevel. *Science*, 311(5761):622–627, 2006.

[4] S. Bosi, T. Da Ros, G. Spalluto, and M. Prato. Fullerene derivatives: an attractive tool for biological applications. *European Journal of Medicinal Chemistry*, 38(11-12):913–923, 2003.

[5] Philippe Poncharal, Z.L. Wang, Daniel Ugarte, and Walt A. De Heer. Electrostatic deflections and electromechanical resonances of carbon nanotubes. *Science*, 283 (5407):1513–1516, 1999.

[6] Jonathan Loeffler, Ulrih Sutter, Rgeine Hedderich, et al. Overview on promising nanomaterials for industrial applications. *Nanomaterial Roadmap*, 2015.

[7] Zhifeng Long, Jing Ji, Kun Yang, Daohui Lin, and Fengchang Wu. Systematic and quantitative investigation of the mechanism of carbon nanotubes? toxicity toward algae. *Environmental Science & Technology*, 46(15):8458–8466, 2012.

[8] Delina Y. Lyon, Lena Brunet, George W. Hinkal, Mark R. Wiesner, and Pedro J.J. Alvarez. Antibacterial activity of fullerene water suspensions (nc_{60}) is not due to ros-mediated damage. *Nano letters*, 8(5):1539–1543, 2008.

[9] J.P. Kamat, T.P.A. Devasagayam, K.I. Priyadarsini, and H. Mohan. Reactive oxygen species mediated membrane damage induced by fullerene derivatives and its possible biological implications. *Toxicology*, 155(1):55–61, 2000.

[10] N. Nakajima, C. Nishi, F.M. Li, and Y. Ikada. Photo-induced cytotoxicity of water-soluble fullerene. *Fullerene Science and Technology*, 4(1):1–19, 1996.

[11] W.J. Weber, E.J. LeBoeuf, T.M. Young, and W.L. Huang. Contaminant interactions with geosorbent organic matter: Insights drawn from polymer sciences. *Water Research*, 35(4):853–868, 2001.

[12] Baoshan Xing, William B. McGill, and Marvin J. Dudas. Cross-correlation of polarity curves to predict partition coefficients of nonionic organic contaminants. *Environmental Science & Technology*, 28(11):1929–1933, 1994.

[13] Xilong Wang and Baoshan Xing. Sorption of organic contaminants by biopolymer-derived chars. *Environmental Science & Technology*, 41(24):8342–8348, 2007.

[14] F.J. Stevenson. *Humus chemistry : genesis, composition, reactions*. Wiley, New York, 2nd edition, 1994.

[15] R. Sutton and G. Sposito. Molecular structure in soil humic substances: the new view. *Environmental Science & Technology*, 39(23):9009–9015, 2005.

[16] Rossane C. DeLapp and Eugene J. LeBoeuf. Thermal analysis of whole soils and sediment. *Journal of Environmental Quality*, 33(1):330–337, 2004.

[17] Rossane C. DeLapp, Eugene J. LeBoeuf, and Katherine D. Bell. Thermodynamic properties of several soil-and sediment-derived natural organic materials. *Chemosphere*, 54(4):527–539, 2004.

[18] Eugene J. LeBoeuf and Walter J. Weber. Macromolecular characteristics of natural organic matter. 2. sorption and desorption behavior. *Environmental Science & Technology*, 34(17):3632–3640, 2000.

[19] Eugene J. LeBoeuf and Walter J. Weber. Macromolecular characteristics of natural organic matter. 1. insights from glass transition and enthalpic relaxation behavior. *Environmental Science & Technology*, 34(17):3623–3631, 2000.

[20] Gabriele E. Schaumann and Olivia Antelmann. Thermal characteristics of soil organic matter measured by dsc: A hint on a glass transition. *Journal of Plant Nutrition and Soil Science*, 163(2):179–181, 2000.

[21] Katherine D. Young and Eugene J. LeBoeuf. Glass transition behavior in a peat humic acid and an aquatic fulvic acid. *Environmental Science & Technology*, 34 (21):4549–4553, 2000.

[22] E.J. LeBoeuf and W.J. Weber. A distributed reactivity model for sorption by soils and sediments .8. sorbent organic domains: Discovery of a humic acid glass transition and an argument for a polymer-based model. *Environmental Science & Technology*, 31(6):1697–1702, 1997.

[23] Lucy M. Lucht, John M. Larson, and Nikolaos A. Peppas. Macromolecular structure of coals. 9. molecular structure and glass transition temperature. *Energy & Fuels*, 1 (1):56–58, 1987.

[24] Lu Zhang, Eugene J. LeBoeuf, and Baoshan Xing. Thermal analytical investigation of biopolymers and humic-and carbonaceous-based soil and sediment organic matter. *Environmental Science & Technology*, 41(14):4888–4894, 2007.

[25] E.J. LeBoeuf. *Macromolecular characteristics of natural organic matter and their influence on sorption and desorption behavior of organic chemicals*. University of Michigan, 1998.

[26] Weilin Huang and Walter J. Weber. A distributed reactivity model for sorption by soils and sediments. 11. slow concentration-dependent sorption rates. *Environmental Science & Technology*, 32(22):3549–3555, 1998.

[27] Thomas M. Young and Walter J. Weber. A distributed reactivity model for sorption by soils and sediments. 3. effects of diagenetic processes on sorption energetics. *Environmental Science & Technology*, 29(1):92–97, 1995.

[28] H.B. Hopfenberg and V. Stannett. The diffusion and sorption of gases and vapours in glassy polymers. In *The Physics of Glassy Polymers*, pages 504–547. Springer, 1973.

[29] G.E. Schaumann and E.J. LeBoeuf. Glass transitions in peat: their relevance and the impact of water. *Environmental science & technology*, 39(3):800–806, 2005.

[30] V.R.N. Telis and P.J.A. Sobral. Glass transitions and state diagram for freeze-dried pineapple. *LWT-Food Science and Technology*, 34(4):199–205, 2001.

[31] D. Benczedi, I. Tomka, and F. Escher. Thermodynamics of amorphous starch-water systems. 2. concentration fluctuations. *Macromolecules*, 31(9):3062–3074, 1998.

[32] G.E. Schaumann. Matrix relaxation and change of water state during hydration of peat. *Colloids and Surfaces A: Physicochemical and Engineering Aspects*, 265(1): 163–170, 2005.

[33] Adélia J.A. Aquino, Daniel Tunega, Gabriele E. Schaumann, Georg Haberhauer, Martin H. Gerzabek, and Hans Lischka. Stabilizing capacity of water bridges in nanopore segments of humic substances: a theoretical investigation. *The Journal of Physical Chemistry C*, 113(37):16468–16475, 2009.

[34] E.R. Graber, L. Tsechansky, and M. Borisover. Hydration-assisted sorption of a

probe organic compound at different peat hydration levels: the link solvation model. *Environmental science & technology*, 41(2):547–554, 2007.

[35] M. Borisover and E.R. Graber. Relationship between strength of organic sorbate interactions in nom and hydration effect on sorption. *Environmental science & technology*, 36(21):4570–4577, 2002.

[36] M. Borisover, M. Reddy, and E.R. Graber. Solvation effect on organic compound interactions in soil organic matter. *Environmental science & technology*, 35(12): 2518–2524, 2001.

[37] E.R. Graber and M. Borisover. Hydration-facilitated sorption of specifically interacting organic compounds by model soil organic matter. *Environmental science & technology*, 32(2):258–263, 1998.

[38] A.G. Kalinichev and R.J. Kirkpatrick. Molecular dynamics simulation of cationic complexation with natural organic matter. *European Journal of Soil Science*, 58(4): 909–917, 2007.

[39] Coy P. McNew and Eugene J. LeBoeuf. The role of attached phase soil and sediment organic matter physicochemical properties on fullerene (nc_{60}) attachment. *Chemosphere*, 139:609–616, 2015.

[40] Yamuna Kunhi Mouvenchery, Jiří Kučerík, Doerte Diehl, and Gabriele E. Schaumann. Cation-mediated cross-linking in natural organic matter: a review. *Reviews in Environmental Science and Biotechnology*, 11(1):41–54, 2012.

[41] Adélia J.A. Aquino, Daniel Tunega, Gabriele E. Schaumann, Georg Haberhauer, Martin H. Gerzabek, and Hans Lischka. The functionality of cation bridges for binding polar groups in soil aggregates. *International Journal of Quantum Chemistry*, 111(7-8):1531–1542, 2011.

[42] R. Kelman Wieder. Metal cation binding to sphagnum peat and sawdust: Relation to wetland treatment of metal-polluted waters. *Water, Air, and Soil Pollution*, 53(3-4): 391–400, 1990.

[43] G.E. Schaumann and S. Thiele-Bruhn. Molecular modeling of soil organic matter: Squaring the circle? *Geoderma*, (169):e1, 2011.

[44] Yuefeng Lu and Joseph J. Pignatello. Sorption of apolar aromatic compounds to soil humic acid particles affected by aluminum (iii) ion cross-linking. *Journal of Environmental Quality*, 33(4):1314–1321, 2004.

[45] G.E. Schaumann and M. Bertmer. Do water molecules bridge soil organic matter molecule segments? *European Journal of Soil Science*, 59(3):423–429, 2008.

[46] Gabriele E. Schaumann, Daniela Gildemeister, Yamuna Kunhi Mouvenchery, Sandra Spielvogel, and Dörte Diehl. Interactions between cations and water molecule bridges in soil organic matter. *Journal of Soils and Sediments*, 13(9):1579–1588, 2013.

[47] Saikat Ghosh, Hamid Mashayekhi, Prasanta Bhowmik, and Baoshan Xing. Colloidal stability of al2o3 nanoparticles as affected by coating of structurally different humic acids. *Langmuir*, 26(2):873–879, 2009.

[48] Bin Xie, Zhihua Xu, Wenhua Guo, and Qilin Li. Impact of natural organic matter on the physicochemical properties of aqueous c60 nanoparticles. *Environmental Science & Technology*, 42(8):2853–2859, 2008.

[49] Daohui Lin and Baoshan Xing. Tannic acid adsorption and its role for stabilizing carbon nanotube suspensions. *Environmental Science & Technology*, 42(16):5917–5923, 2008.

[50] K.L. Chen and M. Elimelech. Influence of humic acid on the aggregation kinetics of fullerene (c_60) nanoparticles in monovalent and divalent electrolyte solutions. *Journal of Colloid and Interface Science*, 309(1):126–134, 2007.

[51] Motoki Terashima and Seiya Nagao. Solubilization of [60] fullerene in water by aquatic humic substances. *Chemistry Letters*, 36(2):302–303, 2007.

[52] Hoon Hyung, John D. Fortner, Joseph B. Hughes, and Jae-Hong Kim. Natural organic matter stabilizes carbon nanotubes in the aqueous phase. *Environmental Science & Technology*, 41(1):179–184, 2007.

[53] Daohui Lin, Ni Liu, Kun Yang, Lizhong Zhu, Yong Xu, and Baoshan Xing. The effect of ionic strength and ph on the stability of tannic acid-facilitated carbon nanotube suspensions. *Carbon*, 47(12):2875–2882, 2009.

[54] Xin Ma and Dermont Bouchard. Formation of aqueous suspensions of fullerenes. *Environmental Science & Technology*, 43(2):330–336, 2008.

[55] Y. Thomas He, Jiamin Wan, and Tetsu Tokunaga. Kinetic stability of hematite nanoparticles: the effect of particle sizes. *Journal of Nanoparticle Research*, 10 (2):321–332, 2008.

[56] D. Lin, X. Tian, F. Wu, and B. Xing. Fate and transport of engineered nanomaterials in the environment. *Journal of Environmental Quality*, 39(6):1896–1908, 2010.

[57] Mohammed Baalousha, Adriana Manciulea, Susan Cumberland, Kevin Kendall, and Jamie R. Lead. Aggregation and surface properties of iron oxide nanoparticles: influence of ph and natural organic matter. *Environmental Toxicology and Chemistry*, 27(9):1875–1882, 2008.

[58] EJW Verwey. Theory of the stability of lyophobic colloids. *The Journal of Physical Chemistry*, 51(3):631–636, 1947.

[59] BV Derjaguin. Theory of the stability of strongly charged lyophobic sols and the adhesion of strongly charged particles in solutions of electrolytes. *Acta Physicochim. USSR*, 14:633–662, 1941.

[60] Menachem Elimelech, Xiadong Jia, John Gregory, and Richard Williams. *Particle deposition & aggregation: measurement, modelling and simulation*. Butterworth-Heinemann, 1998.

[61] K.L. Chen and M. Elimelech. Aggregation and deposition kinetics of fullerene (c-60) nanoparticles. *Langmuir*, 22(26):10994–11001, 2006.

[62] Navid B. Saleh, Lisa D. Pfefferle, and Menachem Elimelech. Aggregation kinetics of multiwalled carbon nanotubes in aquatic systems: measurements and environmental implications. *Environmental Science & Technology*, 42(21):7963–7969, 2008.

[63] Xiaojun Chang and Dermont C. Bouchard. Multiwalled carbon nanotube deposition on model environmental surfaces. *Environmental Science & Technology*, 47(18): 10372–10380, 2013.

[64] X.L. Qu, P.J.J. Alvarez, and Q.L. Li. Impact of sunlight and humic acid on the deposition kinetics of aqueous fullerene nanoparticles (nc(60)). *Environmental Science & Technology*, 46(24):13455–13462, 2012.

[65] Peng Yi and Kai Loon Chen. Influence of surface oxidation on the aggregation and deposition kinetics of multiwalled carbon nanotubes in monovalent and divalent electrolytes. *Langmuir*, 27(7):3588–3599, 2011.

[66] K.L. Chen and M. Elimelech. Interaction of fullerene (c-60) nanoparticles with humic acid and alginate coated silica surfaces: Measurements, mechanisms, and environmental implications. *Environmental Science & Technology*, 42(20):7607–7614, 2008.

[67] Benjamin Espinasse, Ernest M. Hotze, and Mark R. Wiesner. Transport and retention of colloidal aggregates of c60 in porous media: Effects of organic macromolecules, ionic composition, and preparation method. *Environmental Science & Technology*, 41(21):7396–7402, 2007.

[68] C. Degueldre, H.R. Pfeiffer, W. Alexander, B. Wernli, and R. Bruetsch. Colloid properties in granitic groundwater systems. i: Sampling and characterisation. *Applied Geochemistry*, 11(5):677–695, 1996.

[69] Peter Hirsch and Ellen Rades-Rohkohl. Microbial colonization of aquifer sediment exposed in a groundwater well in northern germany. *Applied and Environmental Microbiology*, 56(10):2963–2966, 1990.

[70] D.L. Balkwill, J.K. Fredrickson, and J.M. Thomas. Vertical and horizontal variations in the physiological diversity of the aerobic chemoheterotrophic bacterial microflora in deep southeast coastal plain subsurface sediments. *Applied and Environmental Microbiology*, 55(5):1058–1065, 1989.

[71] Megan B. Seymour, Gexin Chen, Chunming Su, and Yusong Li. Transport and retention of colloids in porous media: does shape really matter? *Environmental Science & Technology*, 47(15):8391–8398, 2013.

[72] Ruth E. Baltus, Appala Raju Badireddy, Wendong Xu, and Shankararaman Chellam. Analysis of configurational effects on hindered convection of nonspherical bacteria and viruses across microfiltration membranes. *Industrial & Engineering Chemistry Research*, 48(5):2404–2413, 2008.

[73] Yonggang Wang, Yusong Li, John D Fortner, Joseph B Hughes, Linda M Abriola, and Kurt D Pennell. Transport and retention of nanoscale c60 aggregates in water-saturated porous media. *Environmental science & technology*, 42(10):3588–3594, 2008.

[74] Michael B. Salerno, Matt Flamm, Bruce E. Logan, and Darrell Velegol. Transport of rodlike colloids through packed beds. *Environmental Science & Technology*, 40 (20):6336–6340, 2006.

[75] Thomas H. Weiss, Aaron L. Mills, George M. Hornberger, and Janet S. Herman. Effect of bacterial cell shape on transport of bacteria in porous media. *Environmental Science & Technology*, 29(7):1737–1740, 1995.

[76] Jack F Schijven, S Majid Hassanizadeh, and Ria HAM de Bruin. Two-site kinetic modeling of bacteriophages transport through columns of saturated dune sand. *Journal of Contaminant Hydrology*, 57(3):259–279, 2002.

[77] Scott A Bradford, Jirka Simunek, Mehdi Bettahar, Martinus Th van Genuchten, and Scott R Yates. Modeling colloid attachment, straining, and exclusion in saturated porous media. *Environmental Science & Technology*, 37(10):2242–2250, 2003.

[78] Nathalie Tufenkji and Menachem Elimelech. Spatial distributions of cryptosporidium oocysts in porous media: Evidence for dual mode deposition. *Environmental Science & Technology*, 39(10):3620–3629, 2005.

[79] Eli Goldberg, Martin Scheringer, Thomas D Bucheli, and Konrad Hungerbühler. Critical assessment of models for transport of engineered nanoparticles in saturated porous media. *Environmental Science & Technology*, 48(21):12732–12741, 2014.

[80] Indranil Chowdhury, Matthew C. Duch, Nikhita D. Mansukhani, Mark C. Hersam, and Dermont Bouchard. Interactions of graphene oxide nanomaterials with natural organic matter and metal oxide surfaces. *Environmental Science & Technology*, 48 (16):9382–9390, 2014.

[81] Coy P. McNew and Eugene J. LeBoeuf. nc_{60} deposition onto a humic acid coated silica surface and the effect of ionic strength. *Manuscript submitted for publication*, 2015.

[82] Coy P. McNew, Negin Kananizadeh, Yusong Li, and Eugene J. LeBoeuf. The attachment of colloidal particles to environmentally relevant surfaces and the effect of particle shape. *Manuscript in preparation*, 2015.

[83] Christopher M Bishop. *Pattern Recognition and Machine Learning*. springer, 2006.

[84] Li Deng, Geoffrey Hinton, and Brian Kingsbury. New types of deep neural network learning for speech recognition and related applications: An overview. In *Acoustics, Speech and Signal Processing (ICASSP), 2013 IEEE International Conference on*, pages 8599–8603. IEEE, 2013.

[85] David Stavens and Sebastian Thrun. A self-supervised terrain roughness estimator for off-road autonomous driving. *arXiv preprint arXiv:1206.6872*, 2012.

[86] Gary Bradski and Adrian Kaehler. *Learning OpenCV: Computer vision with the OpenCV library*. " O'Reilly Media, Inc.", 2008.

[87] Travis B Murdoch and Allan S Detsky. The inevitable application of big data to health care. *Jama*, 309(13):1351–1352, 2013.

[88] Jeremy M Gernand, Elizabeth Casman, et al. Machine learning for nanomaterial toxicity risk assessment. *Intelligent Systems, IEEE*, 29(3):84–88, 2014.

[89] DA Winkler, FR Burden, Bing Yan, Ralph Weissleder, Carlos Tassa, Stanley Shaw, and VC Epa. Modelling and predicting the biological effects of nanomaterials. *SAR and QSAR in Environmental Research*, 25(2):161–172, 2014.

[90] Eli Goldberg, Martin Scheringer, Thomas D Bucheli, and Konrad Hungerbühler. Prediction of nanoparticle transport behavior from physicochemical properties: machine learning provides insights to guide the next generation of transport models. *Environmental Science: Nano*, 2(4):352–360, 2015.

[91] Archana Jaiswall. Qcm-d basic training: Introduction and applications. QCM-D Training Course, 2013.

[92] Matthew C Dixon. Quartz crystal microbalance with dissipation monitoring: enabling real-time characterization of biological materials and their interactions. *Journal of Biomolecular Techniques*, 19(3):151, 2008.

[93] G. Sauerbrey. Verwendung von schwingquarzen zur wagung dunner schichten und zur mikrowagung. *Z. Phys*, 155:206–222, 1959.

[94] Ilya Reviakine, Diethelm Johannsmann, and Ralf P Richter. Hearing what you cannot see and visualizing what you hear: interpreting quartz crystal microbalance data from solvated interfaces. *Analytical chemistry*, 83(23):8838–8848, 2011.

[95] M.V. Voinova, M. Rodahl, M. Jonson, and B. Kasemo. Viscoelastic acoustic response of layered polymer films at fluid-solid interfaces: continuum mechanics approach. *Physica Scripta*, 59(5):391, 1999.

[96] Kristian Rechendorff, Mads Bruun Hovgaard, Morten Foss, and Flemming Besenbacher. Influence of surface roughness on quartz crystal microbalance measurements in liquids. *Journal of Applied Physics*, 101(11):114502, 2007.

[97] Lubica Macakova, Eva Blomberg, and Per M Claesson. Effect of adsorbed layer surface roughness on the qcm-d response: focus on trapped water. *Langmuir*, 23 (24):12436–12444, 2007.

[98] Chad T Jafvert and Pradnya P Kulkarni. Buckminsterfullerene's (c60) octanol- water partition coefficient (kow) and aqueous solubility. *Environmental science & technology*, 42(16):5945–5950, 2008.

[99] D.Y. Lyon, L.K. Adams, J.C. Falkner, and P.J.J. Alvarez. Antibacterial activity of

fullerene water suspensions: Effects of preparation method and particle size. *Environmental Science & Technology*, 40(14):4360–4366, 2006.

[100] Y. Lu, K. Yang, and D. Lin. Transport of surfactant-facilitated multiwalled carbon nanotube suspensions in columns packed with sized soil particles. *Environmental Pollution*, 192:36–43, 2014.

[101] R.C. DeLapp, E.J. LeBoeuf, J. Chen, and B.H. Gu. Advanced thermal characterization of fractionated natural organic matter. *Journal of Environmental Quality*, 34(3): 842–853, 2005.

[102] G.V. Andrievsky, M.V. Kosevich, O.M. Vovk, V.S. Shelkovsky, and L.A. Vashchenko. On the production of an aqueous colloidal solution of fullerenes. *Journal of the Chemical Society-Chemical Communications*, (12):1281–1282, 1995.

[103] R. Hogg, T.W. Healy, and D.W. Fuerstenau. Mutual coagulation of colloidal dispersions. *Transactions of the Faraday Society*, 62:1638–1651, 1966.

[104] X. Jiang, M. Tong, H. Li, and K. Yang. Deposition kinetics of zinc oxide nanoparticles on natural organic matter coated silica surfaces. *Journal of colloid and interface science*, 350(2):427–434, 2010.

[105] C.G. Malmberg and A.A. Maryott. Dielectric constant of water from 0 to 100 °c. *Journal of Research of the National Bureau of Standards*, 56(1):1–8, 1956.

[106] N. Ishida and S. Biggs. Direct observation of the phase transition for a poly(n-isopropylacryamide) layer grafted onto a solid surface by afm and qcm-d. *Langmuir*, 23(22):11083–11088, 2007.

[107] A. Vidyasagar, C. Sung, R. Gamble, and J.L. Lutkenhaus. Thermal transitions in dry and hydrated layer-by-layer assemblies exhibiting linear and exponential growth. *ACS Nano*, 6(7):6174–6184, 2012.

[108] Fadri Gottschalk and Bernd Nowack. The release of engineered nanomaterials to the environment. *Journal of Environmental Monitoring*, 13(5):1145–1155, 2011.

[109] Jiasong Fang, Delina Y Lyon, Mark R Wiesner, Jinping Dong, and Pedro JJ Alvarez. Effect of a fullerene water suspension on bacterial phospholipids and membrane phase behavior. *Environmental science & technology*, 41(7):2636–2642, 2007.

[110] Jonathan Brant, Helene Lecoanet, and Mark R Wiesner. Aggregation and deposition characteristics of fullerene nanoparticles in aqueous systems. *Journal of Nanoparticle Research*, 7(4-5):545–553, 2005.

[111] Yonggang Wang, Yusong Li, and Kurt D Pennell. Influence of electrolyte species and concentration on the aggregation and transport of fullerene nanoparticles in quartz sands. *Environmental toxicology and chemistry*, 27(9):1860–1867, 2008.

[112] Yusong Li, Yonggang Wang, Kurt D Pennell, and Linda M Abriola. Investigation of the transport and deposition of fullerene (c60) nanoparticles in quartz sands under varying flow conditions. *Environmental science & technology*, 42(19):7174–7180, 2008.

[113] Hélène F Lecoanet, Jean-Yves Bottero, and Mark R Wiesner. Laboratory assessment of the mobility of nanomaterials in porous media. *Environmental science & technology*, 38(19):5164–5169, 2004.

[114] Robert J Hunter. *Zeta potential in colloid science: principles and applications*. Academic press, 2013.

[115] Luc Bousse, Shahriar Mostarshed, Bart Van Der Shoot, NF De Rooij, Peter Gimmel, and Wolfgang Göpel. Zeta potential measurements of ta_2o_5 and sio_2 thin films. *Journal of colloid and interface science*, 147(1):22–32, 1991.

[116] Baoling Yuan, Mai Pham, and Thanh H Nguyen. Deposition kinetics of bacteriophage ms2 on a silica surface coated with natural organic matter in a radial stagnation point flow cell. *Environmental science & technology*, 42(20):7628–7633, 2008.

[117] Seungkwan Hong and Menachem Elimelech. Chemical and physical aspects of natural organic matter (nom) fouling of nanofiltration membranes. *Journal of membrane science*, 132(2):159–181, 1997.

[118] Kai Loon Chen, Steven E Mylon, and Menachem Elimelech. Aggregation kinetics of alginate-coated hematite nanoparticles in monovalent and divalent electrolytes. *Environmental science & technology*, 40(5):1516–1523, 2006.

[119] C.H. Ward, W. Giger, and P.L. McCarty. *Groundwater Quality (Environmental Science and Technology Series)*. John Wiley & Sons Inc, 1985. ISBN 0471815977.

[120] Yingying Wang, Frederik Hammes, Marcel Du?ggelin, and Thomas Egli. Influence of size, shape, and flexibility on bacterial passage through micropore membrane filters. *Environmental Science & Technology*, 42(17):6749–6754, 2008.

[121] Indranil Chowdhury, Matthew C. Duch, Nikhita D. Mansukhani, Mark C. Hersam, and Dermont Bouchard. Deposition and release of graphene oxide nanomaterials using a quartz crystal microbalance. *Environmental Science & Technology*, 48(2): 961–969, 2014.

[122] Yun Shen, Hyunjung Kim, Meiping Tong, and Qingyun Li. Influence of solution chemistry on the deposition and detachment kinetics of rna on silica surfaces. *Colloids and Surfaces B: Biointerfaces*, 82(2):443–449, 2011.

[123] Nelson Akaighe, Sean W. Depner, Sarbajit Banerjee, and Mary Sohn. Transport and deposition of suwannee river humic acid/natural organic matter formed silver nanoparticles on silica matrices: The influence of solution ph and ionic strength. *Chemosphere*, 92(4):406–412, 2013.

[124] Beng Joo Reginald Thio, Dongxu Zhou, and Arturo A. Keller. Influence of natural organic matter on the aggregation and deposition of titanium dioxide nanoparticles. *Journal of Hazardous Materials*, 189(1):556–563, 2011.

[125] Meiping Tong, Jiali Ding, Yun Shen, and Pingting Zhu. Influence of biofilm on the transport of fullerene (c 60) nanoparticles in porous media. *Water Research*, 44(4): 1094–1103, 2010.

[126] Julie A. Champion, Yogesh K. Katare, and Samir Mitragotri. Making polymeric micro-and nanoparticles of complex shapes. *Proceedings of the National Academy of Sciences*, 104(29):11901–11904, 2007.

[127] Qiang Liu, Volha Lazouskaya, Qingxiang He, and Yan Jin. Effect of particle shape on colloid retention and release in saturated porous media. *Journal of Environmental Quality*, 39(2):500–508, 2010.

[128] C.C. Ho and R.H. Ottewill. Investigation of the charge distribution of ellipsoidal particles. *Colloids and Surfaces A: Physicochemical and Engineering Aspects*, 141 (1):29–35, 1998.

[129] C.C. Ho, R.H. Ottewill, and L. Yu. Examination of ellipsoidal polystyrene particles by electrophoresis. *Langmuir*, 13(7):1925–1930, 1997.

[130] Eli Goldberg, Coy P. McNew, Martin Scheringer, Eugene J. LeBoeuf, and Konrad Hungerbuühler. Predicting particle attachment efficiency from physicochemical characteristics: a machine learning approach. *Manuscript in Preparation*.

[131] Barbara Karn, Todd Kuiken, and Martha Otto. Nanotechnology and in situ remediation: a review of the benefits and potential risks. *Environmental health perspectives*, pages 1823–1831, 2009.

[132] Bhupinder Singh Sekhon. Nanotechnology in agri-food production: an overview. *Nanotechnology, science and applications*, 7:31, 2014.

[133] Vandana Ghormade, Mukund V Deshpande, and Kishore M Paknikar. Perspectives for nano-biotechnology enabled protection and nutrition of plants. *Biotechnology advances*, 29(6):792–803, 2011.

[134] Frank Von der Kammer, P Lee Ferguson, Patricia A Holden, Armand Masion, Kim R Rogers, Stephen J Klaine, Albert A Koelmans, Nina Horne, and Jason M Unrine. Analysis of engineered nanomaterials in complex matrices (environment and biota): general considerations and conceptual case studies. *Environmental Toxicology and Chemistry*, 31(1):32–49, 2012.

[135] Steven Sleutel, Veerle Cnudde, Bert Masschaele, J Vlassenbroek, Manuel Dierick, Luc Van Hoorebeke, Patric Jacobs, and Stefaan De Neve. Comparison of different nano-and micro-focus x-ray computed tomography set-ups for the visualization of the soil microstructure and soil organic matter. *Computers & Geosciences*, 34 (8):931–938, 2008.

[136] Tanapon Phenrat, Hye-Jin Kim, Fritjof Fagerlund, Tissa Illangasekare, and Gregory V. Lowry. Empirical correlations to estimate agglomerate size and deposition during injection of a polyelectrolyte-modified fe 0 nanoparticle at high particle concentration in saturated sand. *Journal of Contaminant Hydrology*, 118(3):152–164, 2010.

[137] Tanapon Phenrat, Jee Eun Song, Charlotte M. Cisneros, Daniel P. Schoenfelder, Robert D. Tilton, and Gregory V. Lowry. Estimating attachment of nano-and submicrometer-particles coated with organic macromolecules in porous media: development of an empirical model. *Environmental Science & Technology*, 44(12): 4531–4538, 2010.

[138] Renbi Bai and Chi Tien. Particle deposition under unfavorable surface interactions. *Journal of Colloid and Interface Science*, 218(2):488–499, 1999.

[139] Renbi Bai and Chi Tien. A new correlation for the initial filter coefficient under unfavorable surface interactions. *Journal of Colloid and Interface Science*, 179(2): 631–634, 1996.

[140] Menachem Elimelech. Predicting collision efficiencies of colloidal particles in porous media. *Water Research*, 26(1):1–8, 1992.

[141] Eli Goldberg and Coy P. McNew. Particle attachment efficiency database live figure, 2015. URL http://bl.ocks.org/mcnewcp/raw/3028811a3f6582c255ad/.

[142] Fabian Pedregosa, Gaël Varoquaux, Alexandre Gramfort, Vincent Michel, Bertrand Thirion, Olivier Grisel, Mathieu Blondel, Peter Prettenhofer, Ron Weiss, Vincent Dubourg, et al. Scikit-learn: Machine learning in python. *The Journal of Machine Learning Research*, 12:2825–2830, 2011.

[143] R Allan Freeze and John A Cherry. *Groundwater*. Prentice-Hall, 1977.

Appendix A

Details on Materials Characterization

A.1 Harpeth humic and fulvic acid characterization details

Table A.1: Elemental analysis and water content of HHA and HFA after DeLapp et al. [101], reproduced here with permission from the author.

NOM	C (mass %)	H (mass %)	O (mass %)	N (mass %)	S (mass %)	P (mass %)	Water Content (mass %)
Harpeth Humic Acid	51.2	4.9	39.1	4.0	0.56	0.12	5.8
Harpeth Fulvic Acid	43.4	3.4	49.4	1.5	0.20	0.75	5.2

Table A.2: Relative abundance of functional groups by ^{13}C nuclear magnetic resonance (NMR) analysis of HHA and HFA after DeLapp et al. [101], reproduced here with permission from the author.

NOM	Alkyl 0-50 (ppm)	O-Alkyl 50-112 (ppm)	Aromatic 112-145 (ppm)	Phenolic 145-163 (ppm)	Carboxyl 163-190 (ppm)
Harpeth Humic Acid	0.2	0.28	0.22	0.13	0.18
Harpeth Fulvic Acid	0.15	0.29	0.19	0.18	0.20

A.2 nC_{60} characterization details

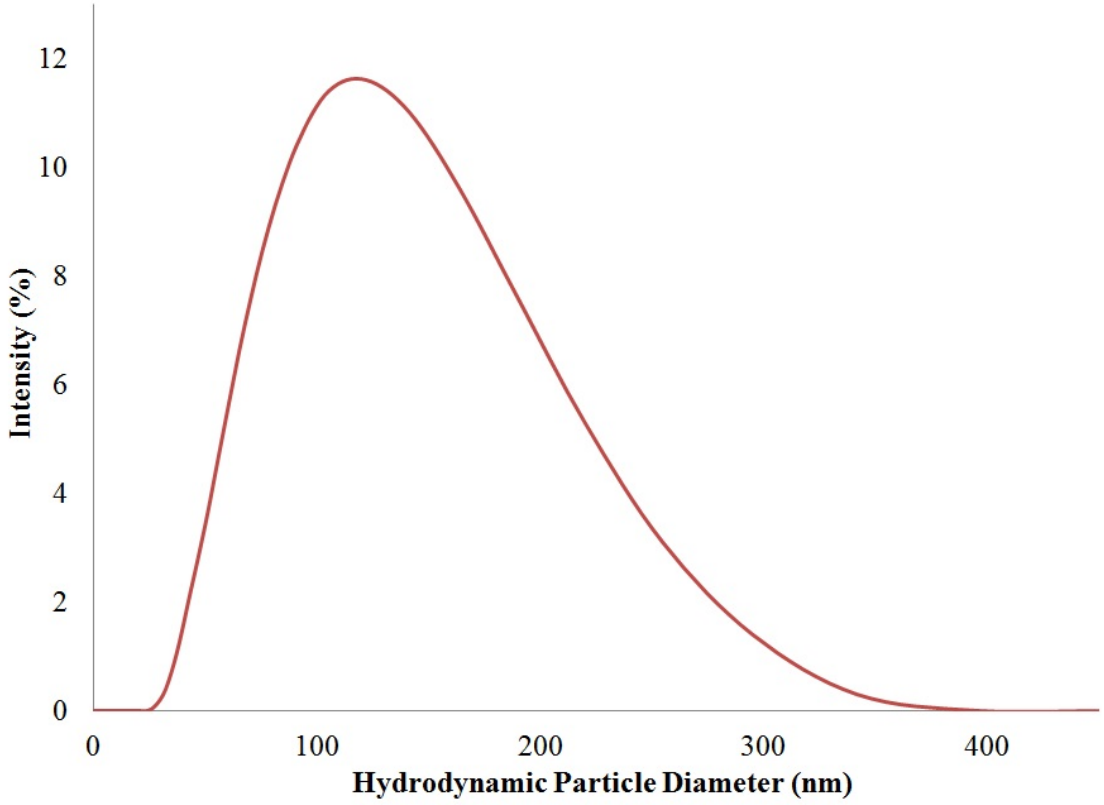

Figure A.1: Particle size distribution of the nC_{60} nanoparticle stock suspension by DLS, based on 14 independent measurements.

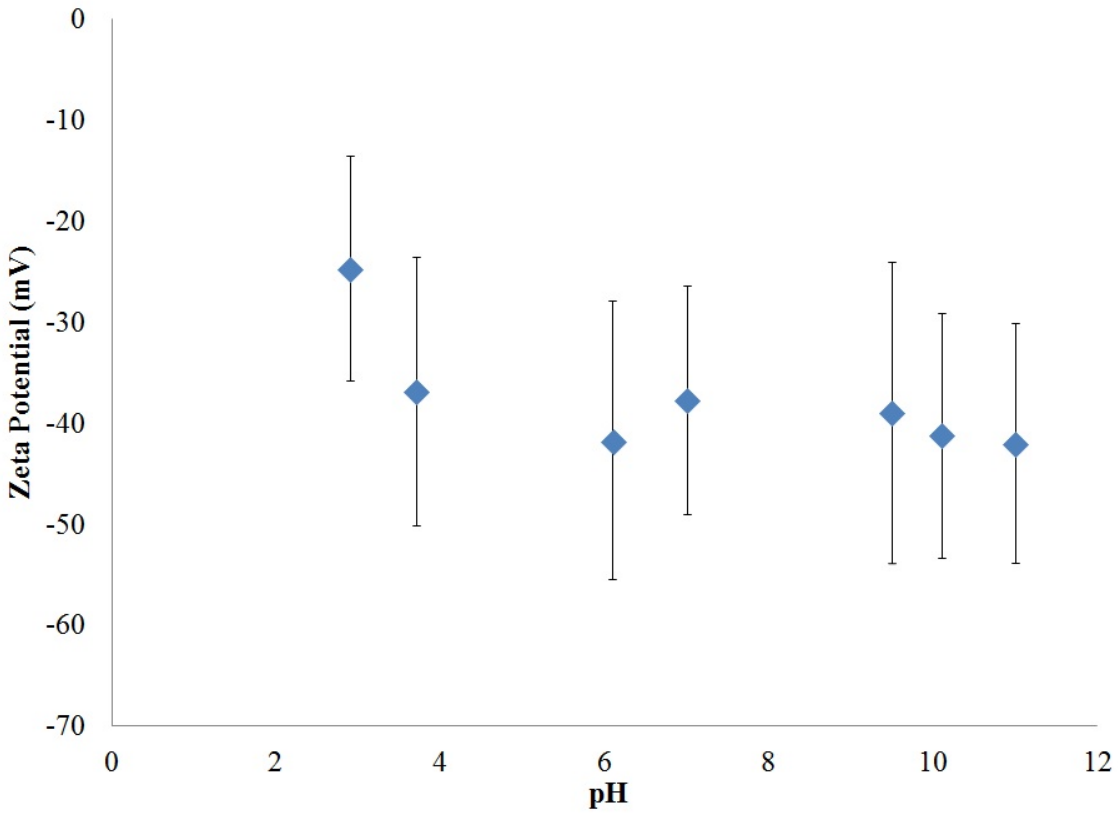

Figure A.2: Zeta potential of the nC_{60} stock suspension over a pH range of 3–10, by DLS. Each point represents 14 independent measurements and error bars represent a 95% confidence interval.

Table A.3: Temperature-dependent nC_{60} particle radius and relative dielectric permittivity of water used to calculate the total interaction energy between the nC_{60} particles and silica sensor surface.

Temperature (°C)	nC_{60} Particle Radius (nm)	ε_r
15	49.7	81.95
25	50.8	78.30
35	52.2	74.83
45	52.5	71.51

A.3 PS particle stretching details

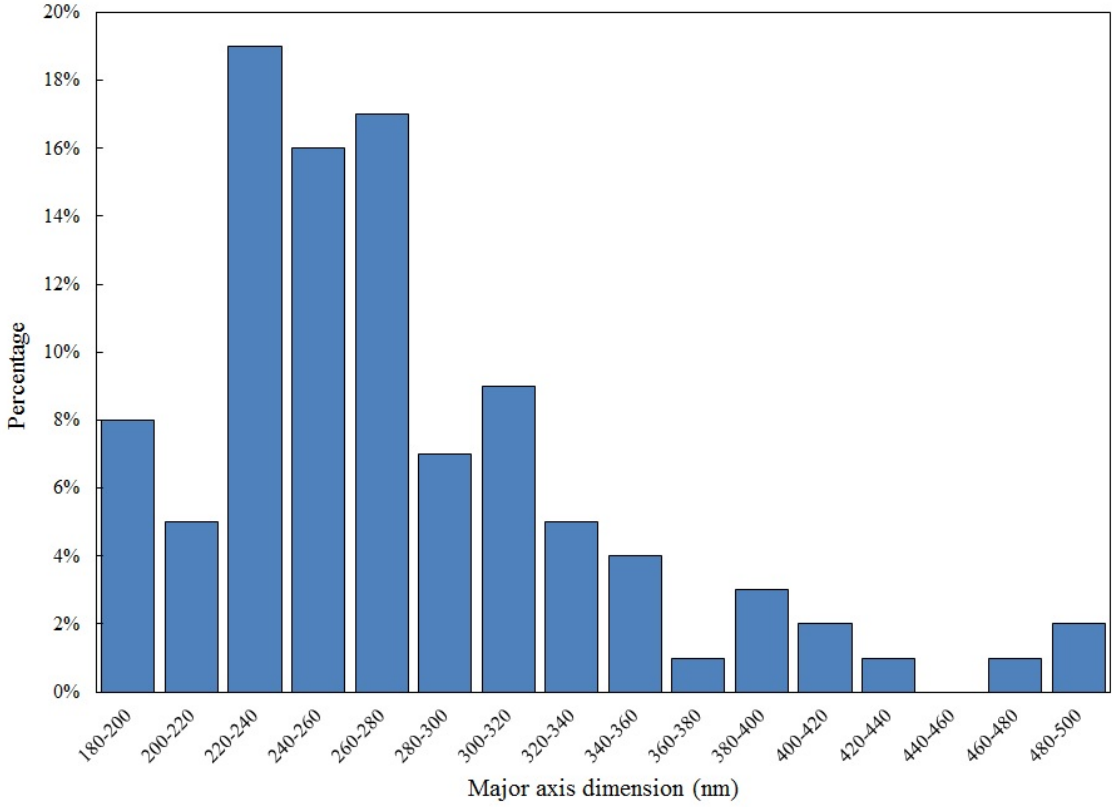

Figure A.3: Summary of the major axis dimensions of stretched PS.

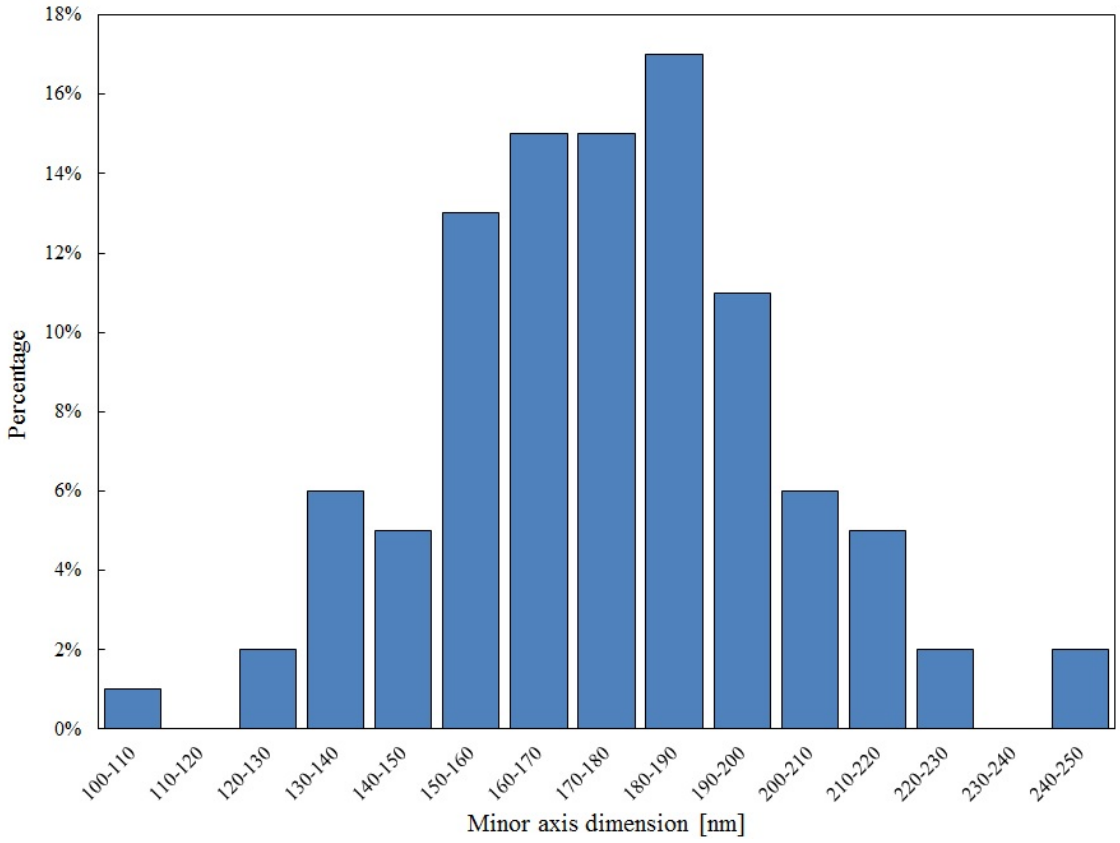

Figure A.4: Summary of the minor axis dimensions of stretched PS.

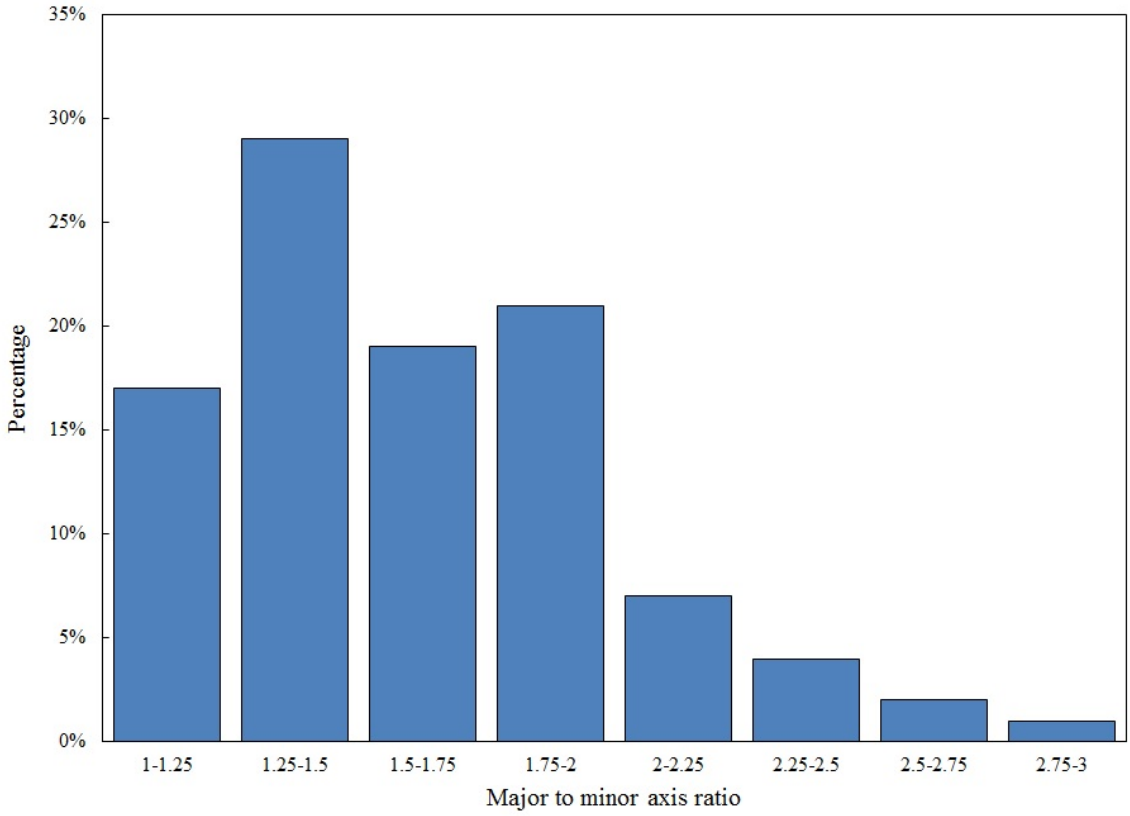

Figure A.5: Summary of the major to minor axis ratios of stretched PS.

The ellipticity (e), surface area (S), and effective diameter (d_{eff}) of the rod shape stretched particles are calculated using the following equations, where s and m are the radius of minor and major axis dimensions, respectively.

$$e = \sqrt{1 - \frac{s^2}{m^2}} \tag{A.1}$$

$$S = 2\pi s^2 + \frac{2\pi sm}{e} sin^{-1} e \tag{A.2}$$

$$d_{eff} = 2\sqrt{\frac{s}{4\pi}} \tag{A.3}$$

Appendix B

Reynolds and Peclet Number Calculations

In order to calculate Re and Pe of the QCM-D system, a parallel-plate channel configuration was assumed [60].

$$Re = \frac{\rho v L}{\mu} \tag{B.1}$$

Eq. B.1 was used to calculate the Re of the QCM-D system where ρ is the density of water, v is the flow velocity within the chamber ($2*10^{-4}$ ms^{-1}), L is the half depth of the channel ($3.2*10^{-4}$ m), and μ is the viscosity of water.

$$Pe = \frac{3va^3}{2L^2D} \tag{B.2}$$

$$D = \frac{kT}{3\pi\mu d} \tag{B.3}$$

Eq. B.2 was used to calculate the Pe of the QCM-D system where a is the nC_{60} particle radius and D is the diffusion coefficient. The diffusion coefficient was estimated using the Stokes-Einstein equation (Eq. B.3) where k is the Boltzmann constant ($1.38*10^{-23}$ JK^{-1}), T is the temperature (298 K), and d is the nC_{60} particle diameter.

Appendix C

Details on Grid Search Hyper Parameter Optimization with Cross Validation

For each model run, the mean 5-fold cross validation R^2 score is evaluated for each hyper parameter combination. The parameter combination resulting in the highest R^2 score is employed in the next step.

Table C.1: Grid search parameter optimization with cross validation (GSPOCV) parameter space for the chosen machine learning method (gradient boosting regressor).

Parameter	Range
Learning rate	[0.01,0.1,1,3,5]
Max depth	[3, 4, 5, 6, 7, 8, 9, None]
Max features	['auto', 'sqrt', 'log2'
Loss	['ls', 'lad']
Minimum Samples Leaf	[2]

Following GSHPOCV, recursive feature elimination with 5-fold cross validation (RFECV) was performed by recursively removing features of lesser importance from the training set, which is composed of four of five folds (68% of the total data), retraining the gradient boosting regressor on the reduced feature training set, and evaluating the performance of the regressor to predict the remaining fold (17% of the total data) until a single feature remained. For each of the five RFECV iterations, the RFECV routine generates 12 sets of gradient boosted decision regressors (with the feature set size decreasing from 13 to 1) and reports the feature set size corresponding to the highest cross-validation score (i.e., the 'optimum number of features')[142]. If two or more feature set sizes have the same score, the smallest set size is recorded. The optimum number of features indicates the minimum number of features required to maximize the cross-validation score for a particular cross-validation fold.